Science Concept 2: The Structure and Composition of the Lunar Interior Provide Fundamental Information on the Evolution of a Differentiated Planetary Body

Science Concept 2: The Structure and Composition of the Lunar Interior Provide Fundamental Information on the Evolution of a Differentiated Planetary Body

Science Goals:

a. Determine the thickness of the lunar crust (upper and lower) and characterize its lateral variability on regional and global scales.

b. Characterize the chemical/physical stratification in the mantle, particularly the nature of the putative 500-km discontinuity and the composition of the lower mantle.

c. Determine the size, composition, and state (solid/liquid) of the core of the Moon.

d. Characterize the thermal state of the interior and elucidate the workings of the planetary heat engine.

INTRODUCTION

Each of the Science Goals addressed by Science Concept 2 is linked: data regarding the crust, mantle, and core must be obtained in order to understand the thermal state of the interior and the planetary heat engine. Much about these Science Goals is currently unknown: crustal thickness and lateral variability are constrained by gravity and seismic models which suffer from non-uniqueness and a lack of control points; mantle composition is ambiguously estimated from seismic velocity profiles and assumed lunar bulk compositions; mantle structure is obtained through seismic velocity profiles, but fine-scale structure is not resolved and any structure outside the Apollo network and below 1000 kilometers depth is unknown; the size, composition and state of the core are obtained through models with few constraints, where the size and state are dependent on an unknown composition, making any core characteristic estimates highly variable; and the thermal state of the interior is constrained by heat flow measurements and characteristics of the core, but current heat flow data are not representative of the global heat flux and core models are non-unique. Besides elucidating the principle objectives of each Science Goal, addressing this Science Concept will also provide data regarding formation and evolution models of the Moon (*i.e.*, the Giant Impact (*e.g.*, Canup, 2004a, 2004b) and Lunar Magma Ocean (LMO; *e.g.*, Wood *et al.*, 1970) hypotheses, the details of which are debated or unknown.

Understanding the formation and evolution of the Moon provides important information on planetary and solar system evolution as a whole. The relative lack of geologic activity on the lunar surface provides a window into processes active during early Solar System formation that have since been removed from the Earth's surface. Likewise, the small size of the Moon implies a faster cooling history, preserving records of initial composition and interior structure (NRC, 2007).

The most comprehensive hypothesis for the formation of the Moon is the collision of an object twice the size of the Moon with the proto-Earth. Thus, the composition and thermal evolution of the Moon and Earth were intimately linked at the beginning of the solar system (NRC, 2007). While these two bodies have evolved independently of each other, a more complete understanding of the composition and structure of the lunar interior will shed light on the early history of Earth.

Other studies of Science Concepts in this volume suggest landing sites and data collection that will help address Science Concept 2. In particular, the knowledge gained by addressing Science Concept 1 will help

elucidate the early thermal history of the Moon (assisting Science Goal 2d). Proposed sample return for Science Concepts 3, 5 and 6 will contribute to current knowledge of crust and mantle lithologies (assisting Science Goals 2a, 2b). However, it should be noted that no other Science Concepts overlap with understanding the lunar core (Science Goal 2c). The contributions of other Science Concepts to the one considered here are outlined in more detail in each Science Goal section.

Approach

Since sample return alone will not be able to fully address each Science Concept 2 Science Goal, we examine landing sites for both geophysical analyses and sample return (Fig. 2.1). Geophysical analysis will provide information on the current state of the Moon, in particular the core, whereas sample return will address the evolution through time. This is especially needed for Science Goals 2b and 2c, where samples of the middle mantle, lower mantle, and the core are impossible to obtain. In addition, geophysical measurements can provide a global context where sample return may provide only local details. Therefore, each Science Goal will have two sets of proposed landing sites: one for geophysical measurements and one for sample return, with the exception of Science Goal 2c where no sample return is proposed (Fig. 2.1).

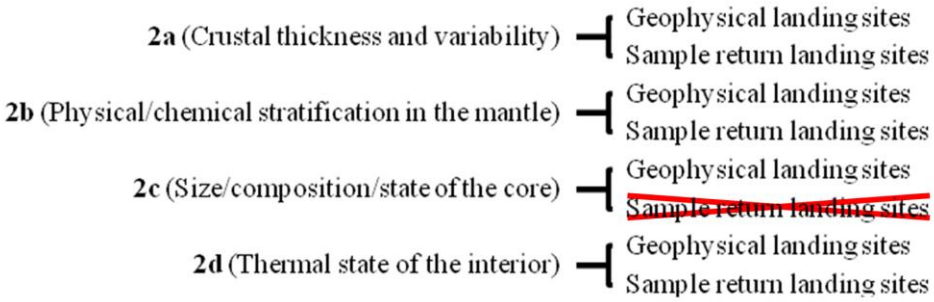

FIGURE 2.1 The types of landing sites for Science Concept 2. Each Science Goal has separate geophysical and landing site requirements, with the exception of Science Goal 2c, which only considers geophysical requirements.

GENERAL BACKGROUND

The aim of Science Concept 2 is to use various geophysical and compositional studies of the Moon to elucidate the interior structure and composition of a differentiated planetary body (NRC 2007). In order to address the state of the lunar crust (Science Goal 2a), mantle (Science Goal 2b), and core (Science Goal 2c), as well as the thermal state and nature of the planetary heat engine (Science Goal 2d), current knowledge about the formation and subsequent evolution of the Moon must be considered to provide important context. Here, we discuss (1) the Giant Impact model for the formation of the Moon (Canup, 2004a, 2004b, 2008), including potential lunar bulk compositions, (2) the initial differentiation of the Moon from a Lunar Magma Ocean (LMO: Smith *et al.*, 1970; Wood *et al.*, 1970), (3) subsequent cumulate overturn and reorganization of the lunar interior (*e.g.*, Hess and Parmentier, 1995), and (4) a brief summary of what is known about the lunar crust, mantle, core, and thermal evolution of the Moon (discussed in detail within each Science Goal).

Formation of the Moon

Early theories for the formation of the Moon suggested gravitational capture of an independently-formed body, fission or derivation from a proto-Earth, or co-formation with Earth (*i.e.*, a binary planetary system; Ringwood, 1979; Canup, 2004b). These theories could explain aspects of lunar formation and evolution, but each was unable to explain certain key features of the Earth-Moon system such as lunar iron depletion relative to Earth and the coupled Earth-Moon angular momentum (Canup, 2004b). Though it has not gained universal acceptance, most lunar scientists agree that the Moon was created by the collision of an impactor approximately twice the size of the current Moon with a proto-Earth that was ~70% of Earth's current size (Fig. 2.2; Hartmann and Davis, 1975; Cameron and Ward, 1976; Canup and Asphaug, 2001; Canup, 2004a, 2004b, 2008). Dynamic simulations of this impact (*e.g.*, Canup, 2004a, 2008) suggest a number of features key for explaining subsequent lunar evolution. For example, it is now thought that the Moon is derived mainly from the mantle of the impactor (Canup, 2004b; also supported by modeling of the lunar interior as in Khan *et al.*, 2004), while the core may have accreted to Earth (Canup, 2008) and thus could explain lunar iron depletion. Likewise, condensation of the Moon from 'cold' vapor outside the Earth's Roche limit (Canup, 2008) may explain the depletion of lunar volatile elements relative to Earth (Taylor *et al.*, 2006) and still allow for complete melting of the early-formed Moon (Canup and Asphaug, 2001). However, there is still significant uncertainty in constraints for lunar formation.

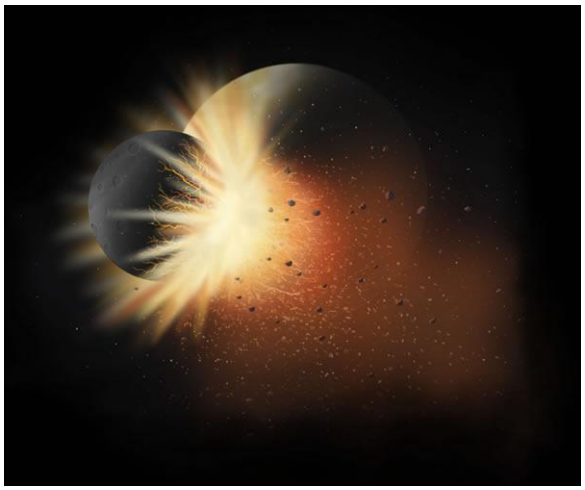

FIGURE 2.2 Illustration of an object twice the size of the Moon colliding with proto-Earth (~70% of its current size). Illustration credit: LPI (Leanne Woolley).

Lunar Bulk Composition

A linked consideration with the formation of the Moon is its bulk composition (Taylor *et al.*, 2006). Estimates for the lunar bulk composition differ primarily in their consideration of refractory lithophile elements (*e.g.*, Al), but other considerations include the abundances of FeO and MgO (Taylor *et al.*, 2006). Possible lunar bulk compositions have been modelled by a number of authors (see Taylor *et al.*, 2006), but recent experimental work on early lunar differentiation (Elardo *et al.*, 2011; Rapp and Draper, 2012) has focused on two possible end-members: Taylor Whole Moon (TWM: Taylor, 1982), which is enriched in refractory elements relative to Earth's composition, and Lunar Primitive Upper Mantle (LPUM: Longhi, 2003, 2006), which contains similar refractory element abundances relative to Earth (Table 2.1). TWM and LPUM also differ in FeO and MgO abundances (by ~3 and ~6 wt%, respectively: Elardo *et al.*, 2011). However, it is important to note that both TWM and LPUM are models based on combined geophysical and petrologic constraints. Further consideration of lunar bulk composition requires additional samples of lunar volcanic products (mare basalts and pyroclastic glasses), and would be especially aided by a sample of the lunar mantle (Taylor *et al.*, 2006).

TABLE 2.1 Lunar bulk compositions used by Taylor (1982) and Longhi (2006). Mg* is molar MgO/[MgO+FeO]. All oxide values are in wt%.

Model	SiO_2	MgO	FeO	Al_2O_3	CaO	Cr_2O_5	TiO_2	MnO	Na_2O	K_2O	P_2O_5	Mg*	CaO/Al_2O_3
TWM (Taylor, 1982)	44.4	32.7	10.9	6.1	4.6	0.61	0.31	0.15	0.09	0.01	0.01	84	0.75
LPUM (Longhi, 2006)	46.1	38.3	7.6	3.9	3.2	0.5	0.17	0.13	0.05	0.01	0.01	90	0.82

Lunar Magma Ocean (LMO)

Regardless of the conditions of lunar formation, it is generally agreed that subsequent widespread melting of lunar material resulted in a "magma ocean" extending from the surface to some depth, from which first-order lunar structure and stratification were derived and separation of the crust, mantle, and possibly the core occurred (*e.g.*, Shearer and Papike, 1999). Anorthositic (*i.e.*, dominated by calcic plagioclase feldspar) rocks and soil samples collected by Apollo 11 led scientists to hypothesize the existence of a global magma body that underwent extensive fractional crystallization (*e.g.*, Smith *et al.*, 1970; Wood *et al.*, 1970). According to this model, denser Mg-rich mafic minerals (dominantly olivine, with subsidiary orthopyroxene and clinopyroxene) sank to form lower mantle cumulates while less-dense plagioclase (formed after 60–80% total crystallization) floated to form the anorthositic crust (Smith *et al.*, 1970, Wood *et al.*, 1970; Taylor and Jakes, 1974; Ringwood and Kesson, 1976). The last vestiges of the magma ocean liquid, after 90–95% crystallization, were enriched in incompatible elements such as potassium, rare-earth elements, and phosphorus (together termed KREEP), as well as FeO- and TiO_2-rich minerals such as ilmenite (Fig. 2.3; Wood *et al.*, 1970; Taylor and Jakes, 1974; Warren and Wasson, 1979). Though there are multiple complications with this simple model, as discussed below, few scientists dispute the existence of an early LMO.

More recent work has questioned some of the assumptions and mechanisms of the simple LMO hypothesis. For example, the absolute crystallization sequence is difficult to predict given uncertainties in initial lunar bulk composition, convection flow regimes, and pressure/temperature conditions (Shearer and Papike, 1999 and references therein). Another complication is that early analyses of the LMO (*e.g.*, Wood *et al.*, 1970) considered a purely fractional end-member scenario, whereas more recent studies (*e.g.*, Snyder *et al.*, 1992) have shown the importance of both equilibrium and fractional crystallization in producing observed major- and trace-element patterns of mantle products (*i.e.*, mare basalts and pyroclastics).

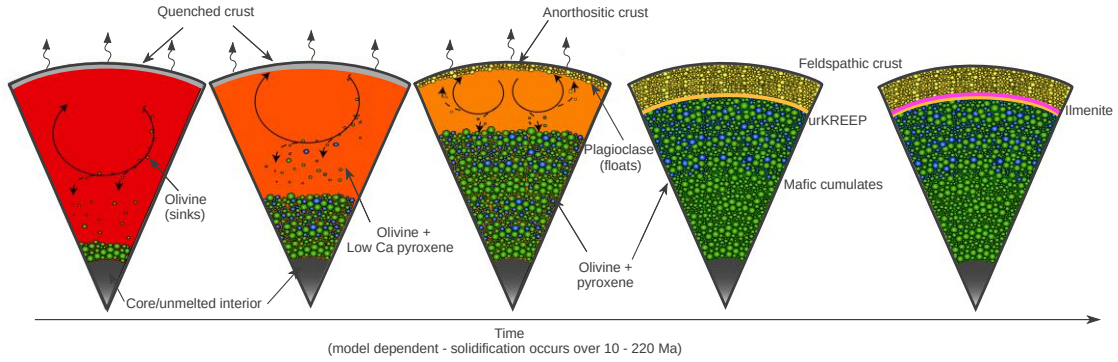

FIGURE 2.3 Simplified model of the crystallization of the lunar magma ocean (LMO; after J. Rapp/LPI). See text for a detailed explanation.

It is also unclear how much lunar material was processed in the LMO (*i.e.*, how deep the magma ocean extended and how much 'primitive' lunar material remained [or remains] below it). Most estimates for the

depth of the LMO range from 200–1000 km (Taylor and Jakes, 1974; Ringwood and Kesson, 1976; Solomon and Chaiken, 1976; Nakamura, 1983; Hess and Parmentier, 1995), although the purported existence of a 500-km seismic discontinuity (Nakamura *et al.*, 1974; Goins *et al.*, 1981b; see below) has led others to suggest this depth as the base of the magma ocean (*e.g.*, Mueller *et al.*, 1988). Part of this uncertainty stems from the fact that the extent and duration of melting depend on the heating mechanism, such that rapid accretion may indeed result in whole-Moon melting but slower accretion produces a shallower partially-melted zone (Shearer and Papike, 1999 and references therein). However, recent models tend to favor extensive to complete melting (Canup and Asphaug, 2001; Longhi, 2006).

While none of these problems are fatal to the LMO hypothesis, they suggest the need for further clarification and emphasize the complexity of such a global-scale process.

Cumulate Overturn of LMO Stratification

Various observations suggest that the lunar interior experienced significant reorganization after its initial stratification. For example, the crystallization of KREEP, FeO-, and ilmenite-rich components in the last stages of magma ocean solidification resulted in inverse density stratification, with the densest minerals at the top of the cumulate pile in a gravitationally unstable configuration (Ringwood and Kesson, 1976; Hess and Parmentier, 1995; Elkins-Tanton *et al.*, 2002). Additionally, while early studies suggested that the observed variability in mare basalt and pyroclastic glass compositions, particularly TiO_2 and KREEP abundances, could be explained by partial melting of discrete mantle sources at different depths (*e.g.*, Taylor and Jakes, 1974), their relatively homogenous major element chemistry suggested global-scale mixing (Shearer and Papike, 1999 and references therein). REE abundances show that this mixing must have occurred after initial magma ocean differentiation (Longhi, 1992). Further work on the volcanic products indicates that their source depths are independent of TiO_2 abundance, and trace element considerations suggest that mare and glass sources contain nearly continuous variation in ilmenite content, something that cannot be produced by remelting of static cumulates (Longhi, 1992 and references therein). Finally, evidence of this hybridization process is seen across the Apollo sample collection, implying the global-scale nature of the overturn event (Delano, 1986), though this point is controversial.

In order to explain these observations, some scientists have suggested a major phase of "cumulate overturn," whereby the dense, FeO-rich ilmenite cumulates at the top of the LMO sank towards the center of the Moon, interacted with deep mantle material, and either blanketed a pre-existing metallic core or created a dense silicate core (*e.g.*, Ringwood and Kesson, 1976; Hess and Parmentier, 1995; Elkins-Tanton *et al.*, 2002; de Vries *et al.*, 2010). The sinking of this material, combined with heating from ilmenite- and KREEP-bearing liquids and mixing with earlier-formed ultramafic cumulates (olivine ± orthopyroxene), produced a "hybrid" mantle zone (Ringwood and Kesson, 1976; Hess and Parmentier, 1995; Elkins-Tanton *et al.*, 2002) that could be remelted to form positively-buoyant plumes containing the range of observed volcanic compositions (*e.g.*, Hess and Parmentier, 1995; Singletary and Grove, 2008). One particularly important corollary of this process is that numerous rising or sinking plumes may have frozen in place to produce a laterally heterogeneous mantle (Hess and Parmentier, 1995; Sakamaki *et al.*, 2010; Elkins-Tanton *et al.*, 2011).

However, the details of this process are still debated. In particular, it is unclear if this overturn event was global (Hess and Parmentier, 1995; Elkin-Tanton *et al.*, 2002) or confined to local-scale convection cells (Fig. 2.4; Snyder *et al.*, 1992), and if the ilmenite-bearing material sank as a solid or liquid (Elkins-Tanton *et al.*, 2002). The depth of the "hybridized" mantle zone is also poorly constrained, with some studies suggesting ~300–500 km depth (Elkins-Tanton *et al.*, 2002, 2011) to the core-mantle boundary (Hess and Parmentier, 1995). Still other models for mantle structure do not require overturn and instead rely on melt generation at depth with assimilation of Ti-rich material at shallower mantle levels (*e.g.*, Wagner and Grove, 1997). The resolution of these issues requires both additional geophysical data and further petrologic data from as-yet unsampled volcanic and mantle lithologies.

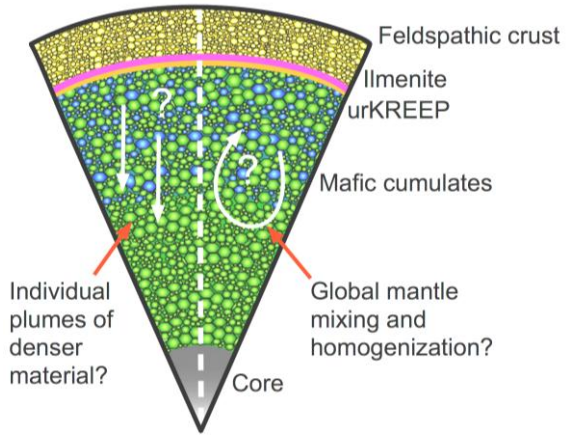

FIGURE 2.4 Two possible scenarios for cumulate overturn: individual plumes (left) or global mixing (right). Colors represent the same compositions as in Fig. 2.3.

Thickness of the Lunar Crust (*c.f.*, Science Goal 2a)

The plagioclase-rich crust of the Moon is on average ~50 km thick (Wieczorek *et al.*, 2006) and is thought to be vertically zoned from anorthositic compositions at the top to noritic or troctolitic compositions at its base (*e.g.*, Arai *et al.*, 2008). It is thickest in the lunar highlands away from large impact basins (some of which are mare-flooded), with a maximum thickness of 110 km and a minimum thickness near zero (*e.g.*, Ishihara *et al.*, 2009). The crust is notably asymmetric with respect to thickness; the farside highlands crust is on average 10–15 km thicker than the nearside (*e.g.*, Wood, 1973). These thickness changes apparently also correlate to compositional heterogeneity, such that the farside crust is more magnesian than the nearside (Arai *et al.*, 2008 and references therein).

Compositional and Physical Stratification of the Lunar Mantle (*c.f.*, Science Goal 2b)

Stratification of the lunar mantle is thought to have originated from (1) differentiation from the LMO, producing an olivine-rich lower mantle with the addition of ortho- and clinopyroxene upsection, culminating in an ilmenite- and KREEP-rich layer just below the crust (*e.g.*, Shearer and Papike, 1999), and (2) subsequent cumulate overturn that redistributed denser material to the base of the mantle and resulted in numerous positively- and negatively-buoyant plumes (*e.g.*, Hess and Parmentier, 1995). Apollo-era and more recent geophysical analyses have identified major compositional or mineralogical discontinuities such as a prevalent 500-km depth discontinuity (*e.g.*, Nakamura *et al.*, 1974; Goins *et al.*, 1981b), which indicate at least some remnant stratification of the mantle underneath the Apollo seismic network. Additionally, these data indicate that lunar seismicity is concentrated in the upper- and lower-most mantle (Nakamura, 1983). While the nature of upper-mantle seismicity is inconclusive (Frohlich and Nakamura, 2006), numerous studies have suggested the presence of a partially-melted lower-mantle attenuation zone as a driver for deep moonquake occurrence (*e.g.*, Frohlich and Nakamura, 2009; Qin *et al.*, 2012).

Size, Composition, and State of the Lunar Core (*c.f.*, Science Goal 2c)

Little is known about the lunar core, but various geophysical and petrologic analyses suggest the presence of a small (1–3 wt. %, <500 km radius), metallic (Fe to FeS) or dense silicate, partially to fully molten core (*e.g.*, Williams *et al.*, 2001; Wieczorek and Zuber, 2002). Further constraints on the size, composition, and state of the lunar core require additional data collection.

Past and Present Thermal State of the Lunar Interior (*c.f.*, Science Goal 2d)

The past thermal state of the interior is poorly constrained due to a lack of data regarding bulk composition and internal structure. However, it is generally believed that the Moon-forming impact (Cameron and Ward, 1976; Canup, 2004b) produced enough energy to create a lunar magma ocean (LMO) that extended to some depth (ranging from 200–1000 km or more; Solomon and Chaiken, 1976; Nakamura, 1983). LMO crystallization (Taylor and Jakes, 1974) and cumulate overturn (Elkins-Tanton *et al*, 2002)

directly affected internal structure and KREEP distribution, which in turn is hypothesized to dictate the location of magmatic activity (Wieczorek and Phillips, 2000). The asymmetric nature of crustal thickness (Ohtake *et al.*, 2012), KREEP distribution (Jolliff *et al.*, 2000), and mare volcanism (Lucey *et al.*, 1998; Zhong *et al.*, 2000) has led to an asymmetric heat flux throughout lunar history. Central magnetic anomalies (Hood, 2011) and paleomagnetic studies of Apollo samples (Garrick-Bethel *et al.*, 2009; Shea *et al.*, 2012; Suavet *et al.*, 2012) have revealed that the early Moon may have possessed an early core dynamo, but its timing and strength are not fully constrained. Data regarding the present thermal state of the interior is similarly lacking. Heat flow measurements from Apollo were not an accurate representation of global heat flux (Warren and Rasmussen, 1987), which is necessary to determine the present thermal gradient (Turcotte and Schubert, 2002). Additionally, constraints on core size, composition, and state (addressed in Science Goal 2c) are essential for understanding the past and current thermal state of the interior (Shearer *et al.*, 2006; Wieczorek *et al.*, 2006).

Geophysical Methods

Seismology

Seismology uses elastic waves propagating through a body to its first-order properties and structures. In this sense, seismology is a direct method of probing the interior of the Moon. Surface stations detect seismic waves travelling through the body of interest, which are used to infer the densities and phases of the materials that the seismic wave propagated through.

A seismic source generates two kinds of waves that travel through the interior of a medium: the pressure wave (P-wave), and the shear wave (S-wave). The P-wave arrives first, as it travels with a higher velocity, while the amount of lag before the arrival of the S-wave gives information on the wave's path length from the seismic source to the station. S-waves do not propagate through liquids, a property useful in determining the presence/absence of liquid or partially melted layers in the interior. Phase changes and ray path refraction can also lead to discontinuities in seismic velocities, Fig. 2.5 summarizes these properties. By taking advantage of this P and S-wave separation, one can obtain information on the vertical and lateral composition, phase, and density structures inside a body, as well as thermal and pressure variations, making seismology a powerful tool in investigating planetary interiors. This technique has significantly advanced our knowledge of Earth's interior structure (discussion above after Stacey and Davis, 2008).

In global seismology, the arrival time $\Delta \boldsymbol{t}$ of seismic rays formulate a forward problem: $\mathrm{G}\boldsymbol{s} = \Delta \boldsymbol{t}$. The matrix G contains geometric information pertaining to source-receiver configuration (*i.e.* the paths of the seismic ray through the medium), vector $\boldsymbol{s}$ contains information on the seismic velocity structure of the medium, and the vector $\Delta \boldsymbol{t}$ contains the arrival times of each ray (discussion above after Lay and Wallace, 1995).

Obtaining the information in $\boldsymbol{s}$, given $\Delta \boldsymbol{t}$ is the goal of the inverse problem. In most cases, due to the lack of coverage of ray paths, one can find many different model solutions for $\boldsymbol{s}$ when given G and $\Delta \boldsymbol{t}$. Thus, it is important to start with a design matrix G that minimizes this non-uniqueness. This can be done (to some extent) through optimizing configuration of the seismometers according to *a priori* information on the seismic source locations, or simply increasing the number and coverage of seismic stations. By this philosophy, lunar seismology is best approached using a network of concurrently-operating seismometers that ensures global coverage in order to not only locate seismic events, but also adequately use these events to study the three-dimensional velocity structure of the Moon's interior.

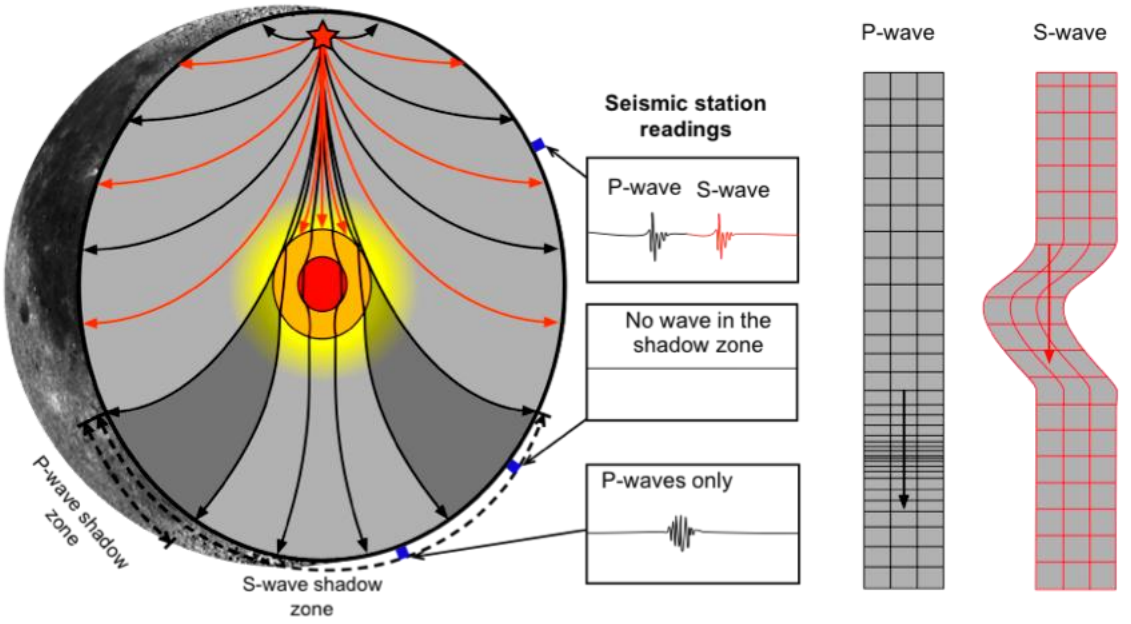

FIGURE 2.5 A summary of P- and S-wave ray paths propagating from a moonquake source (star) through the interior of a planetary body with a liquid outer core (orange) and solid inner core (red). The amount of refraction through the mantle is exaggerated for the moon (*left*). P-waves propagate with oscillations parallel to the direction of energy transfer, while S-waves use oscillations perpendicular to the energy propagation (*right*).

EM Sounding

EM sounding is a method of measuring the electrical conductivity structure throughout the interior of a body. Since electrical conductivity is directly related to thermal conductivity and composition, EM sounding is often used to complement other geophysical methods.

The electrical conductivities of various rock types are different. The electrical conductivities are also different for the same composition at different temperature and pressure environments (Sonett *et al.*, 1971). This is one of the ways EM sounding can provide an independent constraint on the thermal structure and interior composition. Another way the electrical conductivity profile of the planet can help constrain the thermal history of the body is through the Wiedemann-Franz Law. This law directly relates the electrical conductivity of a metal to its thermal conductivity (Wiedemann and Franz, 1853):

$$\frac{k}{\sigma} = LT \tag{2.1}$$

Here, L is a proportionality constant known as the Lorenz number, k is the thermal conductivity, and T is the temperature. Because of this relationship, determining the electrical conductivity is essential in addressing the thermal state of the lunar interior and especially of the core.

This method takes advantage of electromagnetic induction. In a conductor, currents can be induced by time variations in the external magnetic field. These induced currents will then generate their own magnetic field. By measuring both the external magnetic field variations and the current-generated internal magnetic field, one can study the conductivity structure at various depths (Fig. 2.6).

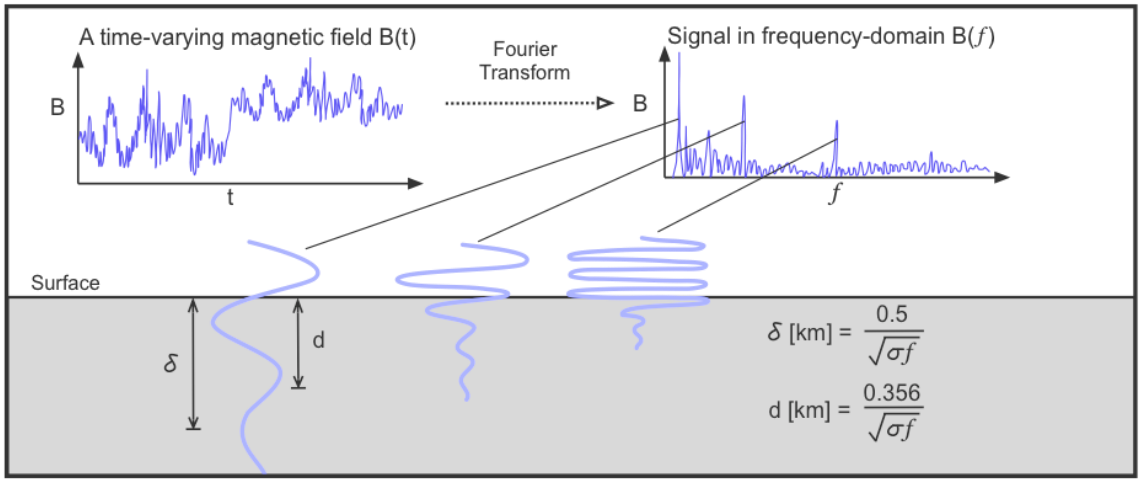

FIGURE 2.6 Various frequency components of a time-varying external field induce currents at various depths. Long-period (low *f*) variations can penetrate deeper into the body's interior. The frequency-response of the induced field can be used to invert for the conductivity structure as a function of depth.

The inductive response of the body varies with depth because of signal attenuation. The amount of attenuation depends on both the frequency of the time-varying signal (f) and the electrical conductivity (σ) of the body. Thus, various frequency components of the signal can probe various depths (Fig. 2.6). We thus can define the skin depth δ as the depth at which a signal attenuates by a factor of e, and adapt a quantity d from McNeill (1990) as the depth of exploration, equivalent to the depth to a perfect conductor for the specified conductivity and frequency (Grimm and Delory, *in press* and references therein):

$$\delta[\mathbf{km}] = \mathbf{0.}\frac{\mathbf{5}}{\sqrt{\sigma f}} \qquad d[\mathbf{km}] = \mathbf{0.}\frac{\mathbf{356}}{\sqrt{\sigma f}} \tag{2.2}$$

Complications arise in relating the measured total magnetic field to the induced magnetic field and in relating the induced field to the attenuation response below the surface. Thus there are various methods of studying the conductivity structure from magnetic field measurements, which are summarized in Fig. 2.7, and described in the next subsections.

Transfer Function (TF)

The transfer function method measures the magnetic field at a distal station orbiting several planet diameters away from the surface and at a proximal station in low orbit or at the surface. The distal station measures the undisturbed, time-varying external field, while the proximal station measures the total magnetic field due to both the external field and the induced field. The transfer function A = (A_R, A_T) is the ratio of the two measurements for each component (radial and tangential):

$$\mathbf{A_R}(f) = \frac{B_{R,proximal}}{B_{R,distal}} \qquad \mathbf{A_T}(f) = \frac{B_{T,proximal}}{B_{T,distal}} \tag{2.3}$$

Using the transfer function, the apparent conductivity (σ_a) as a function of frequency can be determined through a simple equation (Hobbs *et al.*, 1983). Here, μ is the magnetic permeability, and r is the lunar radius:

$$\sigma_{\mathbf{a}}(f) = \frac{\mathbf{1}}{\mathbf{2}\pi f\mu}\left(\frac{\mathbf{2}A_T}{rA_R}\right)^2 \tag{2.4}$$

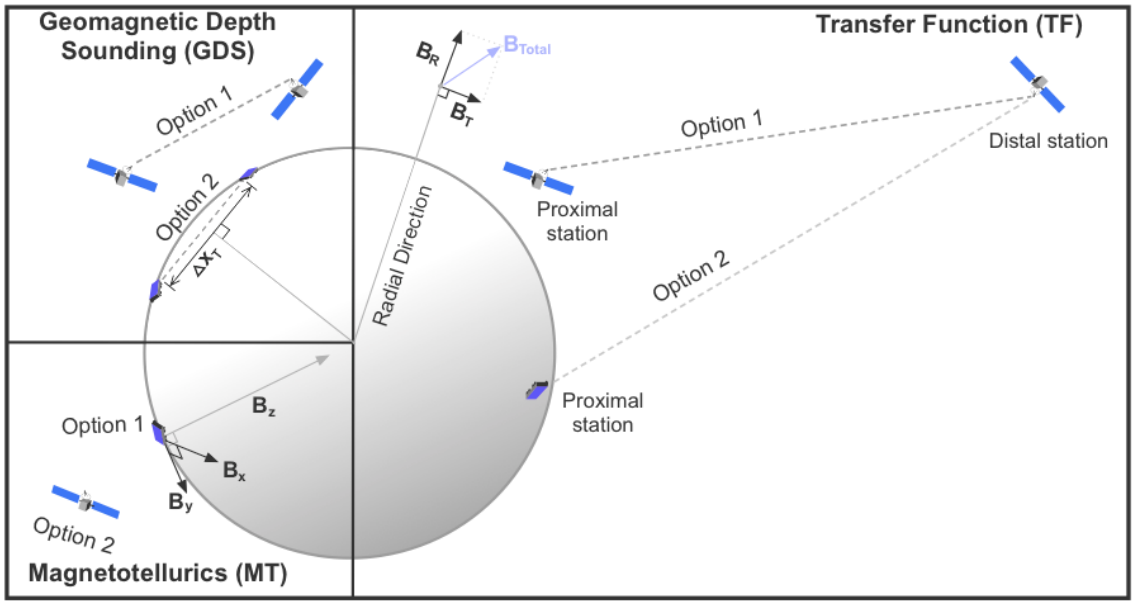

FIGURE 2.7 Options for station set-up and requirements for Geomagnetic Depth Sounding (GDS), Magnetotellurics (MT) and Transfer Function (TF) EM sounding methods. Dashed lines indicate measurements that need to be performed together. Coordinate systems are also illustrated for each method (Modified after Grimm and Delory, in press).

Geomagnetic Depth Sounding (GDS)

Another way to measure apparent conductivity is by taking the horizontal gradient of the tangential component of the magnetic field. This can be done using two or more magnetometers placed with spacing comparable to the exploration depth. The ratio between the radial magnetic field and the horizontal gradient of the tangential magnetic field can be used to determine the apparent conductivity. Here, the derivative with respect to x_T denotes a spatial gradient in the tangential direction (Gough and Ingham, 1983):

$$\sigma_a(f) = \frac{2}{\pi f \mu}\left|\frac{\frac{\partial B_T}{\partial x_T}}{B_R}\right|^2 \qquad (2.5)$$

Magnetotellurics (MT)

This method measures orthogonal components of the electric (E) and magnetic (B) fields from one station (Simpsons and Bahr, 2005). Using these measurements, two apparent conductivities can be calculated using the equations:

$$\sigma_{a,xy}(f) = \frac{2\pi f}{\mu}\left|\frac{B_y}{E_x}\right|^2 \qquad \sigma_{a,yx}(f) = \frac{2\pi f}{\mu}\left|\frac{B_x}{E_y}\right|^2 \qquad (2.6)$$

The two values will coincide if the medium below is horizontally isotropic in terms of the conductivity. Thus, comparing the two values can also give an indication of any lateral heterogeneity that might be present (Grimm and Delory, in press).

Lunar Laser Ranging (LLR)

The internal deformation of the Moon can modify its orbit and rotation in subtle ways (Fig. 2.8). A suite of highly developed mathematical analyses can be used to interpret these movements and give information about the structure and behavior of the lunar interior. To do so, one must first accurately measure these subtle lunar wobbles. To date, lunar laser ranging (LLR) is the only viable means of doing so with the required accuracy (Williams *et al.*, 2006).

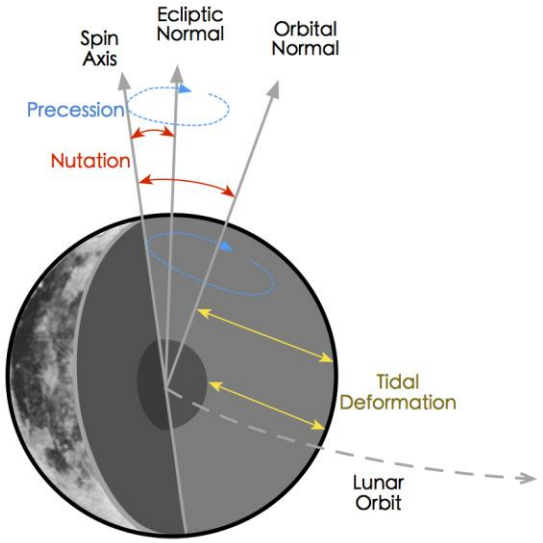

FIGURE 2.8 Libration and tidal deformation of the Moon. Precession corresponds to circular motion about the center of mass, whereas nutation corresponds to lateral movement rotating about the center of mass.

For a solid body object in 3-dimensions, its mass distribution is described by a moment of inertia tensor **I**. This tensor can be decomposed into three separate tensors, describing the solid mass distribution ($\mathbf{I}_{rigid}$), the time-varying mass distribution due to tidal deformation ($\mathbf{I}_{tide}$), and the spin-related distortion to the moment of inertia measurement ($\mathbf{I}_{spin}$) (Williams *et al.*, 2001):

$$\mathbf{I} = \mathbf{I}_{rigid} + \mathbf{I}_{tide} + \mathbf{I}_{spin} \qquad (2.7)$$

The rigid-body moment of inertia tensor ($\mathbf{I}_{rigid}$) has eigenvectors associated with the principal axes of the Moon. The eigenvalues of this coordinate system (A<B<C) are called the rigid-body moments. These describe the time-averaged mass distribution of a body with respect to each of the principal axes. The principal axis associated with A is approximately pointing towards the Earth. The axis associated with C is pointing approximately in the direction of the rotational vector of the moon.

Tidal and rotational affects can act to deform the body with observed monthly variations of ±9 cm (Williams *et al.*, 2010). These variations depend on the Moon's elastic properties, characterized by tidal Love numbers h_2, l_2 and k_2. These values can be used jointly with seismic data to invert for mantle and core structure (Merkowitz *et al.*, 2007). Thus, accurate determination of these values will help constrain the bulk elastic properties of the lunar interior. Love number k_2 also depends on any flattening of the core-mantle boundary (CMB) along the C-axis. The tidal love numbers and the ratios of the principal moments (A, B and C) can all be determined through accurate measurements of the Moon's physical librations. The existence of a fluid core, size of the outer core, possible inner core and the geometry of the CMB can also have significant effects on this libration through their interactions with the solid mantle (Williams and Boggs, 2008).

LLR measures the physical librations by precisely monitoring the positions of various points on the lunar surface relative to Earth. This can be done by installing retroreflectors on the Moon and measuring the travel time of the pulses sent to these reflectors that have reflected back to Earth. A retroreflector network is currently installed on the Moon, but it is limited in both E-W and N-S extent. Increasing this

span would improve the accuracy of the measurements, and would help better constrain the bulk elastic properties of the lunar mantle, and the size, geometry and state of the core.

Heat Flow Measurements

By measuring the present rate at which a planetary body is dissipating heat, one can learn about not only the present interior thermal structure but also the thermal history of the body. Knowledge of the thermal structure of the interior and how it evolved with time can also constrain the density and compositional stratification of the mantle. In general, thermal energy is dissipated through advection, conduction and radiation. Advection requires transport of heat-carrying material, which does not happen in the lunar regolith due to the lack of an advecting medium (*e.g.* water, air). The regolith material is also radiatively opaque. Although its porosity allows for radiative transfer within the regolith, it can be treated as a property of the regolith that affects its thermal conductivity (Kiefer, 2012). Thus, the total heat flow at the lunar surface can be well approximated by measuring the conductive heat flux. In accordance to Fourier's law of conduction, the conductive heat flux radially outward (q_z) is given by:

$$q_z = -k\frac{dT}{dz} \tag{2.8}$$

where z is depth, T is temperature, and k is the thermal conductivity of the material. Therefore, the measurement of q_z requires the determination of both the geothermal gradient and the thermal conductivity.

The geothermal gradient can be measured in boreholes >3 m deep with temperatures taken at different depths spanning at least 1 m below material affected by the annual and diurnal thermal waves (Kiefer, 2012). The thermal conductivity can be determined through the measurements of the thermal diffusivity (κ), which is related to the rate at which a material responds to temperature perturbations at various distances from the perturbation. This can be measured both actively (using a heating source and sensor) and passively (using periodic changes in surface insolation). The conductivity (k) can then be determined through the relation, $k = \kappa C_p \rho$, with appropriate values for the specific heat (C_p) and density (ρ) assigned.

Gravity Measurements

The sub-surface structure of the Moon can be probed by measuring the gravity field. This can be done in orbit by tracking the acceleration of a spacecraft as it flies over the surface. The acceleration $\boldsymbol{a}$ spacecraft experiences depends on the mass distribution:

$$\boldsymbol{a}(\boldsymbol{r}) = -G\iiint \frac{(\boldsymbol{r}-\boldsymbol{r}')}{|\boldsymbol{r}-\boldsymbol{r}'|^3}\rho(\boldsymbol{r}')d\boldsymbol{r}'^3 \tag{2.9}$$

Here G is the universal gravitational constant, $\boldsymbol{r}'$ is the coordinate of the mass element ($dm = \rho(\boldsymbol{r}')d\boldsymbol{r}'^3$), $\boldsymbol{r}$ is the position of the spacecraft and $|\boldsymbol{r}-\boldsymbol{r}'|$ is the distance from the mass element to the spacecraft.

The greatest contributor to changes in acceleration is the mass excess/deficit directly below the spacecraft. Thus, accurately tracking the changes in position ($\boldsymbol{r}$) and acceleration of an orbiter as it flies over a terrain will map the near-surface mass distribution (Stacey and Davis, 2008). To overcome the difficulty of tracking an orbiter on the lunar farside, a twin satellite approach can be employed. In this case, one satellite goes over a feature first and accelerates, changing the distance from the satellite behind. The separation change can be measured and recorded without communication with Earth. This is the approach taken by the new Gravity Recovery And Interior Laboratory (GRAIL) mission (Zuber, 2008). The spatial resolution of gravity mapping is comparable to the orbital altitude. Contributions to gravity anomalies from topographic features (*e.g.* mounds, craters) can be processed out of the data with knowledge of the feature's average density (*i.e.*, Bouguer correction).

After corrections, the gravity anomaly is a measure of the subsurface density distribution and can give information about subsurface structure. Any gravity excess/deficit will be due to a combination of variations in thickness and density of the crust or underlying mantle. One can then use *a priori* information concerning density variations to produce global crustal thickness models (Wieczorek *et al.*, 2006). These models need to be refined/anchored with surface studies (*i.e.*, seismology) of crustal thickness at representative sites. In addition to crustal information, tracking orbiters can also yield the moment of inertia (I) of the body, which gives information on internal mass concentration, constraining the existence

of a dense core. Temporal variations in the gravity field due to tides can also be measured with an orbiter, which would constrain tidal Love number k_2 (Williams *et al.*, 2010).

GENERAL METHODS

ArcMap 10 geographic information systems (GIS) software and MATLAB were used extensively throughout the landing site selection process to locate regions which matched the criteria set out for geophysical and sample return requirements specific to each Science Goal.

Separate project files for geophysical and sample return elements of each Science Goal were produced. These project files contain all relevant data available to find all the possible landing sites to address that particular element of the Science Concept. At the end of each Science Goal, geophysical and sample return maps were combined to find the sites where the most questions may be answered for each Science Goal. In some cases the geophysical and sample return elements of each Science Goal were not compatible. Finally, all the maps were brought together to find landing sites that may be appropriate to address Science Concept 2.

There are two global map projections used throughout the report: Plate Carree and Orthographic. Plate Carree is the most common for global datasets and is centered at 0°E. An orthographic projection is used when there is a need to emphasize nearside and farside locations and is also centered at 0°E. All projections use the International Astronomical Union (IAU) 2006 Moon as a reference sphere, which has a radius of 1,737.4 km (Seidelmann *et al.*, 2007).

DATA

All data used for the landing site selection process are shown in Table 2.2.

TABLE 2.2 All datasets used for Science Concept 2.

Data	Resolution	Instrument	Source	Authors
Imagery				
WAC Global Mosaic	64 ppd	LRO	http://wms.lroc.asu.edu/lroc/global_product/100_mpp_global_bw	
Digital Terrain Model				
LDEM	64 ppd	LOLA	http://imbrium.mit.edu/DATA/LOLA_GDR/CYLINDRICAL/IMG/	
LDEM	128 ppd	LOLA	http://imbrium.mit.edu/DATA/LOLA_GDR/CYLINDRICAL/IMG/	
Crater Records				
LPI-CLSE crater database	N/A	N/A	http://www.lpi.usra.edu/lunar/surface/Lunar_Impact_Crater_Database_v24May2011.xls	Losiak *et al.* (2009); revised by Ohman (2011)
LOLA Crater Database	N/A	LOLA	http://www.planetary.brown.edu/html_pages/LOLAcraters.html	Head *et al.* (2010)

Magnetic Data				
Internal magnetic field	1°	LP magnetometer and Clementine Topography	http://core2.gsfc.nasa.gov/research/purucker/moon_2010/index.html	Purucker and Nicholas (2007)
Element Data				
Thorium		LP		
Titanium		LP		
Iron		LP		
Ejecta Material				
Crater ejecta material	Shapefiles			Science Concept 5
Other				
Sinuous Rilles	Shapefiles			Hurwitz *et al.* (submitted to Planetary and Space Science, May 2012)
Floor-Fractured Craters	Shapefiles			Science Concept 5
Pyroclastic database	Shapefiles			Refer to Table A2.2 for references
Cryptomare deposits	Shapefiles			Refer to Table A2.3 for references
Olivine detection	Shapefiles			Yamamoto *et al.* (2010), Table A2.5
Deep moonquake nest locations				Nakamura (2005)
Shallow moonquake event locations				Nakamura (1977)

Digital Elevation Model (DEM)

The Lunar Orbiter Laser Altimeter (LOLA) 64 and 128 pixels per degree (ppd) gridded datasets were used to produce a slope map and a map of areas visible from the Earth's surface.

Imagery

Images used in this study come from the Lunar Reconnaissance Orbiter (LRO) Wide Angle Camera (WAC) global mosaic. The 64 ppd version of this dataset is used in global maps where higher resolution is not necessary.

Slope

Slope maps were produced from the LOLA 64 ppd elevation dataset, where the value of the slope represents the maximum slope between the pixel and one of its neighbors (slope value in degrees). The 64 ppd LOLA DEM was used as it was not deemed necessary to have slope at higher resolution and the only slope requirement was to land well away from areas of 20°or larger slope.

SCIENCE GOAL 2A: DETERMINE THE THICKNESS OF THE LUNAR CRUST (UPPER AND LOWER) AND CHARACTERIZE ITS LATERAL VARIABILITY ON REGIONAL AND GLOBAL SCALES

Introduction

Compared to the relative lack of information regarding the lunar mantle and core, decades of petrologic and geophysical analyses of the lunar crust have resulted in a significant, but far from complete, understanding of its thickness, chemistry, and spatial variation across the Moon. For example, it is generally accepted that (1) the crust is thicker under the primordial highlands than under major impact basins and mare (Wood, 1973), (2) the farside highlands crust is thicker and more magnesian than the nearside highlands (Wieczorek *et al.*, 2006; Arai *et al.*, 2008 and references therein), and (3) the crust is vertically stratified (Toksöz *et al.*, 1974; Ryder and Wood, 1977; Spudis and Davis, 1986; Ryder *et al.*, 1997; Tompkins and Pieters, 1999) and laterally heterogeneous in thickness (Chenet *et al.*, 2006) and composition (Arai *et al.*, 2008). Given the work of previous studies, additional geophysical analyses are key to further understanding the nature and distribution of lunar crustal material. These analyses include passive seismic experiments and electromagnetic (EM) sounding data, coupled with orbital analyses of the lunar gravity field (*e.g.*, the ongoing GRAIL mission). These data will provide direct insights about crustal thickness and better constrain models for lunar crustal formation and evolution.

The purpose of sample return in a crustal thickness context is to better understand the global geochemistry of the lunar crust, which has important implications for crustal thickness and petrogenesis. It is widely accepted that the uppermost part of the lunar crust is mainly anorthositic (containing calcic plagioclase feldspar), whereas the lower crust is more mafic in composition (containing a greater fraction of olivine and pyroxene) (Ryder and Wood, 1977; Spudis and Davis, 1986; Wieczorek and Zuber, 2001; Arai *et al.*, 2008 and references therein). However, outcrops of pure anorthosite are limited (Hawke *et al.*, 2003) and there is evidence of significant lateral and vertical heterogeneity in crustal composition on a regional (Ryder *et al.*, 1997) to global scale (Arai *et al.*, 2008). Additionally, it has recently been suggested that compositional variations may correlate to differences in crustal thickness (Cahill *et al.*, 2009). It is therefore anticipated that sample return will be used to provide compositional context for the geophysical measurements made. For example, sample return may determine whether a physical or compositional transition is responsible for a marked change in seismic velocity at ~20 km depth (*e.g.*, Toksöz *et al.*, 1974).

Science Concept 3 also requires samples of crustal materials and as such many of the requirements and approaches described here will overlap with that Science Goal. The rocks that will be considered for sample return are those that can be shown to provide representative compositions of the whole crustal stratigraphy (upper and lower lunar crust) over regional and global scales.

Background

Thickness of the Lunar Crust

Though suffering from limited data and poor resolution, orbital gravity and laser altimetry studies first noted the hemispherical dichotomy in crustal thickness, with a farside crust that was proposed to be ~10–15

km thicker than that of the nearside (*e.g.*, Wood, 1973; Kaula *et al.*, 1974). Thinner crust was also inferred under mare basalts (*i.e.*, in large impact basins: Wood, 1973; Kaula *et al.*, 1974). These studies were complemented by seismic data from Apollo 12, 14, 15, and 16 that placed constraints on crustal thicknesses at known surface locations (Toksöz *et al.*, 1972, 1974; Goins *et al.*, 1981a). The Apollo 12 and 14 sites (located <200 km from each other) were interpreted to have crustal thicknesses around 58–65 km (Toksöz *et al.*, 1972, 1974; Nakamura *et al.*, 1982), compared to the topographically higher Apollo 16 site that maintained a thicker 75-km crust (Goins *et al.*, 1981a). Both sites showed evidence of a 20-km seismic discontinuity (Toksöz *et al.*, 1972, 1974; Goins *et al.*, 1981a) that has been interpreted either as a physical (*i.e.*, due to annealing of impact-related fractures with depth: Simmons *et al.*, 1973) or a compositional boundary (*i.e.*, a more mafic lower crust overlain by felsic anorthosites: Toksöz *et al.*, 1972, 1974; Ryder and Wood, 1977; Tompkins and Pieters, 1999). It has also been suggested that a compositionally-stratified crust may result in a physical fracture discontinuity due to differences in material properties (Wieczorek and Phillips, 1997).

More recent studies of lunar crustal thickness have tended to either reanalyze the Apollo seismic data (Khan *et al.*, 2000; Khan and Mosegaard, 2002; Lognonné *et al.*, 2003; Chenet *et al.*, 2006) or utilize updated gravity and topography datasets (*e.g.*, Clementine: Zuber *et al.*, 1994; Lunar Prospector: Konopliv *et al.*, 1998, 2001) to calculate global crustal thickness (Zuber *et al.*, 1994; Wieczorek *et al.*, 2006; Hikida and Wieczorek, 2007; Ishihara *et al.*, 2009; see below). These datasets are not mutually exclusive; seismic analyses can only determine crustal thickness local to the Apollo Seismic Network (or any future network), but gravity- and topography-derived datasets require seismic data as pinning points for global models. Many early gravity-derived models were anchored to ~60 km crustal thicknesses at the Apollo 12 and 14 sites (*e.g.*, Zuber *et al.*, 1994); however, recent seismic reanalyses and gravity models show that the Apollo 12 and 14 sites are likely thinner than proposed by Toksöz *et al.* (1972, 1974), with various workers suggesting values of 30–50 km (Khan *et al.*, 2000; Khan and Mosegaard, 2002; Lognonné *et al.*, 2003; Chenet *et al.*, 2006; Hikida and Wieczorek, 2007; Ishihara *et al.*, 2009). Similarly, the proposed crustal thickness for the Apollo 16 landing site has also been reduced, for example to 38±7 km (Chenet *et al.*, 2006) or ~54 km (Hikida and Wieczorek, 2007). Significant discrepancies in proposed crustal thicknesses exist between gravity- and seismic-derived models (*e.g.*, the gravity model of Ishihara *et al.* (2009) compared to the seismic model of Chenet *et al.* (2006)) and even between models derived from similar datasets (*e.g.*, the seismic model of Khan *et al.* (2000) compared to that of Lognonné *et al.* (2003)), elucidating the need for further orbiter and surface data collection. (Additional data on crustal thickness are contained in geoid-to-topography ratio (GTR) and spectral admittance studies; see Wieczorek *et al.* (2006) for a compilation.)

Still, a number of important conclusions derived by early studies have been supported. For example, the farside highlands crust contains the thickest crust (up to ~110 km: Ishihara *et al.*, 2009) and is on average 10–20 km thicker than the nearside (Zuber *et al.*, 1994; Chenet *et al.*, 2006; Wieczorek *et al.*, 2006); crustal thickness is at a minimum in large, mare-flooded impact basins such as Crisium, Orientale, and Moscoviense (Zuber *et al.*, 1994; Wieczorek *et al.*, 2006; Hikida and Wieczorek, 2007); and the 20-km seismic discontinuity is likely real and may be widespread in the lunar crust (Wieczorek and Phillips, 1997; Khan *et al.*, 2000; Khan and Mosegaard, 2002). Additionally, there are large lateral variations in the crust, perhaps relating to heterogeneity in fracture concentrations or the influence of heterogeneous serial magmatism (Chenet *et al.*, 2006). Finally, the average crustal thickness for the entire Moon is thought to be around 50 km (Wieczorek *et al.*, 2006; Ishihara *et al.*, 2009), which is useful as a reference value for future crustal thickness models.

The origin of the hemispherical asymmetry in crustal thickness is less clear. Early studies correlated this anomaly to the nearside concentration of mare basalts and KREEP, and the center-of-mass/center-of-figure offset (*e.g.*, Wood, 1973; Kaula *et al.*, 1974) and suggested their coupled derivation from asymmetric asteroid bombardment (Wood, 1973) or asymmetric crustal growth (Warren and Wasson, 1980; Arai *et al.*, 2008). Recent work has considered the influence of either internal asymmetries in LMO convection (Loper and Werner, 2002) and tidal dissipation (Garrick-Bethell *et al.*, 2010) or external asymmetries such as the distribution of SPA ejecta (Zuber *et al.*, 1994; Arai *et al.*, 2008). Accretion of a companion moon to the lunar farside has also been proposed (Jutzi and Asphaug, 2011). Further discussion is beyond the scope of this work, but increased understanding of crustal thickness and its variability will help constrain the accuracy of these models and contribute to knowledge of early lunar formation.

Recent and Ongoing Gravity Datasets (esp. for Crustal Thickness)

The most widely used lunar gravity map to model crustal thickness was developed using data from Lunar Prospector, which was launched by NASA in 1999. These data were taken by measuring Doppler shifts in the microwave-tracking signal as it reaches Earth, and converted into acceleration to provide information on the gravity field (Konopliv *et al.*, 1998). This method has only been able to indirectly map the farside of the Moon due to the lack of line-of-site communication with Earth, and as such the precision and reliability of farside gravity maps is uncertain. SELENE Kaguya first directly mapped the farside gravity field on the Moon by using four-way Doppler tracking with relay sub-satellite Okina, launched by JAXA in 2007 (Namiki *et al.*, 2009), which has already significantly improved the accuracy of farside gravity maps (*e.g.*, Ishihara *et al.*, 2009).

The ongoing Gravity Recovery and Interior Laboratory (GRAIL) mission, launched by NASA in 2011, consists of two near-identical lunar orbiters, a leader (Ebb) and a follower (Flow), that measure a microwave beam transmitted between them to find their relative position (assisted by GPS) from which variations in the Moon's gravity can be extracted. The first stage has successfully mapped global gravity variations from a 50 km altitude with a spherical harmonic degree of 330, improving current lunar gravity data maps from SELENE by 3× on the nearside (previous spherical harmonic degree of 110) (Konopliv *et al.*, 2001) and 5× on the farside (previous spherical harmonic degree of 70) (Matsumoto *et al.*, 2010). During the second stage, GRAIL will perform high-resolution (30 km × 30 km) mapping to a higher accuracy of <1 mGal (1 mGal = 0.01 m/s^2) (W. Kiefer, pers. comm.) with a tracking error of <0.1 μm/s (Weaver *et al.*, 2010).

The main objectives of GRAIL are to determine the structure of the lunar interior from crust to core (Science Goal 2a and 2c) and to advance understanding of the thermal evolution of the moon (Science Goal 2d). In particular, GRAIL investigations will include:

- Mapping crustal and lithospheric structure (combined with LOLA topography data)
- Ascertaining temporal evolution of crustal brecciation and magnetism
- Determining subsurface structure of impact basins and mascon ("mass concentration") origin
- Understanding asymmetric lunar thermal evolution
- Constraining deep interior structure from tides
- Placing limits on size of a possible solid inner core

Since these objectives directly correlate to Science Concept 2 (in particular Science Goals 2a, 2c, and 2d), the completion of the GRAIL mission and subsequent release of data will greatly contribute to the work that is outlined here.

Deriving Crustal Thickness from Gravity

The gravity anomaly map is used in conjunction with a high-resolution topographic map to model the Moon's crustal thickness, primarily by subtracting the gravitational effects from surface topography (*e.g.*, a crater or mountain), amongst other corrections. This method is illustrated as a flow diagram in Fig. 2.9. These models can be further constrained and improved by using passive seismic nodes with known crustal thicknesses as anchor points (*e.g.*, Chenet *et al.*, 2006).

For the purposes of this report, we use crustal thickness models derived from Lunar Prospector data and Clementine topography (Wieczorek *et al.*, 2006), as complete Kaguya SELENE and GRAIL data are not yet publicly available. However, we note that preliminary results are available in the literature; the most recent iteration of lunar crustal thickness models uses combined SELENE gravity and topography data (Ishihara *et al.*, 2009), and these models will be superseded by GRAIL's high-resolution gravity data combined with the LRO LOLA topography map.

Composition and Petrogenesis of the Lunar Crust

A full understanding of crustal thickness requires consideration of crustal composition, particularly to provide constraints to seismic and gravity/topography models (*e.g.*, density) of the lunar crust. Additionally, compositional constraints are required to formulate models for the crustal formation and evolution that can explain crustal thickness distributions.

Considering the constraints from LMO differentiation models, the Al-rich anorthositic upper crust is thought to have formed directly from the magma ocean by plagioclase flotation (Wood *et al.*, 1970), though others have suggested the influence of more complicated processes involving reprocessing of primitive crust (*e.g.*, Walker, 1983; Longhi, 2003; Meyer *et al.*, 2010). In contrast, petrologic and remote sensing studies indicate that the lower crust is more mafic but still contains plagioclase (Ryder and Wood, 1977; Pieters *et al.*, 1997; Ryder *et al.*, 1997; Wieczorek and Zuber, 2001; Arai *et al.*, 2008 and references therein). A possible explanation for this difference is that the latest LMO liquids became denser and more Fe-rich after the removal of Mg-rich olivine and pyroxene, which allowed certain mafic minerals to float along with plagioclase (Wieczorek and Zuber, 2001). Alternative theories suggest underplating by mare basalt liquids (Head and Wilson, 1992) or that the lower crust is composed of various mafic intrusive rocks (Ryder and Wood, 1977) which could represent a phase of post-magma ocean serial magmatism (*e.g.* Warren, 1993; Ryder *et al.*, 1997; Longhi, 2003). One item that remains unclear is the crust-mantle distribution of primitive urKREEP.

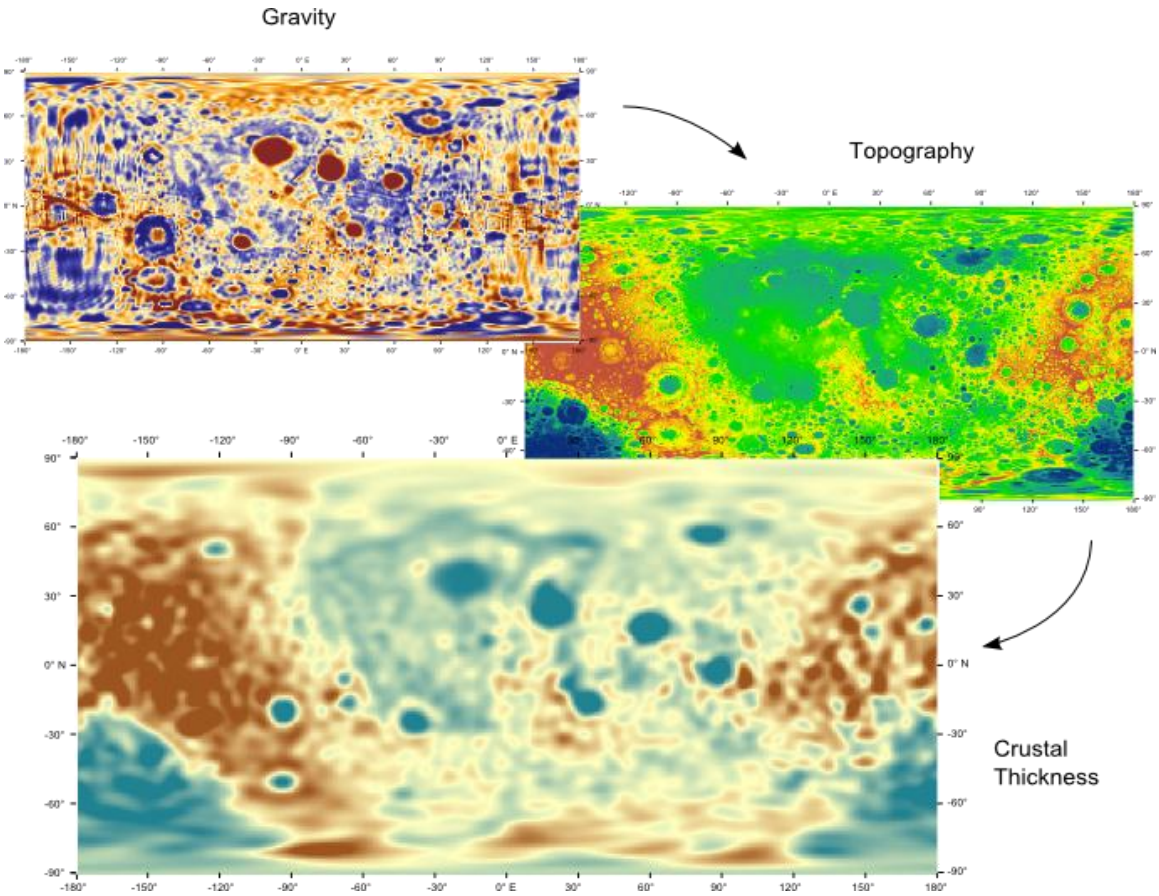

FIGURE 2.9 Flow diagram indicating the steps taken to produce a global crustal thickness model for the Moon. Global gravity datasets (*e.g.*, from Clementine, Lunar Prospector, Kaguya SELENE, and GRAIL) are combined with topographic datasets (*e.g.*, from Clementine, Kaguya SELENE, and LOLA), corrected, and inverted for crustal thickness (*e.g.*, Model 3 from Wieczorek *et al.*, 2006, shown here).

Although the LMO is a convenient and accepted framework for lunar crust formation, geophysical and petrologic studies have shown that the lunar crust is not simply stratified but highly variable both laterally and vertically. Based on remote sensing data from the Clementine mission, Jolliff *et al.* (2000) defined four geochemical terranes with distinct major and trace element abundances: the Procellarum KREEP Terrane (PKT), Feldspathic Highlands Terrane (FHT) (further subdivided into FHT-A, for "anorthositic," and FHT-O, for "other") and the South Pole Aitken Terrane (SPA or SPAT). Lateral crustal heterogeneity is also indicated by hemispherical asymmetry in crustal composition: whereas ferroan anorthosites are

thought to overlie a noritic lower crust (orthopyroxene + plagioclase) on the lunar nearside, the farside crust is proposed to consist of magnesian anorthosites overlying Mg-rich troctolites (olivine + plagioclase) (Takeda *et al.*, 2006; Arai *et al.*, 2008, Ohtake *et al.*, 2009, 2012). Furthermore, the nearly exclusive nearside distribution of basaltic maria, while not directly bearing on crustal composition, may stem from the same process that resulted in lateral heterogeneity.

Vertical variability in crustal composition further complicates the simple LMO differentiation story. Global remote sensing data shows that the highlands crust is not composed of extensive areas of anorthosite (*e.g.*, Lucey *et al.*, 1995), but that the largest areas of anorthosite are exposed in impact craters and basins, especially in rings formed during crater modification stages (Hawke *et al.*, 2003). This suggests that the original upper crust has been significantly reworked and modified by impacts and volcanism on various scales, and that the principal layer of anorthosite underlies impact-excavated megaregolith (Taylor, 2009) with a possible mafic "mixed layer" that represents a primordial, quenched LMO crust (Hawke *et al.*, 2003). In addition, the ejecta of large impact basins are more mafic than the surrounding highlands, as are the central peaks and peak rings of select complex craters (Pieters *et al.*, 1997). Similarly, the SPA basin floor is notably more mafic in composition than the surrounding FHT (Pieters *et al.*, 1997). These lateral and vertical complexities in crustal composition require further review and refinement of the simple LMO model for crustal formation.

Petrology of the lunar crust – inferences from sample studies

Previous studies of Apollo and Luna samples have organized pristine non-mare rocks into 3 broad groups: the ferroan anorthosite suite (FAS), the magnesian suite (Mg-suite), and the alkali suite (*e.g.* Warren, 1993; Taylor, 2009). As defined by Warren and Wasson (1978), 'pristinity' is a term used to distinguish those rocks that have survived significant modification (physically and chemically) by impacts. Fig. 2.10 illustrates the compositional and geochemical variations among the highlands lithologies, as well as the approximate locations of these within the crust.

Ferroan Anorthosite Suite (FAS)

Generally, the FAS rocks are composed of ~77 to 96 vol. % Ca-rich (anorthite) plagioclase feldspar (Fig. 2.12) having relatively high Al_2O_3 compositions (Wieczorek *et al.*, 2006). The mafic silicate minerals in the FAS have low Mg# (molar Mg/(Mg+Fe)), indicating the ferroan nature of the FAS (Taylor *et al.*, 1991; Wieczorek *et al.*, 2006). The FAS also display low concentrations of incompatible elements (*e.g.*, Th and La) and have large positive europium (Eu) anomalies (Taylor *et al.*, 1991). The FAS can be further subdivided on the basis of modal mineralogy and composition (*e.g.*, Taylor, 2009). For example, the pure anorthosite (PAN) has a plagioclase content of >95 vol. %, FeO <3 wt. % and an An_{70-90} plagioclase composition (*e.g.* Ohtake *et al.*, 2009). The range in compositions and ages displayed by the FAS suggests that they likely represent the primary crystallization products of the LMO (*e.g.* Norman and Ryder, 1979; Taylor, 2009).

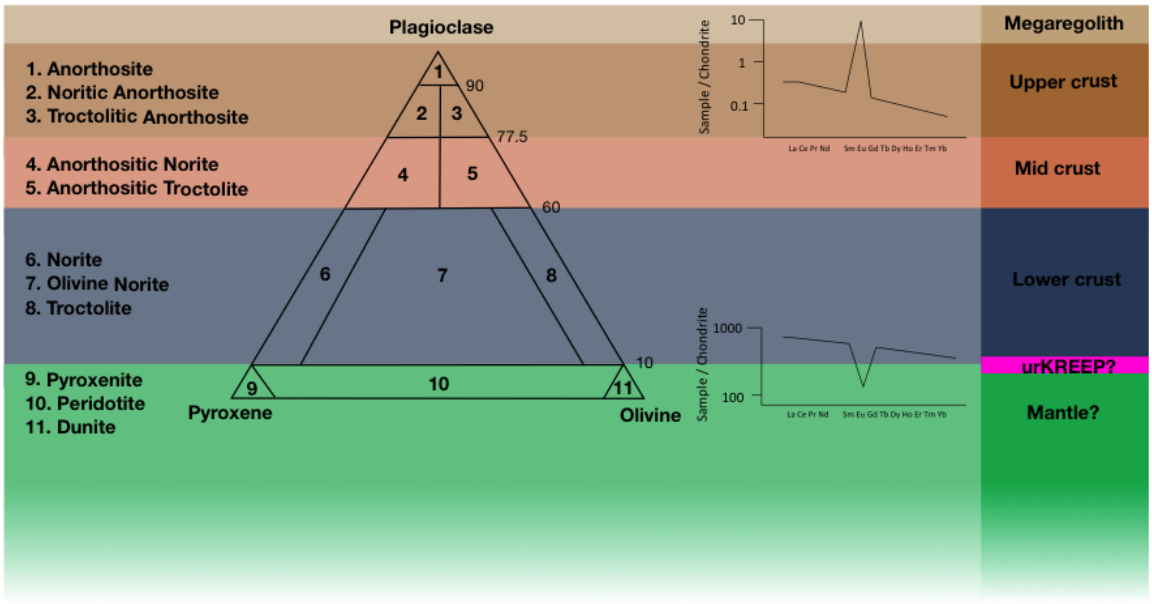

FIGURE 2.10 From left to right, the image illustrates the rock name, the corresponding plagioclase-olivine-pyroxene ternary composition diagram (where 90, 77.5, 60, 10 indicate the relevant % plagioclase), two rare earth element spider diagrams highlighting the difference in composition between the FAN and proposed super-KREEP (after Taylor, 2009) with respective positive and negative Eu anomalies, and finally where the rocks may be found within lunar crust-mantle stratigraphy. Color scheme is consistent throughout this chapter. Modified from Jolliff (2012).

Mg-suite

The Mg-suite lithologies contain less feldspar than the FAS (<80 vol. %, Fig. 2.12) (Taylor, 2009). The lithologies constituting the Mg-suite are norite, troctolite, and dunite. The Mg-suite is geochemically unusual in that it is relatively enriched in trace elements (*i.e.*, KREEP) indicating a highly evolved parental magma, but its Mg# (>64) suggest a primitive parental magma (Wieczorek *et al.*, 2006). Petrologic studies of the Mg-suite samples suggest that they represent intrusions into the primary lunar crust and are possibly the result of serial magmatism post-LMO crystallization (Taylor, 2009 and references therein). Two petrogenic models have been developed for the Mg-suite: Model 1 involves decompression melting and rising of highly magnesian early LMO cumulates, which assimilated with the late LMO urKREEP; Model 2 suggests that hybridized mantle cumulates and urKREEP were the source for Mg-magmas as a result of massive overturn (Shearer and Papike, 2005).

Alkali suite

The alkali suite includes KREEP basalt, alkali anorthosite, alkali gabbronorite, quartz monzodiorite, and felsite, all of which are rocks enriched in alkali elements (Taylor, 2009). The alkali suite contain ~50 vol. % plagioclase, with bulk Al_2O_3 ranging from 13 to 16 wt. % and Mg# between 52 and 65 (reviewed by Wieczorek *et al.*, 2006). This suite displays a typical KREEP incompatible element enriched signature (Taylor, 2009) (Fig. 2.12). Although most lunar basalt samples have a KREEP component, actual KREEP basalts are only found in the Apollo 15 sample collection (Wieczorek *et al.*, 2006). Petrological models evoke the possibility that the fractional crystallization of KREEP basalt created the cumulate diversity seen in the alkali suite samples, and that the parentage of KREEP basalt is more applicable to the alkali suite than the Mg-suite (*e.g.*, as shown by experimental studies of quartz monzodiorite) (*e.g.* Taylor, 2009). The alkali suite crystallization ages range from ~4.3 to 3.8 Ga, overlapping that of the FAS and Mg-suite (Wieczorek *et al.*, 2006).

A significant problem with these studies to date is that the sample collection is limited to rocks from the PKT, and it is unclear how well these lithologic groupings apply to the entirety of the lunar crust (*e.g.*, Cahill *et al.*, 2009). In order to better understand asymmetry in crustal thickness, determine its relationship

to chemical stratification, and gain better understanding of urKREEP chemistry and its distribution at the crust-mantle boundary, samples from all geochemical terranes and the full stratigraphy of the crust need to be collected. These data can also constrain the chemical and physical properties of the medium in geophysical models.

Using Impact craters as windows into the lunar interior

Impacts drill holes deep into the lunar subsurface, excavating and exposing this material in crater deposits and landforms. We have utilized equations, which are briefly described below, to calculate which craters or basins on the lunar surface may expose upper and lower crust material. For a more detailed discussion please refer to the Methodology section in Science Concept 3.

For simple craters (craters with diameter less than approximately 16–20 km), the transient crater diameter (D_{tc}) can be calculated using Equation (2.10), where D represents the final diameter of the crater (all in km):

$$D_{tc} = 0.84D \quad (2.10)$$

For complex craters, we utilized Equation (2.11) to determine the transient crater diameter (after Croft, 1985), where D_{sc} is the transition crater diameter from simple to complex craters (approximately 16–20 km on the case of the Moon) and all parameters are in cm:

$$D = D_{sc}^{-0.18} D_{tc}^{1.18} \quad (2.11)$$

The D_{tc} was then used in the following equations to calculate the maximum depth of excavation (d_e) and maximum depth of melting (d_m). These two key parameters were compared against three models of crustal thickness from Wieczorek *et al.* (2006) (as discussed in the Science Concept 3 methodology section).

Depth of excavation

Ejecta deposits are material mobilized from the site of impact onto the surrounding terrane. The ejecta material does not come from the full depth of the crater but rather from much shallower levels (Melosh, 1989). The maximum depth from which the ejecta material originates is determined by calculating the depth of excavation (d_e) (Equation 2.12: Croft, 1980; Melosh, 1989), which is important for determining the contribution of crust/mantle components. d_e is generally equal to one third of the transient crater depth d_{td}, or one tenth of the transient crater diameter D_{tc} (all in km):

$$D_e = 1/3 D_{td} = 1/10 D_{tc} \quad (2.12)$$

Maximum depth of melting

The maximum depth of melting (d_m) for complex craters, *i.e.*, those with diameters >16–20 km, is calculated by Equation (2.13) (after Cahill *et al.*, 2009), where D is the final rim diameter of the crater in kilometers:

$$D_m = 0.109 D^{1.08} \quad (2.13)$$

For all complex craters with a diameter >20 km listed in the Lunar Impact Crater Database (Losiak *et al.*, 2009, revised by Ohman, 2011), the proximity to the crust-mantle boundary was calculated by subtracting either the depth of excavation or depth of melting, from the pre-impact crustal thickness (as determined by each of the three crustal thickness models) (after Cahill *et al.*, 2009). Where a positive proximity means that d_e or d_m is located only within the crust and a negative proximity means that d_e or d_m may extend into the mantle.

Impact melt sheet

An impact melt sheet is formed due to the vast amount of kinetic energy generated during an impact, which melts the target lithology and any residual impactor material (*e.g.* Kring, 1995). In the case of complex (or larger) craters most of the melt pools inside the transient cavity of the crater and creates the central melt sheet, while some is deposited on crater walls or in terraces and a smaller proportion is mixed with broken up material and ejected from the crater. The maximum depth of melting allows consideration of a maximum depth of origin for the melt material.

Central peak

Central peaks are formed in complex craters. They result from the shock-compression of material directly beneath where the impactor hit, which rebounds or recoils back towards the surface, finally resting above the apparent crater floor (Fig. 2.11; Baldwin, 1974). As concluded by Cintala and Grieve (1998), the minimum depth of origin for a central peak coincides with the maximum D_m (Equation 2.13). Thus the maximum d_m can be used to determine where within the crust or mantle the central peak material has come from.

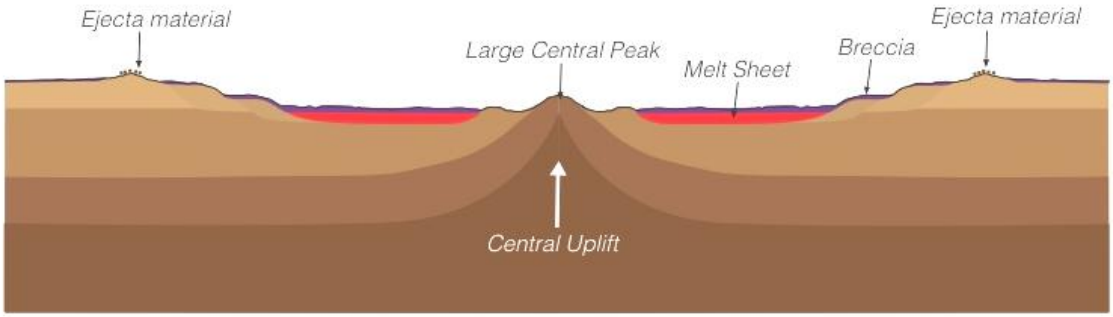

FIGURE 2.11 Schematic cross section of a complex crater with crater deposits and landforms identified. Notice that the central peak can contain outcrops of uplifted material from deeper stratigraphic levels than sampled elsewhere in the crater. Not to scale.

Central peak ring or basin inner ring

There are several hypotheses for the formation of peak rings within peak ring craters and multi-ring basins (Fig. 2.12). Unlike the case for central peaks where the maximum depth of melting likely corresponds to the minimum depth of origin for the peak material, after Cintala and Grieve (1998) the peak ring formation is considered to be intrinsically affected by impact melting. They conclude that the material for the peak ring likely does not come from the maximum depth of melting but from much shallower levels, and that this applies to peak ring basins and multi-ring basins.

However some workers have also proposed that the central peak ring is an enlargement of a central peak (*e.g.* Kring, 2005), thought to be formed from the collapse and spreading of a central peak if it has risen too far above the surface. Please note that the formation of rings in multi-ring basins is poorly understood and the reader is redirected to Pike and Spudis (1987) for a comprehensive discussion.

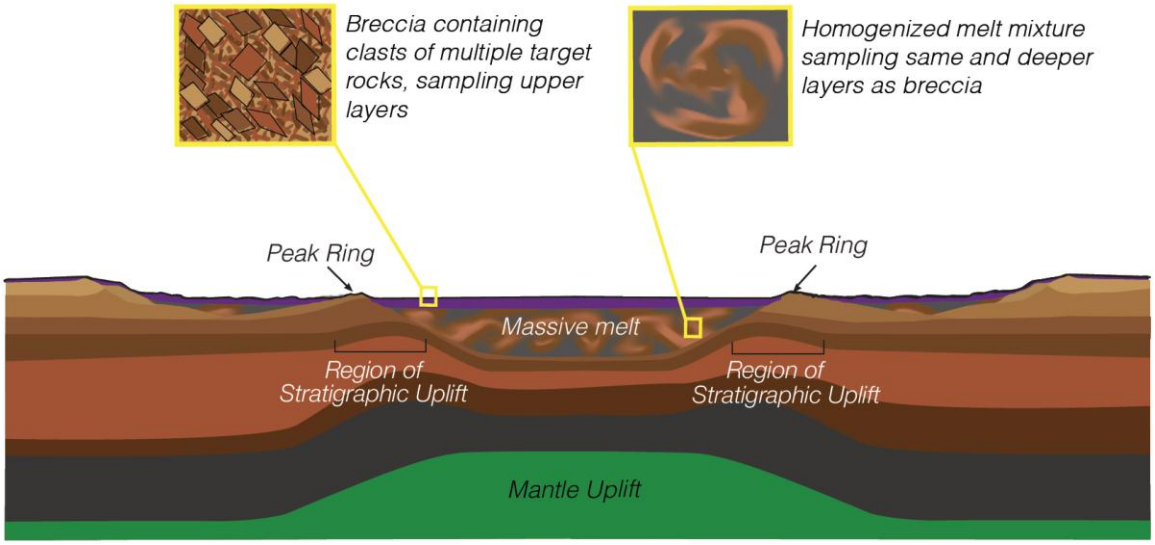

FIGURE 2.12 Schematic cross section of a peak ring basin (which is also applicable to a multi-ring basin). The figure illustrates that breccia and ejecta material can potentially contain material from all levels sampled by the crater. Note the homogenization of the crustal material from multiple stratigraphic levels in the massive melt sheet. Not to scale.

Requirements

Orbital Geophysics

Gravity Surveying

Surveying the gravitational field is the best way to characterize both regional and global crustal thickness variations. This will be completed to a high degree of spatial resolution (~27 km globally) by the current GRAIL mission (Zuber *et al.*, 2012; Hirt and Featherstone, 2012). Since this data can be obtained from orbit, it is not considered when selecting landing site locations.

In situ Geophysics

Seismology

While gravity surveys provide a direct measure of the subsurface mass concentration variation, the crustal thickness (H) itself is modeled from these surveys and requires anchor points where H is known to a higher degree of certainty. A passive seismic experiment can be used to invert for H both at the seismometer location and at surrounding locations where meteoroid impacts occur (Chenet *et al.*, 2006). To maximize the usefulness of these anchor nodes, they need to be positioned at locations representative of the 'typical' crustal thickness for each terrane (Jolliff *et al.*, 2000). Thus, a minimum of four seismometers is required (one in each terrane), and passive seismic experiments must be implemented concurrently to obtain maximum constraints for subsequent analyses. Active seismic experiments are not appropriate for this Science Goal as they do not provide information below ~500 meters depth (Watkins and Kovach, 1972).

EM Sounding

EM sounding can be used in conjunction with seismology to further constrain crustal thickness at the anchor points. Magnetotellurics (MT) is perhaps the most suitable method, as it does not require an orbital station (*c.f.*, Geophysical Methods). Detection of the shallow crust requires an EM field signal above 10 Hz, though well-documented fields on the Moon are ≤ 10 Hz in frequency (Grimm and Delory, 2010). Fortunately, solar wind fluctuations produce robust signals up to 100 Hz, allowing for detection of the crust-mantle boundary (Fillingim *et al.*, 2010). For Science Goal 2a, MT measurements must be conducted at the same location as the seismic experiments, but has no requirements of its own as to where the experiment should be done.

Sample Return

Landing sites should be selected to obtain samples that are representative of both the upper and lower crustal compositions laterally and vertically, specifically:

1. Rocks of both the upper (anorthosite) and lower (norite, troctolite, or gabbro) crust representing the full compositional range of crustal stratigraphy.
2. Rock samples from each of the four geochemical terranes (after Jolliff *et al.*, 2000).

In order to maximize the probability of successful sampling, selected landing sites should also meet the following criteria:

3. Outcrops and deposits of a specific basin should be known so that it is clear which crater or basin is being sampled.
4. Outcrops or deposits should be exposed at the surface and easily accessible.

Methodology

In situ Geophysics

The terranes (as identified by Jolliff *et al.*, 2000) were first traced out in ArcMap 10. To find regions of 'typical' crustal thickness, crustal thickness distributions were extracted and plotted in MATLAB to find the mean and the standard deviation of crustal thickness for each terrane individually (Fig. 2.13). The Model 3 total crustal thickness model data from Wieczorek *et al.* (2006) was used, which is derived from Clementine topography, and Lunar Prospector LP150Q gravity model data. This model will be replaced with a model which makes use of LOLA topography and GRAIL data, when the latter becomes available. ArcMap 10 was then used to extract locations where crustal thickness is within one standard deviation (σ) of the mean crustal thickness for each terrane, to map areas of 'typical' crustal thickness.

As EM sounding can be carried out anywhere on the lunar surface, there is no mapping required for this method. This means that Fig. 2.14 is the only map for the geophysical methods within this Science Goal.

Sample Return

In the context of the NRC report, landing site candidates require exposures of rocks that have originated from deep within the Moon. To fulfill the requirements outlined above, only those craters and basins that potentially sample the full stratigraphy of the lunar crust have been considered. We have used the following approach, discussed in more detail in Science Concept 3 (*e.g.*, Flahaut *et al.*, 2012).

1. We utilized the Lunar Impact Crater Database (Losiak *et al.* 2009, revised by Ohman, 2011) to identify all craters and basins that may expose the lower crust in either ejecta blankets, melt sheets, or central uplifts (*i.e.*, central peaks and peak rings). We sought to identify those craters and basins that tapped both the lower and upper crust, assuming that a crater sampling the lower crust must have sampled the upper crust as well.
2. Using Equations 2.10–2.13 (outlined above), we identified all craters or basins that may theoretically expose lower crustal material in their ejecta.
3. Melt depth proximity calculations were used in combination with (1) to determine where the lower crust may be sampled in impact melt sheets or in central peaks and peak rings (if preserved).
4. The calculations described above are theoretical and as such LROC Quickmap was used to verify whether craters/basins did indeed preserve their central peaks or peak rings.

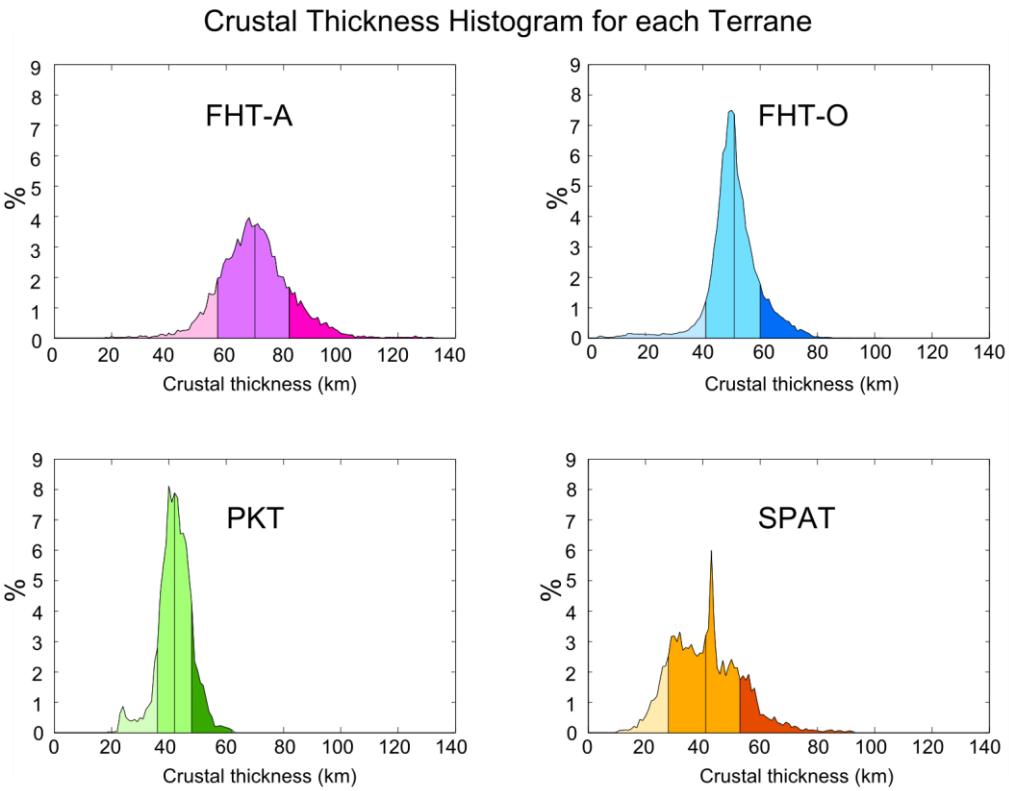

FIGURE 2.13 A histogram showing the frequency distribution of 'thin', 'typical', and 'thick' crustal thickness for each of the terranes, as defined in Jolliff *et al.* (2000). 'Typical' crustal thickness is defined as ±1σ of the mean crustal thickness of the terrane (middle vertical line). Lighter shades denote 'thin' crust for each terrane; darker shades denote 'thick' crust for each terrane. Color scheme is also used in Fig. 2.16

However, there are a number of sampling details that must be considered:

1. The calculations for d_m have been used here to determine where the material for the peak rings comes from. However, there is significant debate regarding how the rings are formed, which in turn dictates what depth the material comes from. Therefore the rings which have been identified here as potentially sampling the lower crust should be treated with caution.
2. Only lower and upper crustal exposures within basins are considered. As an example, Imbrium has a basin diameter of ~1160 km and is theoretically likely to contain lower crust and mantle material in its ejecta deposits, melt sheet or uplifted central peak or peak rings. However, Imbrium does not have a well preserved central peak or peak ring, as most of the melt sheet has been covered with mare basalts and megaregolith. Thus it is likely that samples of mantle material may be preserved within the basin itself, but most are likely not available for easy sampling and would be difficult to identify. On the other hand, ejected mantle material may be well preserved given the relative age of the basin, but the temporal connection between ejected samples and specific impacts is difficult to verify.
3. As of yet there are no contour maps for ejecta material on the Moon, and modeling has suggested that deeper material is more likely to be exposed closer to the central uplifts of craters and basins. Therefore our focus is on sampling the rim ejecta material, as material further away from the crater is more likely to be buried by regolith (which is particularly true for older craters).
4. Similarly, larger craters and basins are filled with younger volcanic deposits that obscure the underlying melt sheet. Thus the most optimal place to sample the melt sheet is where it is preserved in crater walls or terraces.

5. In cases where the central peak or peak ring are preserved, there are likely to be steeply inclined outcrops of rock that are good places to sample either directly or in debris at the base of the uplift.

Suggested Landing Sites

In situ Geophysics

Locations where crust is 'thick' (>1σ from the mean), and 'thin' (< 1σ from the mean) are shown in Fig. 2.14 as darker and lighter shades respectively. In accordance to the geophysical requirements, one seismic station needs to be placed within each of the terranes, and at a location with 'typical' crustal thickness, which is defined as within 1σ of the mean modeled crustal thickness.

Sample Return

Locations that satisfy the above requirements are shown in Fig. 2.15. All results are displayed in Table A2.1. Based on proximity calculations, the following craters (identified in Fig. 2.15) have ejecta potentially containing lower crust material: Nectaris, Orientale, South Pole-Aitken, Ingenii, Poincare, Antoniadi, and Minkowski (the latter four are located within SPA). Figure 2.17 shows craters and basins that may have lower crustal material in their melt and preserved central peaks (*e.g.*, Humboldt, Zeeman). Figure 2.17 also shows craters and basins that may have lower crust material in their melt and preserved peak rings (*e.g.*, Schrödinger, Orientale, Moscoviense). As noted above, our recommendation is to sample at least one crater or basin within each terrane; however, note that no craters were identified within the PKT according to our method. We do not feel that this is a drawback, as Apollo breccias from the PKT may contain clasts of crustal lithologies.

It should be noted that only specific areas within craters and basins can be sampled to attain upper and lower crustal compositions. Examples of complex crater (Humboldt) and multi-ring basin (Orientale) sample locales are illustrated below. However it is important to recall that the formation of peak rings is poorly understood and that the application of proximity calculations to determine the depth of origin of peak ring material is somewhat ambiguous.

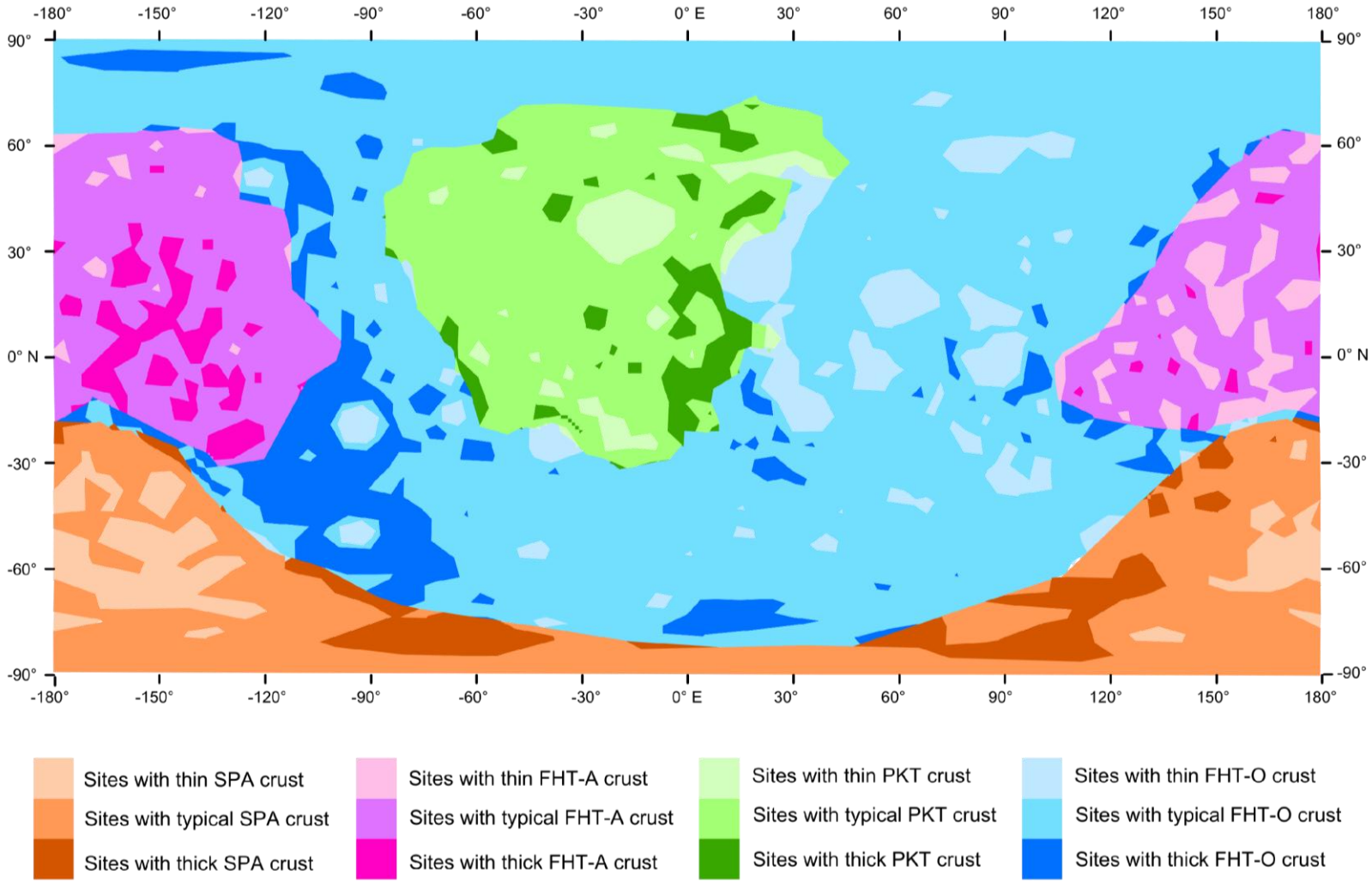

FIGURE 2.14 Map showing the areas of 'thin', 'typical', and 'thick' crustal thickness for each of the terranes, as defined in Jolliff *et al.* (2000), to identify sites where it would be preferable to place seismometers to aid our understanding of Science Goal 2a. Lighter shades denote 'thin' crust for each terrane; darker shades denote 'thick' crust for each terrane. This map is also used for heat flow measurements, under Science Goal 2c and 2d, as this experiment also requires 'typical' crustal thickness, but with additional requirements. The colors of defined regions correspond with the colors of the histogram in Fig. 2.15.

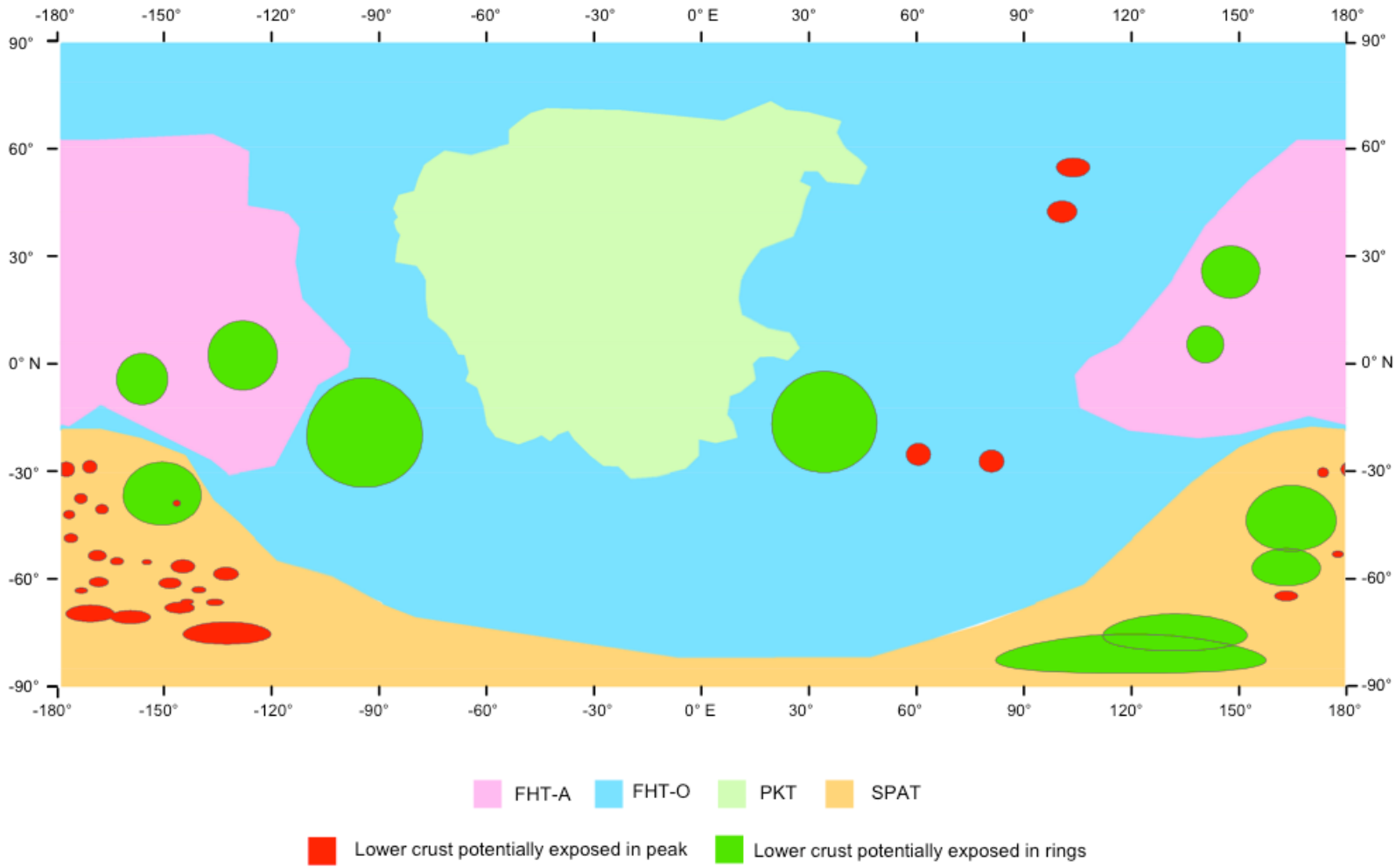

FIGURE 2.15 Map of all craters and basins that may contain lower and upper crustal material in their preserved impact melt, central peaks, or peak rings. Terrane boundaries of Jolliff *et al.* (2000) have been added to highlight where lower crustal rocks could be sampled within each terrane. Note that the filled ellipses do not mean that lower crust can be sampled everywhere within that ellipse (*c.f.*, Figs. 2.18 and 2.19).

Example 1: Humboldt

Humboldt is presented here as an example of where different lithologies are present within a complex crater. Humboldt has a preserved central peak (Fig. 2.16) and within this crater it should be possible to sample ejecta on the crater rim, melt (as this crater has not been flooded with mare basalt), and the outcrops of the central peak. An example landing site (pink star) been added for perspective; this site could potentially contain exposures of the lower crust and melt sheet.

Example 2: Orientale

Orientale basin has been selected as an example of where to sample the crust within a multi-ring basin (Fig. 2.17). Due to the formation mechanisms of multi-ring basins, it is unlikely that all of the rings contain material from the maximum depth of melting; the inner rings are the most plausible candidates. Figure 2.17 illustrates that though most of the Orientale basin has been flooded with mare basalts that have covered most of the melt sheet, there may be melt preserved as ponds on basin walls. The inner rook ring of Orientale is very likely to contain exposures of the LMO-generated crust beneath a megaregolith (*e.g.*, Hawke *et al.*, 2003).

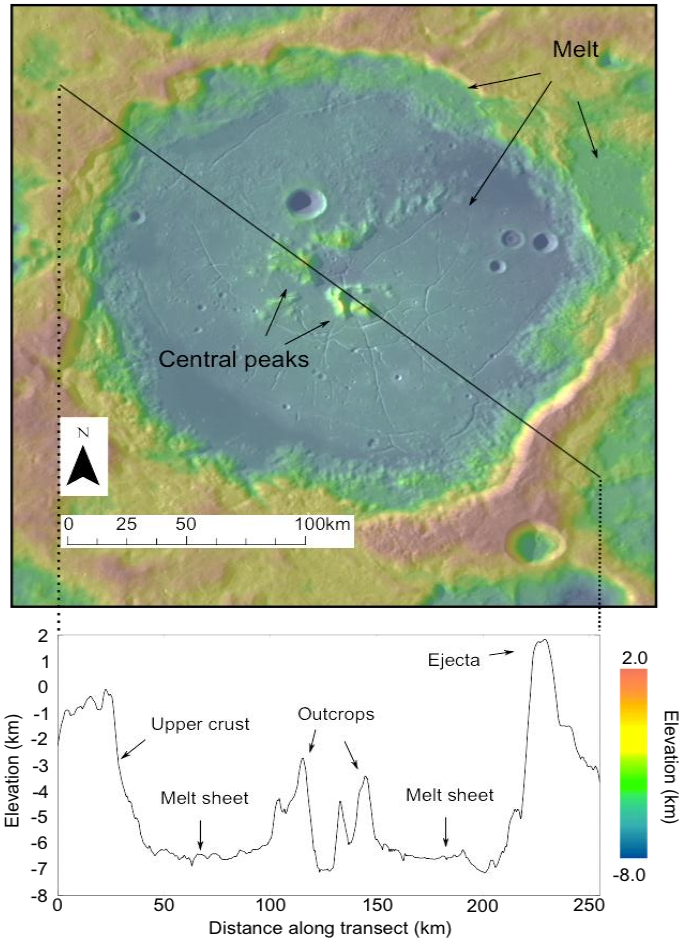

FIGURE 2.16 LROC WAC Quickmap image of Humboldt crater located at 26.8˚ S, 80.8˚ E. The topographic profile was obtained from Quickmap tools using GLD100; vertical exaggeration is ~20:1. The central peak outcrop and melt pockets could be sampled to obtain samples of the lower crustal composition and should be sampled.

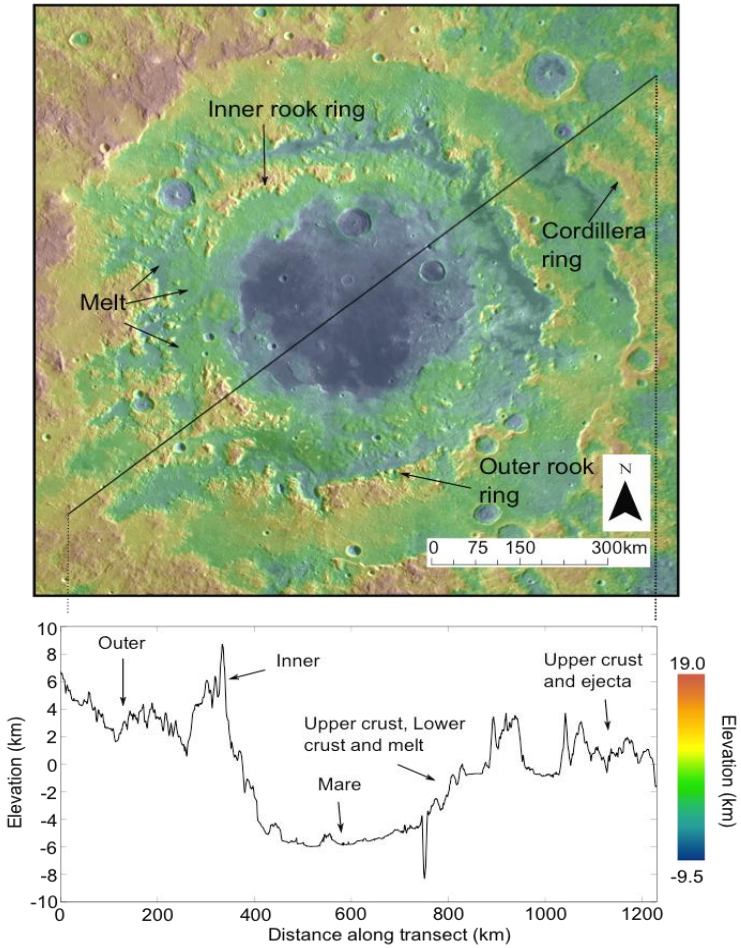

FIGURE 2.17 LROC WAC Quickmap image of Orientale basin located at 19.6˚ S, 94.0˚E. The topographic profile was obtained from Quickmap tools which used GLD100 data source; vertical exaggeration is ~ 10:1. Peak rings may potentially contain outcrops of material uplifted from the lower crust.

Conclusions

The final map combining the geophysical and sample return elements for Science Goal 2a is shown in Fig. 2.18. In this map, the highlighted areas are the craters that can be visited as part of the sample return element of this Science Goal, bearing in mind that only one crater needs to be visited within each terrane. As there are no suitable sites for sample return within PKT, it is suggested that the geophysical package that needs to be placed within this terrane is placed as far away as possible from the packages in the other terranes. This would increase the global coverage of the seismic network, and provide information regarding mantle structure. For the highlighted regions in other terranes, there are regions with typical crustal thickness which are suitable for the geophysical package.

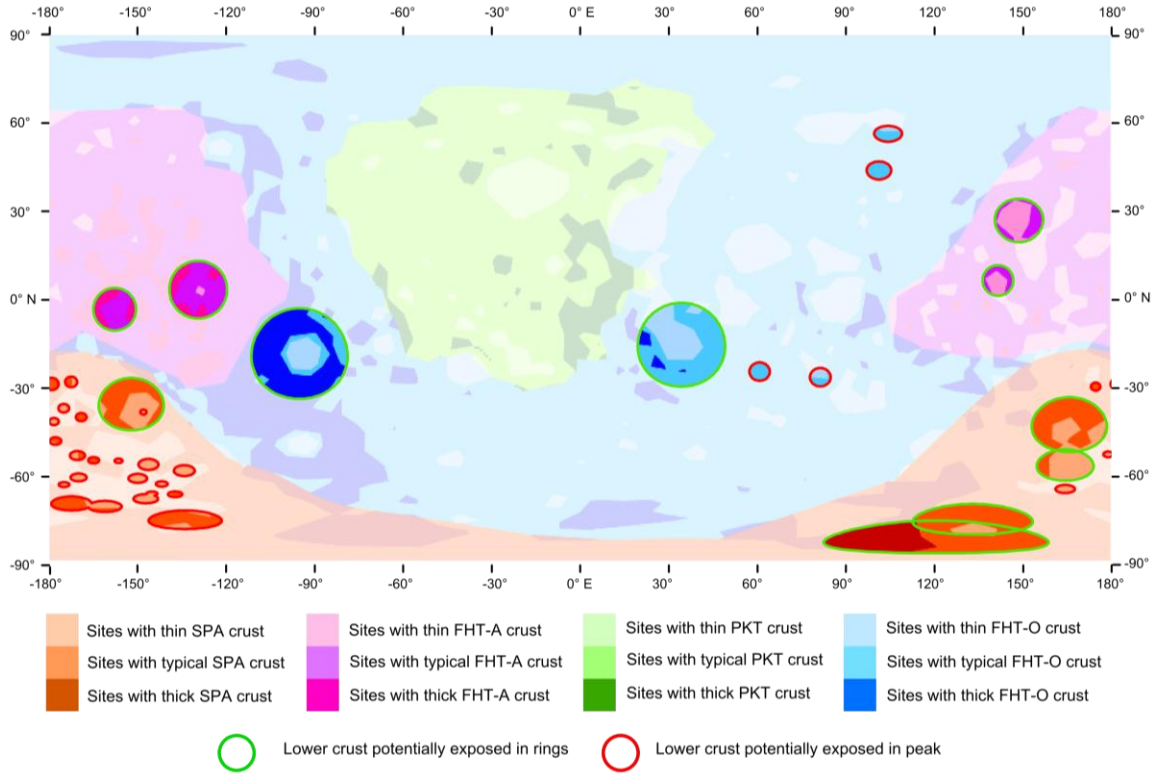

FIGURE 2.18 Final landing site map for Science Goal 2a. The final geophysical landing site map is superimposed onto the final sample return landing site map. Notice there are craters and basins suitable for sample return for this Science Goal present in all of the terranes (except PKT) with some located in the highlands, incorporating areas of typical crustal thickness suitable for meeting the geophysical requirements.

SCIENCE GOAL 2B: CHARATERIZE THE CHEMICAL/PHYSICAL STRATIFICATION IN THE MANTLE, PARTICULARLY THE NATURE OF THE PUTATIVE 500-KM DISCONTINUITY AND THE COMPOSITON OF THE LOWER MANTLE.

Introduction

Compared with the wealth of data concerning the lunar crust, relatively little is known about the composition and structure of the lunar mantle. Apollo, Luna and meteoritic samples contain no direct mantle lithologies and Apollo seismic data revealed only some details about the upper and middle mantle. The close spacing of the Apollo seismic array made it such that mantle structure outside the network extent could not be resolved (R. Weber, pers. comm.). Additionally, current seismic data is not sufficient to resolve the structure of the middle and lower mantle (Nakamura, 1983).

The nature of the lunar mantle is highly dependent on details regarding the lunar magma ocean (LMO) hypothesis, many of which are debated and/or unknown. Mantle composition is governed by the bulk composition of the Moon and the extent to which the LMO differentiated. Mantle stratification is likewise dependent on the depth of the LMO, in addition to the degree of stratification during differentiation and the extent and scale of cumulate overturn. The distribution of deep moonquakes (DMQ) and high frequency teleseismic events (HFT) indicate at least some mantle stratification with low-velocity zones and structural discontinuities proposed at various mantle levels, including a major 500-km discontinuity. However, many of the models that arrived at these features are non-unique, suffer from a dearth of data, or are speculative, and even those that are more highly resolved lack key constraints.

Science Concept 3 (Science Goal 3a, b, c), Science Concept 5, and Science Concept 6 (Science Goal 6c) have proposed to sample lithologies that will address the composition of the mantle. Sample locations presented here should be used in conjunction with those other proposed landing sites in order to more readily address Science Goal 2b. No other Science Concepts have proposed geophysical landing sites that will address the structure of the mantle.

Background

Lunar Magma Ocean (LMO) and Cumulate Overturn

The lunar magma ocean and subsequent cumulate overturn are discussed in depth in the general background, and only summarized here. While the nature of the lunar mantle is subject to significant debate, it is generally agreed that the initial physical and chemical stratification was produced by differentiation from a magma ocean (*e.g.*, Shearer and Papike, 1999). Prior to any overturn, the LMO cumulate pile would have been zoned from Mg- and olivine-rich at its base to Fe-, Ti-, KREEP-, and pyroxene-rich at the top, with a feldspathic crust. Subsequent overturn driven by gravitational instabilities (Hess and Parmentier, 1995) may have resulted in the delivery of dense ilmenite- and KREEP-bearing plumes to the middle and lower mantle, creating a "hybrid" heterogeneous mantle source for mare basalts and pyroclastic glasses, and perhaps resulting in an ensuing series of positively buoyant plumes (e.g, Singletary and Grove, 2008). These data all indicate that the global zoned structure of the early mantle has been highly disrupted after its initial solidification, but the extent and scale of mantle heterogeneity is as yet unclear.

High-Frequency Teleseismic (HFT) Events and Upper Mantle Structure

Twenty-eight out of the ~12,500 seismic events recorded by the Apollo Passive Seismic Experiment (APSE) were classified as "high-frequency teleseismic events," characterized by their high-frequency nature, well-defined P- and S-wave arrivals, and higher-magnitude energy release (Nakamura *et al.*, 1974, 1979; Nakamura, 1977; Oberst, 1987). Unlike deep moonquakes, their occurrence is not aligned with tidal periodicities (Nakamura *et al.*, 1974; Nakamura, 1977), but is rather statistically correlated with the sidereal month, such that HFT events tend to occur during a specific lunar orientation relative to the stars (Frohlich and Nakamura, 2006).

The source depths for HFT are poorly resolved. Though some studies locate epicenters in the shallow mantle at ~50–200 km depth (Nakamura *et al.*, 1979; Khan *et al.*, 2000; Fig. 2.21), it is not possible to exclude a shallower or even surficial origin for HFT (Nakamura *et al.*, 1974; Nakamura, 1977; Frohlich and Nakamura, 2006; Kawamura *et al.*, 2008) even though their seismic record is markedly different from known meteorite impacts (Nakamura, 1977; Nakamura *et al.*, 1979). If HFT events do indeed represent "shallow" moonquakes, it suggests that only the upper mantle of the Moon concentrates significant tectonic stresses (occasionally exceeding 100 MPa) required to cause them (Nakamura *et al.*, 1979; Oberst, 1987). The accumulation of such large stresses could relate to thermal changes in the lunar interior or long-lived heterogeneities from large impact basins (Nakamura *et al.*, 1979). Alternatively, Frohlich and Nakamura (2006) note the sidereal periodicity of HFT and suggest the possible influence of extra-Solar-System meteorites or nuggets of strange quark matter in triggering or causing HFT. Therefore, the implications of HFT for upper mantle structure are unclear. Unfortunately, the resolution of their source depths would require an unreasonable number of closely spaced seismometers (*c.f.*, Requirements-Geophysical).

500-km Seismic Discontinuity

Early interpretations of Apollo-era seismic data suggested the presence of a significant discontinuity around 500 kilometers depth as an explanation for a sharp increase in P- and S-wave velocity (Goins *et al.*, 1981b; Nakamura *et al.*, 1982; Nakamura, 1983; Wieczorek *et al.*, 2006 and references therein). This discontinuity has been interpreted to represent a major compositional boundary (*e.g.*, Goins *et al.*, 1981b) or a mineralogical phase transition (Wieczorek *et al.*, 2006 and references therein), though the latter case is less plausible to explain the observed velocity increase (*e.g.*, Hood and Jones, 1987). A significant compositional change between the upper and middle mantle may be explained in four ways (Wieczorek *et al.*, 2006):

1. The 500 km discontinuity represents the base of melting and differentiation in the LMO (*e.g.*, Mueller *et al.*, 1988);
2. The lunar mantle was compositionally zoned during accretion, with refractory Al- and Mg-rich compositions concentrated in the lower mantle (Hood and Jones, 1987; Mueller *et al.*, 1988);
3. The discontinuity represents the boundary between olivine- and orthopyroxene-rich cumulates formed in the LMO (Wieczorek *et al.*, 2006 and references therein), though later cumulate overturn is thought to have modified this configuration (e.g, Hess and Parmentier, 1995);
4. The discontinuity could represent the base of melting to produce mare and pyroclastic volcanic products, in which case it may be a local feature of the PKT (Wieczorek and Phillips, 2000).

However, some early work noted the relatively weak evidence for the boundary, arguing that such a mantle transition zone may be "gradual or discontinuous" (Nakamura, 1983). More recent seismic inversions have alternately supported (Khan *et al.*, 2000; Khan and Mosegaard, 2001) or questioned (Longonné *et al.*, 2003; Khan *et al.*, 2007) the existence of the discontinuity. It has also been suggested that the 500-km discontinuity may be an artifact of the original data processing (R. Weber, pers. comm.). In contrast, if the seismic discontinuity is real, then the small aperture of the Apollo seismic network limits any global interpretations (*e.g.*, Wieczorek and Phillips, 2000). Without more extensive seismic coverage, it is impossible to determine whether or not the discontinuity exists and if it is a global or regional feature.

We also note that various geophysical analyses of the Moon (especially seismology and EM sounding) suggest the presence of other major discontinuities or low-velocity zones in the lunar mantle, but many of these models are non-unique and relate to differences in datasets used to invert for mantle structure (*e.g.*, the number of deep moonquake source events utilized). The 500 km discontinuity has received particular attention because it is a feature common to many models for the lunar interior and therefore we restrict our discussion to it for brevity.

Deep Moonquakes, Mantle Asymmetry, and the Lower Mantle Attenuation Zone

One discovery in the Apollo seismic data was the recognition of deep moonquakes (DMQ), which occur in clusters or "nests" at depths of 800–1000 kilometers (Nakamura *et al.*, 1982). Nearly all of these events were recorded on the lunar nearside, with the exception of at least one event (termed A33), and their occurrence coincides with cyclic tidal periodicities (Goins *et al.*, 1981b; Nakamura, 1983; Bulow *et al.*, 2007). The asymmetric distribution of DMQ can be explained in two ways: either farside DMQ were attenuated in the lower mantle before reaching the Apollo seismic network (Nakamura, 2005), or the lunar farside is aseismic, in which case DMQ distribution may be related to other nearside-farside asymmetries (such as the distribution of mare basalts: Qin *et al.*, 2012) (Fig. 2.19).

Recent work has focused on reconciling the two end-member cases by focusing on the causes of DMQ. Given the challenge of fracturing rock at the high confining pressures indicated by their source depths, Frohlich and Nakamura (2009) suggested that DMQ could be caused by tidally-driven fluid or melt migration along pre-existing fractures, possibly assisted by fatigued and weakened lower-mantle material. Further strength reductions of lower mantle material may also be accommodated by phase transitions and associated transformational faulting (*e.g.*, Weber *et al.*, 2009).

Other workers have similarly suggested that a lower-mantle, partially-melted attenuation zone exists (also supported by seismic and LLR data: Nakamura *et al.*, 1973; Williams *et al.*, 2001; Khan *et al.*, 2004), but is asymmetrically distributed on the nearside and is responsible for the observed DMQ distribution (Qin

et al., 2012). The correlation between DMQ and mare basalt distributions, therefore, may be a function of a volatile-rich plume (Saal *et al.*, 2008) that rose in a single hemisphere (Zhong *et al.*, 2000), erupted mare material, cooled, and sank. Since this material can deform relatively easily (Frohlich and Nakamura, 2009), it provides a convenient source region for DMQ (Qin *et al.*, 2012). However, many of these suggestions are purely speculative (Frohlich and Nakamura, 2009) or rooted in highly specified models of mantle processes (Zhong *et al.*, 2000) and thus require significantly better-resolved geophysical data to verify.

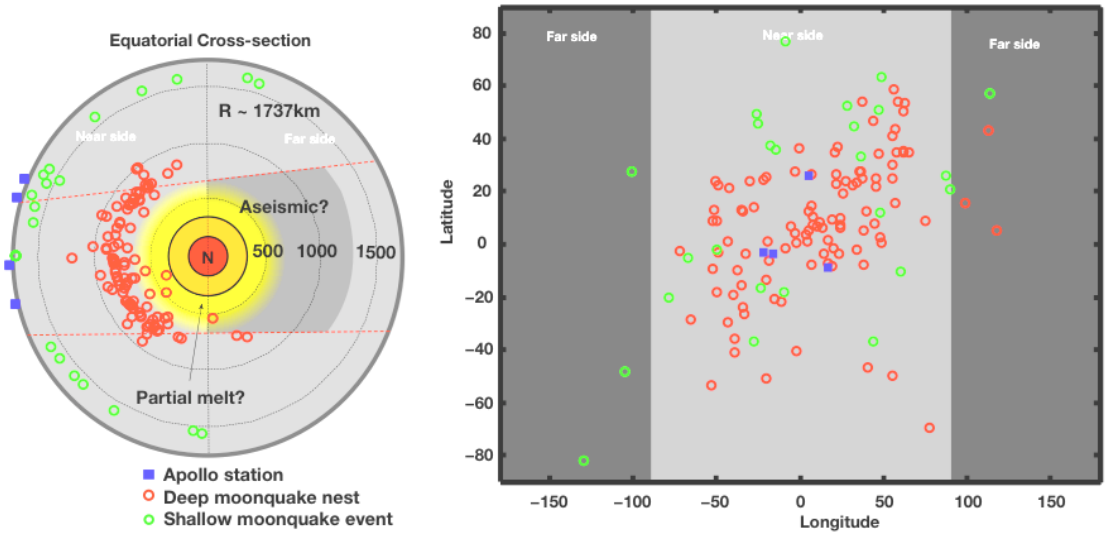

FIGURE 2.19 Summary of the three-dimensional distribution of Apollo seismic stations, deep moonquake nests (Nakamura, 2005) and shallow moonquake events (Nakamura, 1977). Left diagram shows the depth-longitude distribution (NOT a projection of the points onto the equatorial plane); grey concentric circles are lines of equal radial distances from the center of the Moon (500, 1000, 1500 km respectively). Right diagram shows the latitude-longitude distribution.

Recent studies have focused on the optimization of a seismic configuration to improve upon the Apollo Network and to increase both lateral and vertical seismic coverage (Yamada *et al.*, 2011; Hempel *et al.*, 2012). This work shows that the Apollo instruments were not theoretically capable of detecting deep moonquakes that occurred on the farside (Fig. 2.20; Hempel *et al.*, 2012). Therefore, any new seismic network must ensure global coverage of deep moonquakes to address questions regarding lower mantle seismicity and asymmetry. With sensitivity of current instruments, the minimum number of stations required for global coverage is a four and they must be equally spaced stations on the lunar surface (*i.e.*, a tetrahedron) (Fig. 2.22; Hempel *et al.*, 2012).

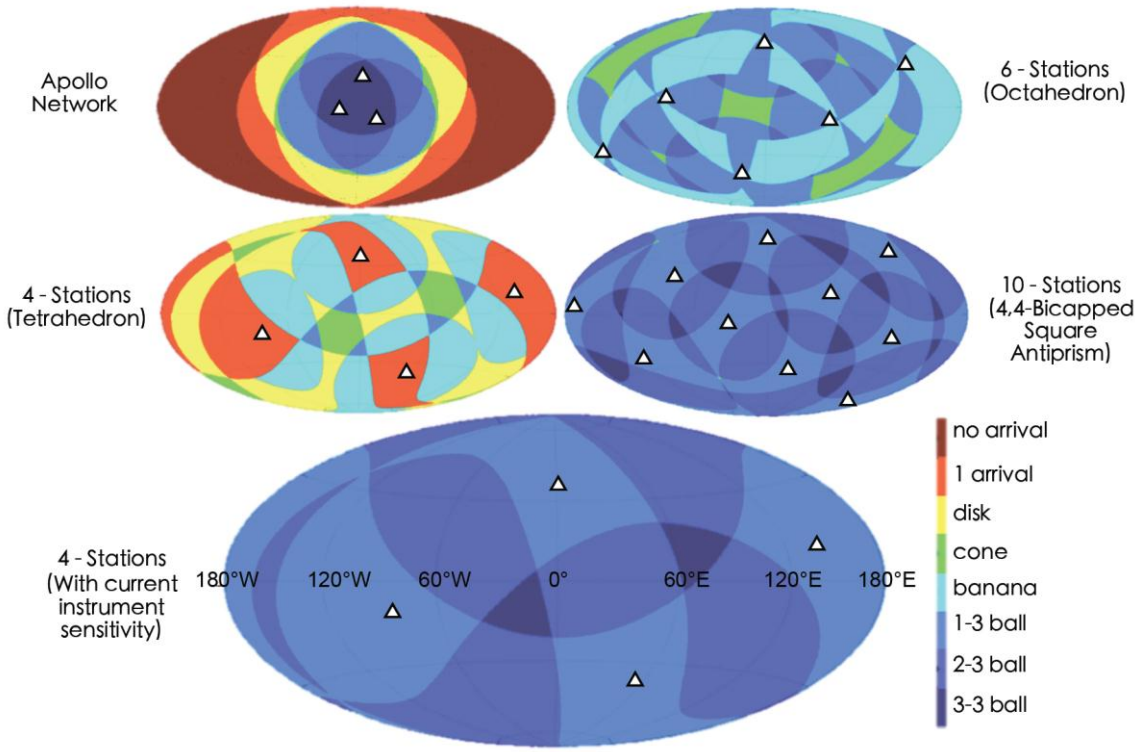

FIGURE 2.20 Proposed seismic configurations and their coverage. White points are positions of seismometers. The top four maps show different networks of seismometers with the same sensitivity as Apollo instruments. The bottom map shows the coverage of a four-station network using modern seismometers. Red indicates regions where if a deep moonquake occurs, no station or only one station will detect it. Yellow, green and the lightest blue shade indicate regions where moonquakes will be located as a probability disk, cone, or banana shaped region. The three darkest shades of blue indicate regions where deep moonquakes will be located accurately in a spherical region with decreasing uncertainty (Hempel *et al.*, 2012).

Inferences from sample studies

Much of the evidence for mantle cumulate overturn has come from the geochemical study of returned lunar samples (Apollo, Luna) and lunar meteorites. Mantle overturn is thought to have created a heterogeneous mantle, a conclusion partially derived from geochemical studies of mare basalts and pyroclastic glasses (*e.g.*, Grove and Krawczynski, 2009), and from the heterogeneous concentrations of volatiles (OH, F, Cl) in these samples (*e.g.*, McCubbin *et al.*, 2010).

Pyroclastic deposits

Pyroclastic deposits on the moon are thought to be the product of fire-fountaining volcanism (*e.g.*, Wieczorek *et al.*, 2006; Fig. 2.21). They are manifested as glass beads on the lunar surface of varying colors and compositions. They are envisioned to have formed by the ascent of magmas at temperatures >1450 ˚C (*e.g.*, Elkins-Tanton *et al.*, 2003) that were ejected into the cold, dry, vacuum of the Moon forming quenched glass droplets (Grove and Krawczynski, 2009) (Fig. 2.21). The volcanic fire fountaining is also manifested in dark mantle deposits, *e.g.*, Apollo 17 orange and black glasses (*e.g.*, Wilhelms and McCauley, 1971; Head, 1974).

Gaddis *et al.* (1985) described how lunar pyroclastic deposits (LPDs) vary in areal extent from <1 km^2 to >49,000 km^2. This is important as different eruptive styles can be given to LPDs based on their areal extent, as well as their morphology, vent size and type (*e.g.*, Head and Wilson, 1979). The larger LPDs are thought to be the product of continuous eruption of volcanic materials, in a Hawaiian-style 'fire fountaining' (Wilson and Head, 1981). It has also been proposed that these eruptions are likely to preserve

the primitive signature of magmatic materials (Head and Wilson, 1979). In contrast, a more intermittent, Vulcanian-style eruption is proposed to have produced the smaller LPDs (<200 km^2) (Head and Wilson, 1979). In this type of eruption, rising volatile-rich lavas are likely to incorporate and assimilate country rocks en-route to the surface.

The compositions of ultramafic glasses returned by the Apollo missions are unique in relation to those found on the Earth. They record TiO_2 contents ranging from <0.25 to >16 wt. % (Grove and Krawczynski, 2009), and are more ultramafic than mare basalts and terrestrial lavas with combined MgO and FeO contents >35 wt. % (Grove and Krawczynski, 2009). Recent studies of melt inclusions in high-Ti glasses in Apollo 17 soil sample 74220 show that parental magmas may have contained up to 400 ppm H_2O (Hauri *et al.*, 2011). The compositional diversity displayed by the lunar ultramafic glasses requires that the source regions for their parental magmas are heterogeneous with respect to TiO_2, Al_2O_3, FeO and MgO.

The source depths of the picritic glasses have been estimated from experimental studies and range from ~250 km to as deep as ~1000 km, and generally from 200 to 400 km (Delano, 1986; Grove and Krawczynski, 2009; Longhi, 1992). Such depths imply that the source of the parental magmas is in the upper mantle, but it remains unclear where in the magma-ocean cumulate pile these magmas were derived from.

Mare basalts

Lunar basalts are concentrated on the nearside in and around the PKT, and are significantly less extensive on the farside (Lucey *et al.*, 2006). Mare basalts display a wide range in TiO_2, K_2O, Al_2O_3, FeO and MgO contents (refer to Science Concept 5 for a more detailed description of mare basalt variability). The diversity of TiO_2 content within these samples is classified as high-Ti (>8 wt%), low-Ti (1–4 wt %) and very low-Ti (<1 wt%). Like the pyroclastic glasses, the compositional diversity in mare basalts suggests a heterogeneous source region for their parental magmas. The depth of derivation for mare basalts is considered to be < 250 km (thus in the uppermost parts of the lunar mantle) (Longhi, 1992, 1995; Thacker *et al.*, 2009).

Based on radiometric age dating of Apollo mare basalt samples, mare volcanism was thought to extend from ~3.1 to 3.9 Ga (Nyquist and Shih, 1992). Since the Apollo missions there has been much focus on crater counting to determine model ages of unsampled mare basalts (Boyce *et al.*, 1974; Heisinger *et al.*, 2000, 2003, 2010, 2011; Young, 1977). These data suggest that the youngest mare basalts are ~1.1 Ga old (Hiesinger *et al.*, 2008), and are located in the Aristarchus Plateau (Heisinger *et al.*, 2010) and Kepler crater (Morota *et al.*, 2011).

Cryptomare

Cryptomare are thought to be extensive mare basalts that have been buried by impact ejecta and regolith (Wieczorek *et al.*, 2006). They have been identified within dark mantle deposits surrounding impact craters and are considered to be the products of large scale ancient (Pre-Nectarian >3.8 Ga) basaltic volcanism (*e.g.* Hawke *et al.*, 1990, Head and Wilson, 1992). There is no direct evidence for the composition of cryptomare as none were sampled during Apollo or Luna missions. However, the basaltic lunar meteorite Kalahari 009 has a radiometric crystallization age of 4.35 Ga, consistent with cryptomare model ages and a VLT composition consistent with remote sensing spectra of cryptomare (Terada *et al.*, 2007). Because these deposits have not yet been sampled, their source depths remain unclear.

An important caveat to come from the study of both picritic glasses and basalts is that their high pressure multiple saturation points (thought to indicate potential source depths) do not necessarily correspond for compositionally similar lithologies. For example, experimental studies of TiO_2 basalts indicate shallow depths of origin but cannot explain the origin of the high TiO_2 picritic glasses (Grove and Krawczynski, 2009). Cumulate mantle overturn may help address this issue but it also raises its own questions such as the mechanisms involved in sinking titanium rich cumulates and the heat sources involved in melting events (Elkins-Tanton *et al.*, 2003).

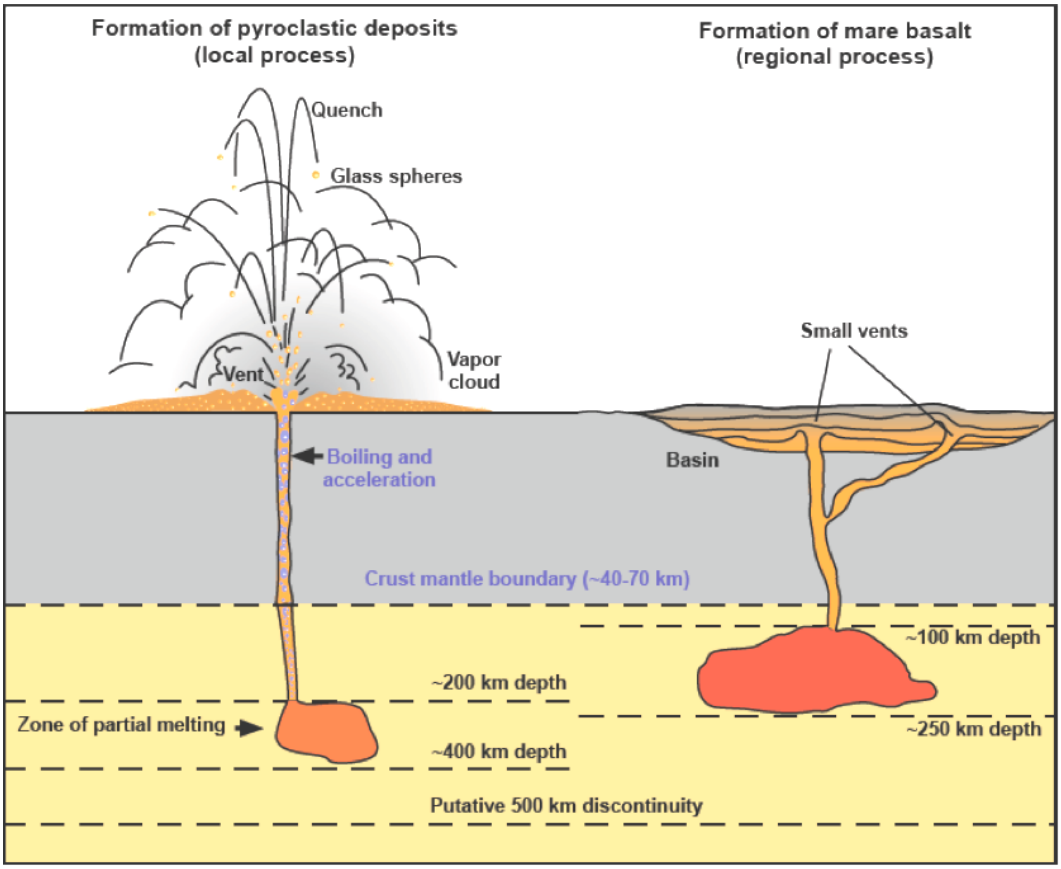

FIGURE 2.21 The image is not to scale. Schematic diagram (modified after Meyer *et al.*, 1975) illustrating the difference in source depths between the pyroclastic glasses (left) and the mare basalts (right), based on estimates of Delano (1986), Grove and Krawczynski (2009), Longhi (1992, 1995), Thacker *et al.* (2009), and Wieczorek *et al.* (2006) and references therein. Mare basalt volcanism is a regional scale process generally occurring in large basins (>300 km in diameter). The vents for pyroclastic eruptions are much smaller and represent local scale features; however, it should be recalled that the deposits from fire fountaining can cover up to 50,000 km^2 (Gaddis *et al.*, 1985).

Requirements

In situ Geophysics

Seismology

A passive network of three seismometers forming a triangle with 3000–5000 km spacing between stations is a minimum requirement to locate a deep moonquake event, provided that the signal reaches all three stations (Neal *et al.*, 2006). Smaller triangles with spacing comparable to the depth of the event (50–200 km) are necessary to locate shallow moonquakes in the upper mantle. Thus, the minimal requirements for geophysical landing site selection differ for the various aspects of Science Goal 2b.

1) To evaluate deep mantle structure and stratification, resolve its lateral heterogeneity, and assess the nature and extent of the putative 500 km discontinuity, a four-station array is the required minimum (Neal *et al.*, 2006).
2) To assess the global distribution of lunar seismic events, at least one station must be located on the farside.
3) To assess fine-scale vertical stratification of the mantle below 1100 km depth, a triangular array of three seismometers with 3000–5000 km spacing between stations is required.
4) An unrealistically large number of closely spaced (50–200 km) seismometers are required to characterize the *global* shallow moonquake distribution (Neal *et al.*, 2006). However, small

clusters of three seismometers in a triangular configuration could address shallow moonquake distribution and upper mantle structure where these configurations are placed. It would also perhaps allow discrimination between the proposed causes for HFT events (Frohlich and Nakamura, 2006).

The seismometers need to operate at a higher sensitivity than the Apollo seismometers and able to operate at three frequency bands: 0.001–0.1 Hz, 0.1–1.0 Hz, and 1.0–20 Hz. The network of seismometers must also be operating simultaneously for the entirety of the 6-year lunar tidal period (due to physical libration) to provide enough sampling of moonquake events. It should be noted that the longest lunar tidal period is ~18.6 years (Wieczorek, 2009) and its full effects on deep interior seismicity will not be captured with a 6-year operation time. Due to the configuration requirements of this seismic network, seismology is the main driver for geophysical landing site selection for addressing Science Goal 2b.

EM Sounding

Magnetotellurics provides knowledge of the radial electrical conductivity structure as well as lateral heterogeneity with resolution comparable to the skin depth. This can be used in complement to seismology to infer internal temperature and composition. EM sounding of the lunar mantle requires detection of signals 0.001–1 Hz (Grimm and Delory, 2010; Fillingim *et al.*, 2011). Since MT studies can be conducted independently rather than in a network, they do not have specific landing site requirements and can be deployed anywhere on the lunar surface. The benefit of deploying MT on the surface rather than in orbit is that it takes advantage of having amplified signals on the dayside surface (Fig. 2.22).

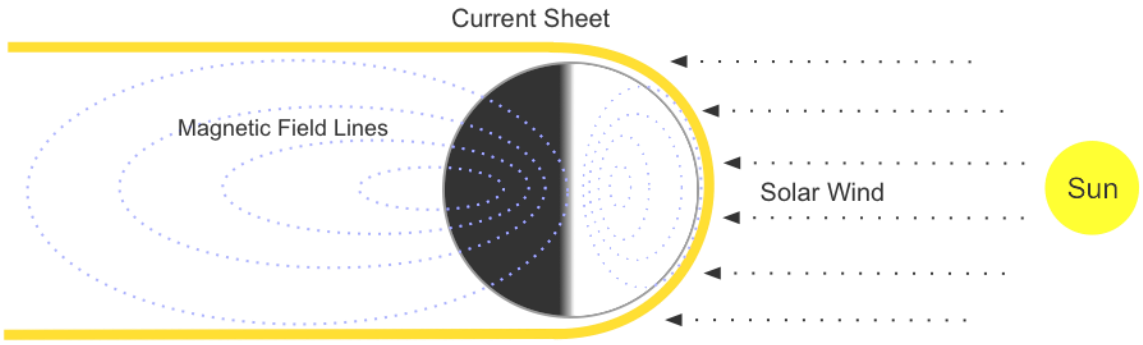

FIGURE 2.22 The effect of solar wind on the lunar magnetic field environment (modified after Grimm and Delory, *in press*). This is caused by solar wind bombardment of the magnetic field, which induces a current sheet (in yellow) that acts to compress and amplify the dayside surface field. Surface magnetometers will be able to measure these amplified signals, which will improve the EM sounding experiments.

Lunar Laser Ranging

LLR can provide measurements of bulk elasticity of the mantle, which constrain composition and seismic parameters. Thus, it provides data that can be used in conjunction with EM sounding and seismic data to jointly invert for interior structure. Since bulk elasticity of the mantle is only useful for seismic inversions, and given that the GRAIL mission can determine the tidal Love number, k_2, with an order of magnitude better accuracy than the current LLR network (Williams *et al.*, 2010), LLR will not be a driver for geophysical landing site selection for Science Goal 2b. However, retroreflectors should be deployed at any landing sites visible from Earth that are outside the coverage of the current LLR network.

Sample Return

Sample return is required in order to fully address the chemical and physical stratification of the mantle (NRC Report, 2007). The chemical composition of the lunar mantle is poorly understood due to a lack of direct samples of the mantle in the current sample collection. Our understanding of the mantle is limited to materials derived from the mantle such as volcanic products like mare basalts, and it has been suggested

that the lunar mantle is mineralogically similar to the Earth's, being mostly composed of orthopyroxene and olivine (reviewed by Wieczorek *et al.*, 2006).

Other Science Concepts have proposed to sample mantle-derived materials and potential mantle outcrops. However, the sample return landing sites proposed for this Science Goal are aimed at understanding the composition of the lunar mantle, as outlined below. It is anticipated that the direct sampling of exposed mantle or mantle-derived lithologies will aid the interpretation of geophysical measurements proposed for this Science Goal. Understanding the chemical evolution of the mantle will also help constrain thermal evolution models (*i.e.*, the lunar heat engine), and thus will also contribute to sample return considerations for Science Goal 2d.

We worked on the premise that there are two kinds of samples on the lunar surface that may elucidate the composition of the lunar mantle:

1. Mantle derived material (which may or may not have assimilated crust): pyroclastic deposits, mare basalts and cryptomare
2. Potentially exposed mantle material in craters and basins, including: ejecta material, melt sheet, and outcrops of central peaks and peak rings.

However, direct mantle exposures in craters and basins are based on calculations (described in Science Goal 2a) and thus are theoretical. However, it is generally agreed that basalts and picritic glasses originate in the mantle and therefore these mantle-derived materials are considered as 'primary' target sites, with craters and basins as 'secondary' targets.

In order to maximize the probability of successful sampling, selected landing sites should meet the following criteria:

1. Direct sampling of mantle derived lithologies
2. Direct sampling of exposed mantle
3. Outcrops and deposits of a specific basin should be known so that it is clear which crater or basin is being sampled
4. Outcrops or deposits should be exposed at the surface and easily accessible

Methodology

In situ Geophysics

As the only driver to address the geophysical methods within this Science Goal is a tetrahedral configuration of seismometers upon the lunar surface (Fig. 2.23), there is no GIS work to be completed for this Science Goal. The site selection for the third and fourth seismometers depends only on where the first and second seismometers are placed. Though the full nature of shallow moonquake events and upper mantle structure will not necessarily be determined by a globally-distributed tetrahedron, small clusters of three seismometers with 50–200 km spacing could be placed at the corners of the array to study fine-scale shallow mantle structure within the clusters. Although 12 seismometers would be optimal for global coverage of both deep and shallow mantle, the questions posed by Science Goal 2b can begin to be addressed primarily by a tetrahedral seismic configuration.

LLR is not a driver for this Science Goal, but the placement of an additional retroreflector would be beneficial on any nearside landing site outside the current LLR network. A discussion on appropriate landing sites can be found in Science Goal 2c, where it is a driver for geophysical landing site selection.

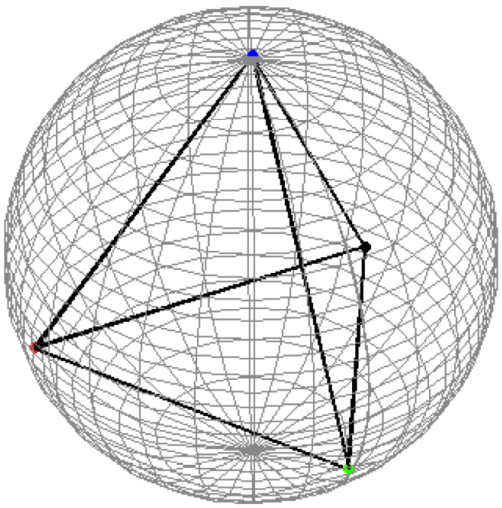

FIGURE 2.23 Tetrahedral configuration for a four-station seismic network, where the sphere represents the lunar surface. As long as the relative positions of the four stations are maintained, this configuration can be rotated to comply with other landing site requirements.

Sample Return

1. All primary mantle derived products on the lunar surface were mapped in ArcGIS:
    a. Pyroclastic deposits (see Table A2.2 based on the USGS Lunar Pyroclastic Volcanic project and Gustafson *et al.*, 2012, this table also gives the estimated size of deposits)
    b. Mare basalts as identified on LROC Quickmap
    c. Cryptomaria (compiled data in Table A2.3, based on detailed work done by, *e.g.*, Antonenko, 1999)

The mare basalt distribution was then optimized to obtain the most science for a given site:

Optimization 1: Sampling multiple mare basalt flows at one landing site

In order to identify potential landing sites from which the most science could be derived, the average model age of all mare basalts was calculated from Hiesinger *et al.* (2000, 2002, 2003, 2011, 2012), Morota *et al.* (2011), and Whitten and Head (2011). We then identified all of the locations on the lunar surface (both near and farside) where more than one mare basalt flow could be sampled. These locations were then ranked based on how many basalt flows could be sampled and the aggregated model age range at a given location. We took into account the fact that relatively young mare basalt samples are under-represented in the sample collection so these were given higher priority than relatively old mare basalt flows. Note that there is a 30 km buffer applied to each point as an estimated georeferencing error in ArcGIS.

Optimization 2: Composition of mare basalts.

In order to further obtain the most science from one landing site we used Clementine data (from Lucey *et al.*, 2000) to map the variation of titanium content across the lunar surface. This was used to determine the locations of underrepresented basalts (*i.e.*, intermediate to very low TiO_2) (*e.g.*, Hiesinger *et al.*, 1998; Wieczorek *et al.*, 2006).

1. Using the depth of excavation calculations summarized in Science Goal 2a, we identified all craters and basins that may theoretically expose mantle material in their ejecta (*i.e.* those with negative proximity to the crust-mantle boundary).
2. Using the melt depth proximity calculations, we determined where on the lunar surface the lunar mantle may be sampled in impact melt sheets or in the central peak/ring (*i.e.*, those with negative proximity to the crust-mantle boundary). (Table A2.4).

3. LROC Quickmap was then used to visually determine whether those craters and basins do actually preserve their central peaks or peak rings. For example, Imbrium basin was calculated to contain mantle material in its central peak/ring however, it is not visible in LROC images as it is masked by younger mare basalt flows, and thus the central uplift is not available for sampling.
4. The secondary target site data was then compared to the spectral profiler olivine detection data of Yamamoto *et al.* (2010, 2012), which may indicate presence of troctolite/dunite at the surface. (Table A2.5)
5. Finally, optimized primary target data was compared with secondary target site data, to select the landing sites providing the most scientific opportunity.

As described in Science Goal 2a, the formation mechanism of rings and peak rings is highly debated. Thus, craters or basins calculated to sample mantle material should be treated with caution. For example, Imbrium and Serenitatis basins are considered to have sampled mantle, but Apollo 15 and 17 astronauts did not obtain any samples of mantle material from them.

Suggested Landing Sites

In situ Geophysics

Due to the nature of requirements for geophysical methods, no specific landing sites are suggested, but any set of geophysical landing sites chosen to address Science Goal 2b should maintain a tetrahedral configuration (see Methodology, above).

Sample Return

Figure 2.24 shows everywhere on the lunar surface where primary target sites (mantle derived products) might be sampled. Note that the pyroclastic deposits are of various sizes (from <1 to >49,000 km^2).

Table A2.6 and Fig. A2.1 shows the results of Optimization 1. Optimization 2 then identified the locations of underrepresented basalts at Mare Frigoris, northern and eastern Oceanus Procellarum, northern Mare Imbrium, northern Mare Serenitatis, and SPA. Figure 2.25 shows the combination of Optimization 1 and Optimization 2 for mare basalts. Overlap with high priority Optimization 1 and Optimization 2 sites occurs in northern and eastern Oceanus Procellarum, Mare Frigoris, NW Imbrium, proximal to Aristarchus crater, and NW Mare Serenitatis.

Table A2.4 identifies all of those craters and basins that potentially sample mantle material in their central uplifts (peaks/rings). From the calculations there are only three basins that have potentially sampled mantle material in their ejecta blankets (South Pole-Aitken basin, Imbrium and Serenitatis). From consultation with LROC Quickmap, the basins which potentially expose mantle material in their preserved central uplifts are Apollo, Hertzsprung, Orientale, Nectaris, Moscoviense, Schrödinger, Amundsen-Ganswindt and Poincare.

Conclusions

Figure 2.26 shows the final suggested landing sites, deduced by comparing primary and secondary sample return target sites and identifying any overlaps. Since there are no specific geophysical locations (*c.f.,* Suggested Landing Sites) and only a configuration that must be maintained, any site chosen for sample return should also contain a seismometer and, if appropriate, an LLR station.

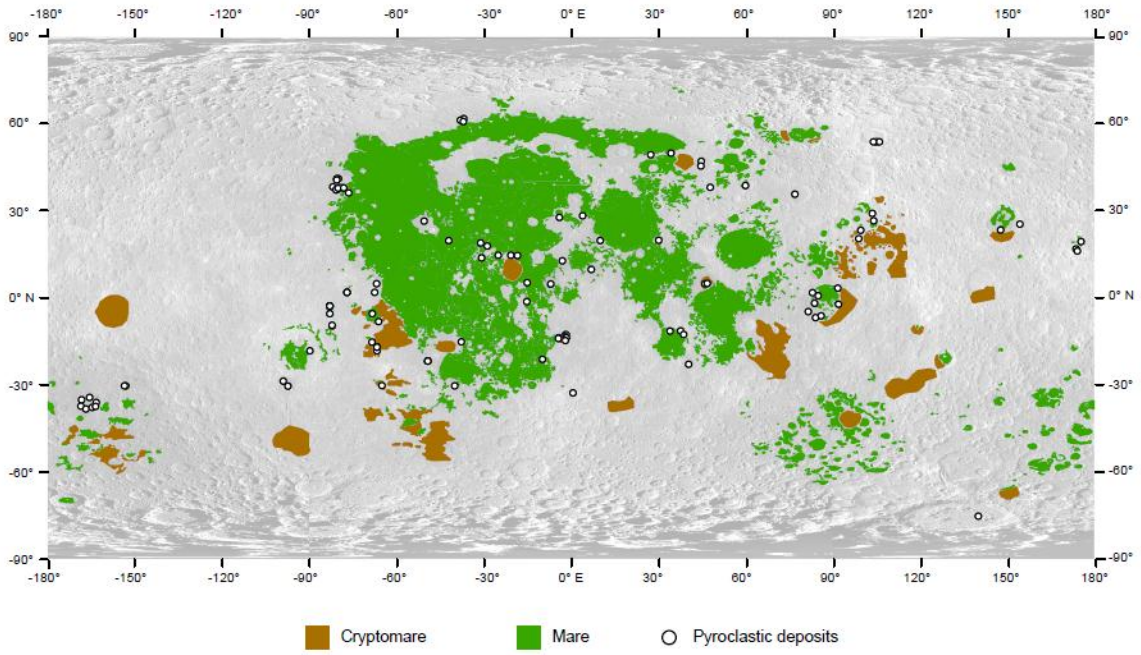

FIGURE 2.24 Map of all of the primary target sites for sample return (pyroclastic deposits, mare basalt flows, and cryptomare). The background is a WAC global mosaic.

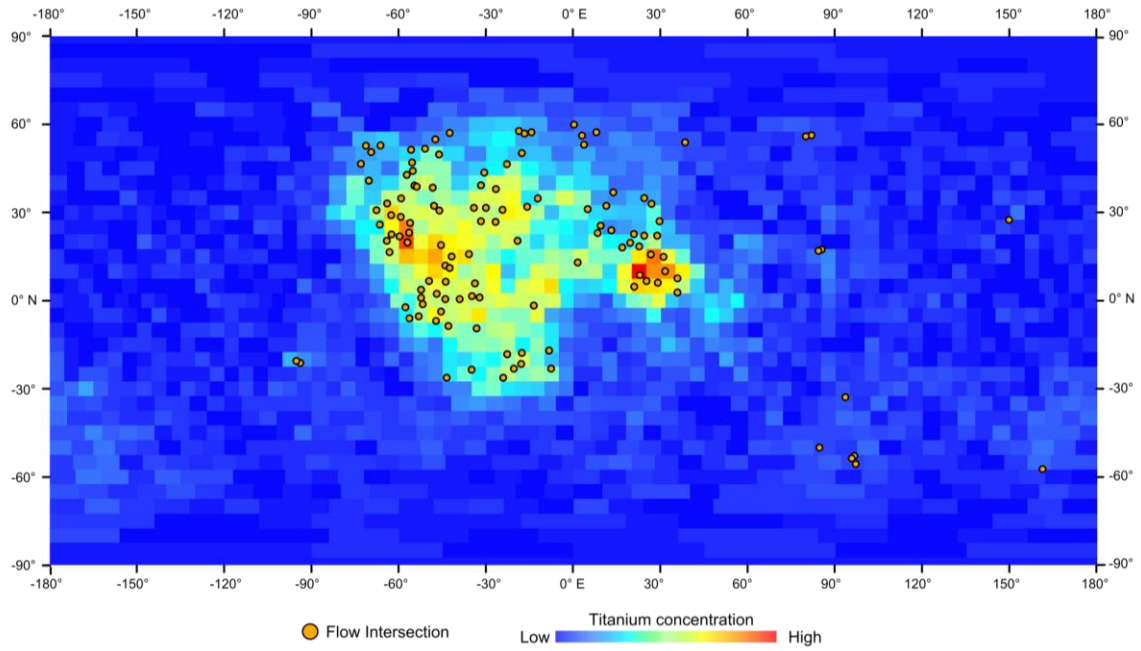

FIGURE 2.25 Shows the optimizations 1. The rank points represent the places where more than one basalt flow could be sampled, the rank numbers are listed in Table A2.4 identified by latitude and longitude. Optimization 2 is also shown, with optimization 1 basalts projected onto a Clementine Ti map (Lucey *et al.*, 2000). Colors represent the count rates, simply these correspond to higher counts corresponds to high Ti detected, low counts imply low Ti concentration detected.

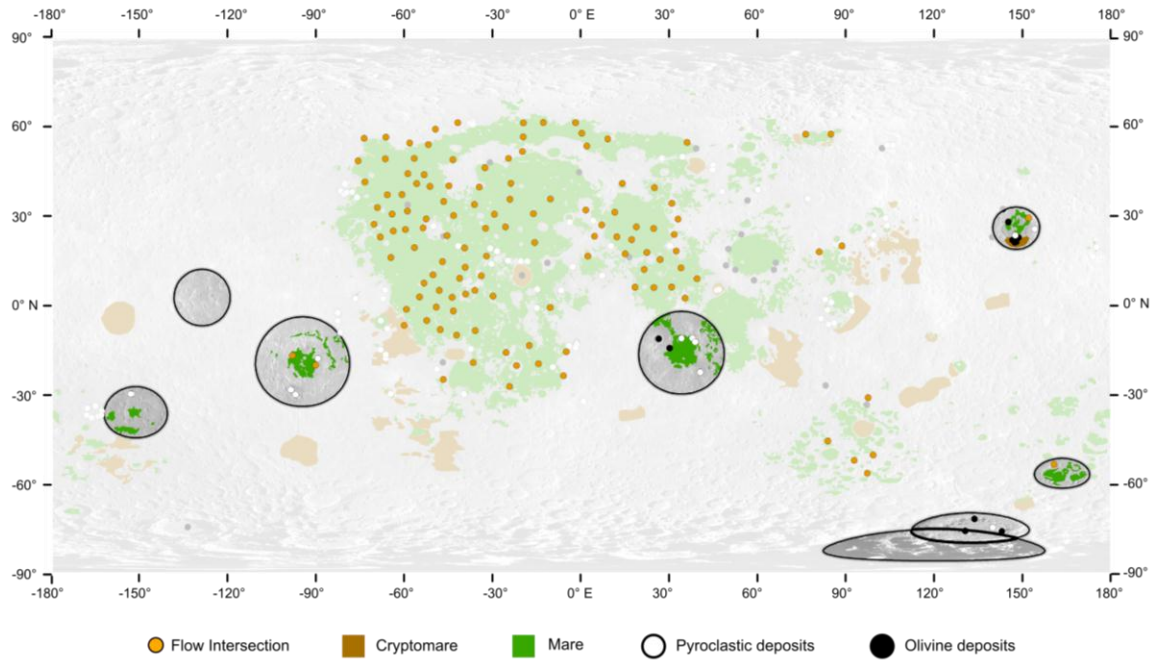

FIGURE 2.26 Shows the final landing site map for Science Goal 2b sample return. The highlighted craters and basins are those within which there is the most overlap between primary and secondary target lithologies. Background of WAC global mosaic.

SCIENCE GOAL 2C: DETERMINE THE SIZE, COMPOSITION, AND STATE (SOLID/LIQUID) OF THE CORE OF THE MOON

Introduction

Despite more than three decades of remote sensing analyses, relatively little is known about the current size, composition, and state of the lunar core. Besides generally verifying its existence, previous work suggests that (1) the core is between 1–3% of the mass of the Moon and thus has a relatively small radius (<500 km: *e.g.*, Williams *et al.*, 2001), (2) the core could be composed of pure Fe metal, Fe-FeS metal, or Ti-rich silicates (*e.g.*, Wieczorek and Zuber, 2002), and (3) the core is either partially or fully molten (*e.g.*, Williams *et al.*, 2001). Knowledge of the current characteristics of the core is an important consideration for planetary differentiation and thermal evolution, especially because it provides fundamental constraints on lunar formation hypotheses (Wieczorek *et al.*, 2006). Therefore, addressing this Science Goal will also provide information for Science Goal 2d.

Core size can be constrained through a variety of geophysical methods, including moment of inertia measurements, lunar laser ranging (LLR), electromagnetic (EM) sounding, heat flow measurements, and seismology. While each of these datasets independently provides particular information about the core, they should be used together in order to reduce the non-uniqueness of calculated core size (*e.g.* moment of inertia measures the distribution of mass, but it does not give detailed density structure and allows for multiple fits to a single data point).

The concentration of siderophile ('iron-loving') elements in the crust and mantle can also provide information on differentiation and core formation (*e.g.*, Righter, 2002). If the crust and mantle are relatively depleted in siderophile elements, then it is likely that the Moon underwent some level of core formation. However, while geochemical data are useful in determining the possible existence of a core, there is not one particular sample type that addresses its *current* size, composition and state. Therefore, landing sites for sample return are not addressed in this Science Goal.

Background

Size of the lunar core

A summary of published data on possible core sizes is shown in Table 2.3. Information on the size of the lunar core was obtained by Apollo-era seismic analyses (*e.g.*, Nakamura *et al.*, 1974; Sellers, 1992; Weber *et al.*, 2011), EM sounding from both lunar surface and low-orbit measurements (*e.g.*, Dyal *et al.*, 1976; Hood *et al.*, 1982; 1999), moment of inertia (Konopliv *et al.*, 1998), and LLR (*e.g.*, Williams *et al.*, 2001). Some authors have also used petrologic, thermal, and geophysical constraints to model potential core sizes (Binder, 1980; Mueller *et al.*, 1988; Kuskov *et al.*, 2002). In all, these analyses suggest the existence of a lunar core between 150 and 500 km in radius.

A few caveats are required to interpret these size ranges. First, many publications indicate that a core is permissible but not required to fit the available data (Dyal *et al.*, 1976; Goins *et al.*, 1981b; Hobbs *et al.*, 1983; Sellers, 1992; Konopliv *et al.*, 1998; Wieczorek and Zuber, 2002). As such, much of the early EM sounding and seismic work should be viewed as *maximum permissible* core sizes rather than *best estimates* of core size. Secondly, inferences about core size are highly dependent on the modeled core composition, such that pure Fe-metal core sizes are smaller than Fe-FeS metal cores, which are in turn smaller than Ti-rich silicate cores (Wieczorek and Zuber, 2002). This is especially true for EM sounding data because of the conductivity differences between potential metal and silicate compositions; larger cores with lower conductivity (*i.e.*, Ti-rich basalts) can fit the data as well as smaller cores with higher conductivity (*i.e.*, pure Fe or Fe-rich metal). Higher-resolution geophysical data have the potential to reduce the non-uniqueness of these solutions.

Composition of the lunar core

Existing data on the composition of the lunar core suggest two possible end-members: metallic (pure Fe, FeS, Fe-FeS eutectic, or Fe-FeS-C alloy: Wieczorek *et al.*, 2006) or dense Ti-rich silicate (Hess and Parmentier, 1995; Wieczorek and Zuber, 2002). Most of the geophysical data are non-unique with respect to core composition, and either metal or silicate cores are possible (Wieczorek and Zuber, 2002; Kuskov *et al.*, 2002; Wieczorek *et al.*, 2006). However, certain datasets either require or exclude one of the possible end-members. Paleomagnetic data from returned Apollo samples strongly suggest the presence of a metallic core (*e.g.*, Cisowski, 1983; Shea *et al.*, 2012), and this contention is supported by geochemical modelling (Buck and Toksöz, 1980) and highly-siderophile element depletion in the lunar mantle (Righter, 2002). Hafnium-tungsten (Hf-W) systematics also indicate a metallic core, but by a different formation process than the other terrestrial planets (*i.e.*, giant impact as opposed to accretion) (Kleine *et al.*, 2002). If the Moon does contain a metallic core, it is unlikely to be pure Fe, but rather a Fe-FeS eutectic composition (Stevenson and Yoder, 1981; Khan and Mosegaard, 2001; Weber *et al.*, 2011). It is also likely that Fe would entrain C to the core during core formation as has been postulated for Earth (Hirayama *et al.*, 1993; Wieczorek *et al.*, 2006).

Alternatively, models of global cumulate overturn suggest that ilmenite-rich material sank toward the center of the Moon early in lunar history (*c.f.*, Science Goal 2b), either blanketing an existing metallic core or creating a dense silicate core (Hess and Parmentier, 1995; Wieczorek and Zuber, 2002; de Vries *et al.*, 2010). There is evidence that a silicate core could theoretically be a strong enough conductor to produce a lunar dynamo (Wieczorek *et al.*, 2006), but there is some debate as to whether or not it could remain molten until the present, as required by the LLR data (Hood *et al.*, 1999; Wieczorek and Zuber, 2002). Certain geophysical models are also best fit by a dense silicate core (Khan and Mosegaard, 2001).

Previous work has shown either of the two compositional end-members to be viable possibilities, with more data required to discriminate between them.

TABLE 2.3 Literature compilation of minimum and maximum core radii (or a single value if only one given), the method used to obtain core size, the assumed or modeled core composition (which is key to determining core radius), and the reference from which the estimate was obtained.

Minimum Radius (km)	Maximum Radius (km)	Method	Assumed or Modeled Core Composition	Reference
170	360	Seismic	--	Nakamura *et al.* (1974)
--	500	Seismic	--	Nakamura (*pers. comm.*) cited in Goldstein *et al.* (1976)
320	580	EM Sounding	--	Goldstein *et al.* (1976)
0	400	EM Sounding	metallic	Wiskerchen and Scott (1977)
0	535	EM Sounding	--	Dyal *et al.* (1976)
200	400	Petrologic/Thermal Modeling	Fe- or Fe-rich composition	Binder (1980)
435±15		EM Sounding	--	Russell *et al.* (1981)
0	360	EM Sounding	metallic	Hood *et al.* (1982)
0	435	EM Sounding	metallic	Hobbs *et al.* (1983)
150	--	Petrologic/Geophysical Constraints	metallic	Mueller *et al*. (1988)
400	450	Seismic	--	Sellers (1992)
220	450	Moment of Inertia	--	Konopliv *et al.* (1998)
340±90		LP EM Sounding	metallic	Hood *et al.* (1999)
352	374	LLR	radius depends on composition (Fe or FeS)	Williams *et al.* (2001)
313	413	LLR	pure liquid Fe (min) to Ti-rich basalt (max)	Wieczorek and Zuber (2002); data from Williams *et al.* (2001)
350	530	Petrologic/Thermal Modeling	radius depends on composition; more S = larger radius	Kuskov *et al.* (2002)
~350		LLR; LP EM Sounding	--	Khan *et al.* (2004)
--	375	Literature Compilation	Fe-FeS-C alloy; could be larger if silicate	Wieczorek *et al*. (2006)
330±20 (total), 240±10 (solid inner core)		Seismic	metallic	Weber *et al.* (2011)

State of the lunar core

LLR, Lunar Prospector, and Apollo-era seismic data all indicate that the core is at least partially molten (Williams *et al.*, 2001; Khan *et al.*, 2004; Weber *et al.*, 2011). The extent of melting is unclear; a fully molten core or a fluid shell around a solid inner core are both possible to explain the inferred torque between mantle and core (Williams *et al.*, 2001) though recent seismic inversions suggest the latter case (Weber *et al.*, 2011). Regardless of its current state, the presence of a lunar dynamo would require a liquid core at some point in early lunar history (*e.g.*, Shea *et al.*, 2012). Therefore, higher-resolution data on the current state of the core is crucial to interpreting models of lunar thermal evolution.

Requirements

Seismology

A minimum of two seismometers is required to study the size and state of the core (ILN Final Report, 2009). However, since three stations are required to locate a seismic event (Neal, 2006), a two-station array must be strategically placed to take advantage of deep moonquake nests (Fig. 2.21) with known locations and seismic signatures (Nakamura, 2005). One station must be placed within 60° of the deep moonquake epicenter to accurately obtain its origin time (Cohen *et al.*, 2009). The other station must be

placed near the antipode of the seismic source to record waves that have travelled through the deep interior, which we define as being within 120 km of the geometric center of the Moon (Fig. 2.27). One DMQ nest, termed A33, has the advantage of being located on the farside with a nearside antipodal point (Goins *et al.*, 1981b). The majority of other nests, however, would require a station on the farside.

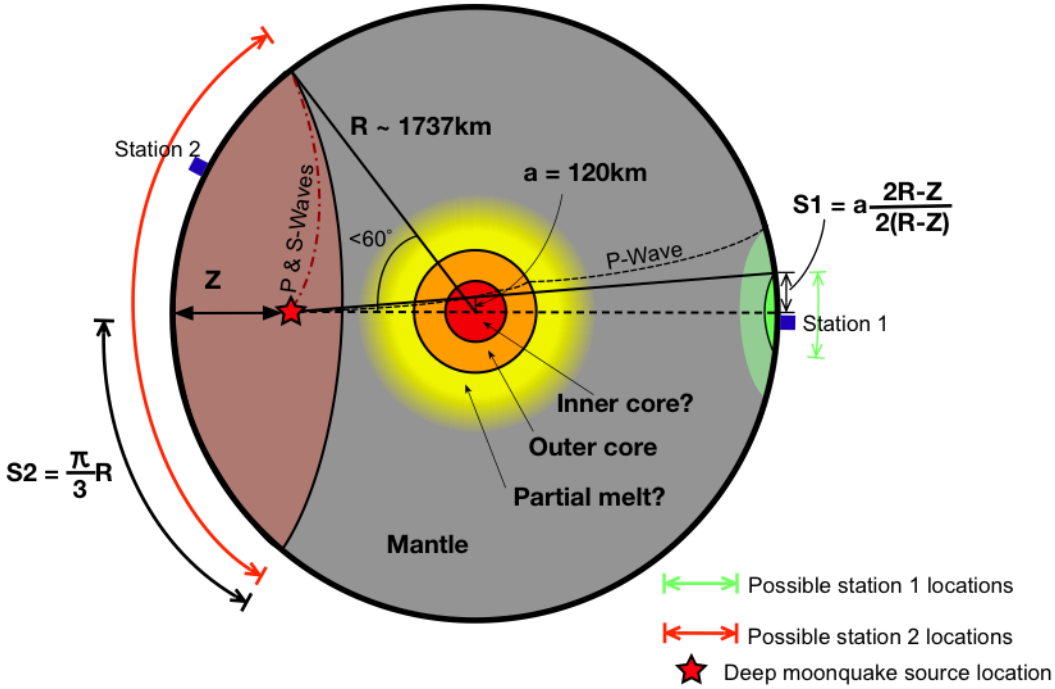

FIGURE 2.27 Geometry of the two-station set-up (discussed in text) that will elucidate the size and physical state of the lunar core. Here, the Moon is approximated to be a sphere with radius R. Z is the depth of the deep moonquake source. Station 1 would be placed within a distance S_1 from the antipode, and station 2 will be placed within a distance S_2 from the epicenter. *a* is conservatively taken to be half of the most recent estimates for an inner core radius of 240 km (Weber *et al.*, 2011).

Lunar Laser Ranging (LLR)

Additional stations to the current LLR retroreflector network will provide the deformation properties, geometries, and depths of major compositional and phase change interfaces (*i.e.* mantle-outer core, outer core-inner core) of the lunar interior (Williams *et al.*, 2010). These improvements require an increase in the three-dimensional coverage of the retroreflector network to more accurately record the three-axis physical lunar libration. The LLR arrays are also required to be on the nearside, and positioned within regions constantly visible from Earth during the full libration period. Geophysical landing site selection (LSS) will be partially driven by those visible locations that would make the most improvement to the current retroreflector network.

Heat Flow

Heat flow measurements can provide constraints on the size and thermal state of the core. Although it is not the main driver for geophysical landing site selection to address Science Goal 2c, it is still important to consider if a location is suitable for making heat flow measurements. For specific requirements of global heat flow studies, see Science Goal 2d where it is a main driver for geophysical landing site selection.

EM Sounding

EM sounding can provide constraints on the size, composition and thermal state of the core. This can be done with the Magnetotellurics (MT) method at a single site with no restrictions on its location. Thus, it

should accompany seismic and LLR experiments, without being a driver for any geophysical landing site selection.

Methodology

Seismology

To address where to place seismometers for Science Goal 2c, the locations of deep moonquakes were used to find the antipodal area with a radius S_1 required to receive seismic waves passing through an inner core of radius 120 km. A second station needs to be placed within 60° (or a distance S_2) of the epicenter of the deep moonquake nests. The values for S_1 and S_2 are calculated using the following equations as shown in Fig. 2.29:

$$\mathbf{S_1} = a\frac{\mathbf{2}R - Z}{\mathbf{2}(R - Z)} \qquad \mathbf{S_2} = \frac{\pi}{\mathbf{3}}R \tag{2.14}$$

Here, *a* is the defined radius for the inner core (taken to be ~120 km), *Z* is the depth of the moonquake event and R is the radius of the Moon (~1737 km).

LLR

Locating where LLR stations can be placed requires identifying those areas that are constantly visible from the Earth's surface. This must take into account regions permanently shadowed by topography and the libration of the Moon, which causes locations near the limbs to be obscured during part of the six year lunar physical libration period (Williams *et al.*, 2001). The effects of this libration have been approximated, so that here it is assumed that the lunar surface between -82.5 and +82.5°E, and -82.5 to +82.5°N is always visible to the Earth (Cohen *et al.*, 2009). This is a 'safe' estimate of this effect and ensures that the site chosen is never over the limb. To locate areas that are shadowed by topography when viewed from Earth, the LOLA 128 pixels per degree (ppd) digital elevation model (DEM) was used. The Earth was then modeled as a point source to find areas visible from a point placed at 0°E, 0°N and at a distance equal to that of the Earth to the Moon (356,700 km). This study should be repeated more thoroughly and make use of the WAC-LOLA-100m resolution DEM.

The current network spans only 25% of lunar diameter in the z-direction (mean rotational axis), 18% in the x-direction (axis pointing towards the Earth), and 38% in the y-direction (axis perpendicular to x and z). Increasing the spread in the z and y direction (Δz, Δy) improves the measurements of latitudinal and longitudinal libration responses, respectively (Merkowitz *et al.*, 2007). Increasing the spread in the x direction (Δx) would help separate the tidal and librational contributions to observed displacements. To treat the span improvements in all directions equally, the total coverage (L) of the retroreflector network is defined by the Pythagorean sum of the spans in each direction:

$$\mathbf{L} = \sqrt{\mathbf{\Delta}x^2 + \Delta y^2 + \mathbf{\Delta}z^2} \tag{2.15}$$

Using this definition, the total coverage achieved by adding a new station was calculated at all locations across the surface of the nearside of the Moon, normalized by the total coverage of the current network (L_0). Consequently, L_0 was calculated by taking the Pythagorean sum of the current LLR spans.

EM Sounding

As there are no requirements that must be satisfied for the location of an EM instrument, there are no methods to be outlined. Since location requirements for EM sounding are trivial, we suggest combining it with other geophysical instrumentation to optimize data returned from a minimum number of locations (see below).

Combining LLR with Seismic

An advantage of using the A33 nest as a seismic source is that the antipode lies on the nearside close to the western limb. In addition, there is an area within 60° of the nest which extends to the nearside. This allows for LLR and seismology experiments of this Science Goal to be addressed in close proximity to one another, and thus share the same landing sites.

Combining LLR, Seismic, and Heat Flow

Once requirements for the driver of geophysical landing site selection are met, extra requirements can be placed to see if there are locations that satisfy the requirements for LLR, seismic and heat flow instruments simultaneously. The requirements and methods for mapping landing sites suitable for heat flow measurements are discussed in detail in Science Goal 2d, where it is a primary driver for geophysical landing site selection.

Suggested Landing Sites

Seismology

Using information on current moonquake nests and Equation 2.14, circles can be plotted showing potential seismic station placement (Fig. 2.28). The A33 moonquake nest was used as an example, as it has station pairs that can be located on the nearside, meaning sites can be combined with LLR sites.

LLR

Landing sites for placing LLR stations must avoid areas never or not always visible from the Earth's surface due to apparent lunar libration. These sites are plotted in Fig. 2.29.

Figure 2.30 shows the comparative improvement in the current LLR retroreflector network coverage that can be achieved by placing an additional retroreflector at a specific location, taking into account the x, y, and z span of the network. The map shows that placing LLR stations at the limbs and closer to the South Pole than the current stations significantly improves the LLR network coverage. The dark blue area in the center of the map shows the area for which placement of an additional retroreflector would not improve the current LLR coverage; red shows areas which would best improve the current LLR network.

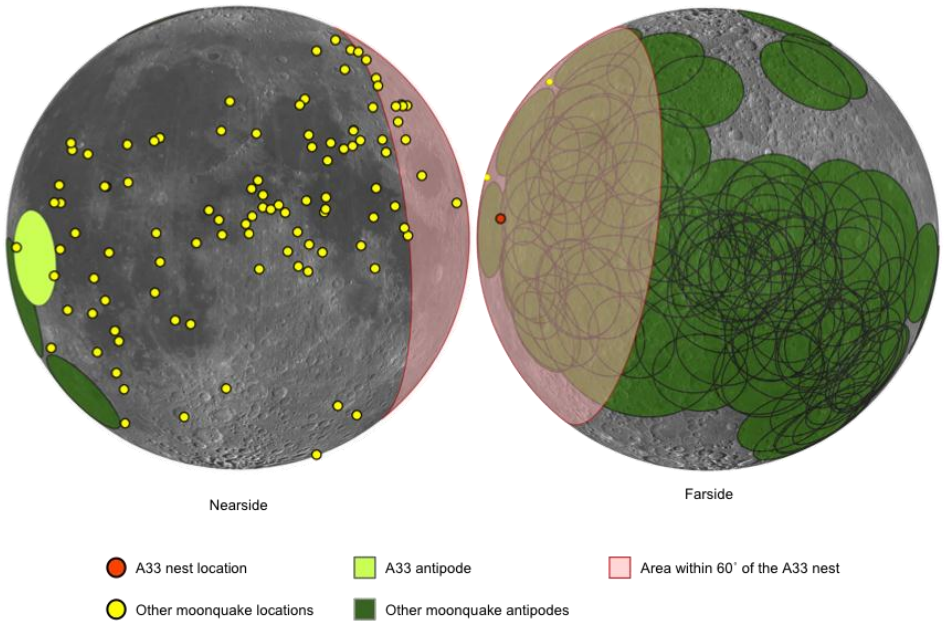

FIGURE 2.28 Location of known moonquake nests and the areas within which seismometers can be placed to gather information regarding the core. The A33 nest and antipode are highlighted as this nest offers the opportunity to combine LLR and seismology experiments within the same landing site, as discussed in the text. Circles are projected onto the IAU Moon 2000 sphere.

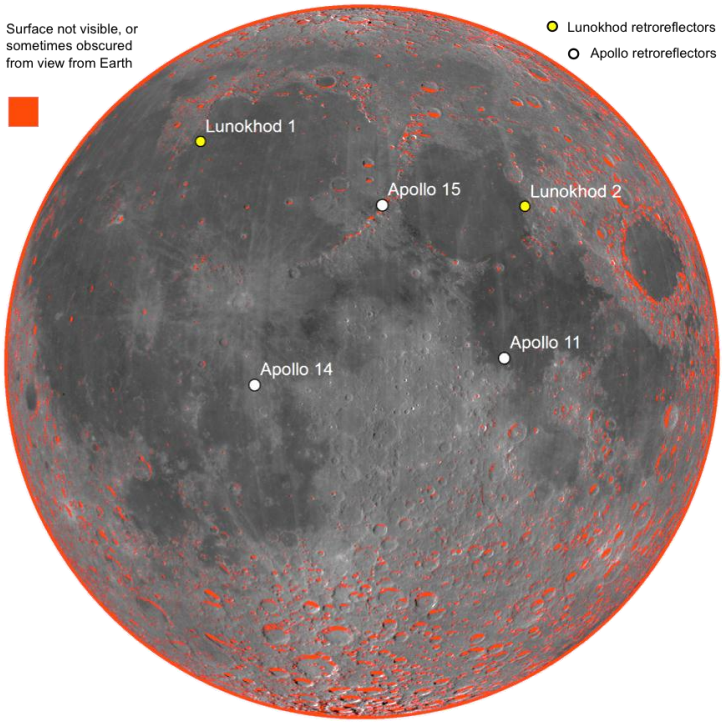

FIGURE 2.29 Map showing areas that are never or not always visible from Earth (red). LLR stations can be placed in any non-red location (nearside only). Current LLR retroreflector stations are shown. The background is the WAC Global Mosaic.

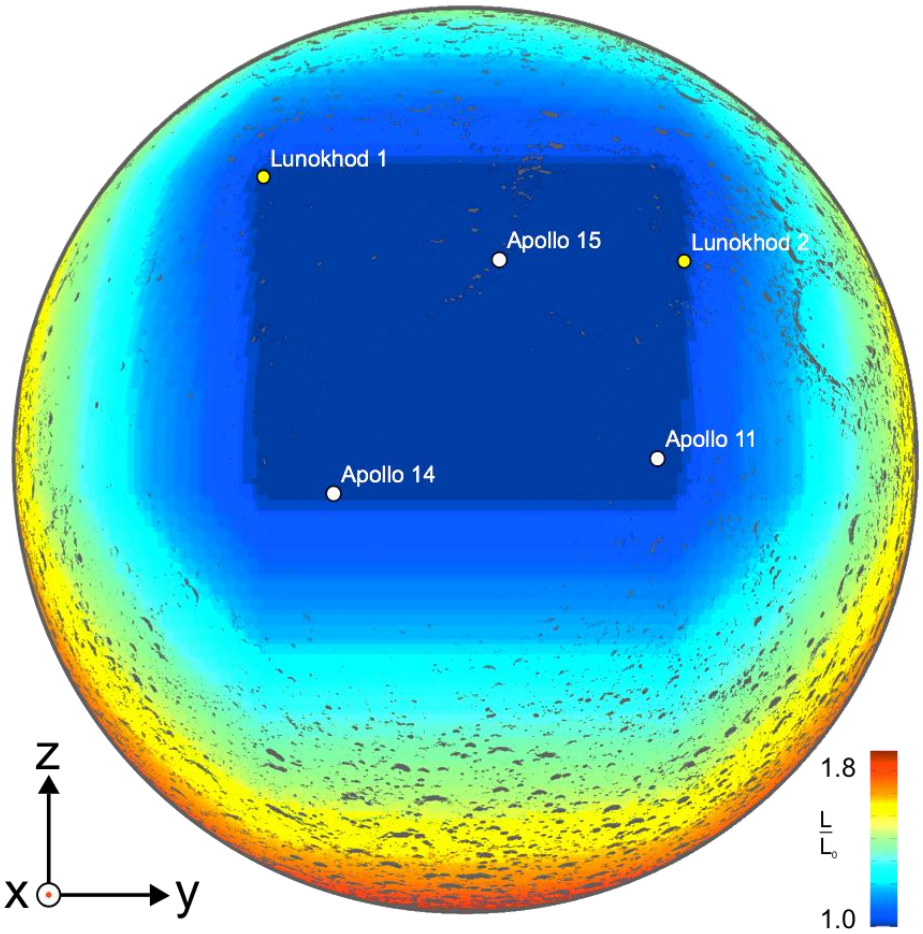

FIGURE 2.30 Map showing how placing a retroreflector at a specific location can improve the x, y, and z coverage of the current LLR network. Axes are shown on the bottom-left, with x pointing out of the page. Dark grey represents the areas which do not have a direct line of sight with Earth at all times during the 6 year lunar physical libration period. Blue regions represent minimal to no improvement relative to the current network configuration, while yellow to red regions are the best locations for an additional retroreflector.

Combining LLR with Seismic

LLR and seismic requirements are the primary drivers for Science Goal 2c landing site selection; Figs. 2.28 and 2.30 show all the locations where these geophysical analyses can be placed on the lunar surface. They have been combined in the final geophysical and overall maps for Science Concept 2, which also consider the tetrahedral requirement for a global seismic network. For the purposes of Science Goal 2c, any seismic station placed on the nearside should include an LLR retroreflector, but the choice of the deep moonquake nest used to probe the core (Fig. 2.28) will determine where that station should be placed. A specific example is shown in the A33 Case Study.

Combining LLR, Seismic, and Heat Flow

By combining heat flow with other geophysical experiments, much of the surface becomes ruled out of the landing site selection process. However, there are still potential landing sites remaining within the A33 nest and its antipode (Fig. 2.28), and the addition of two LLR stations would represent a significant increase in the current extent of the network. Figure 2.31 shows the same information as Fig. 2.28 but displays all the known deep moonquake nests. This shows that only three farside moonquake nests are suitable for the combined package of heat flow, LLR, and seismic experiments, assuming that only two

packages containing all three experiments are used. However, there are plenty of available sites should a nearside moonquake nest with a farside antipode be chosen. Any of these antipodes would be suitable for the study of the lunar core, providing that the second seismometer is placed within 60° of the moonquake nest. Some of these moonquake nests are well constrained using the currently available data, whilst some are not; refer to Nakamura (2005) for the location errors for each moonquake nest.

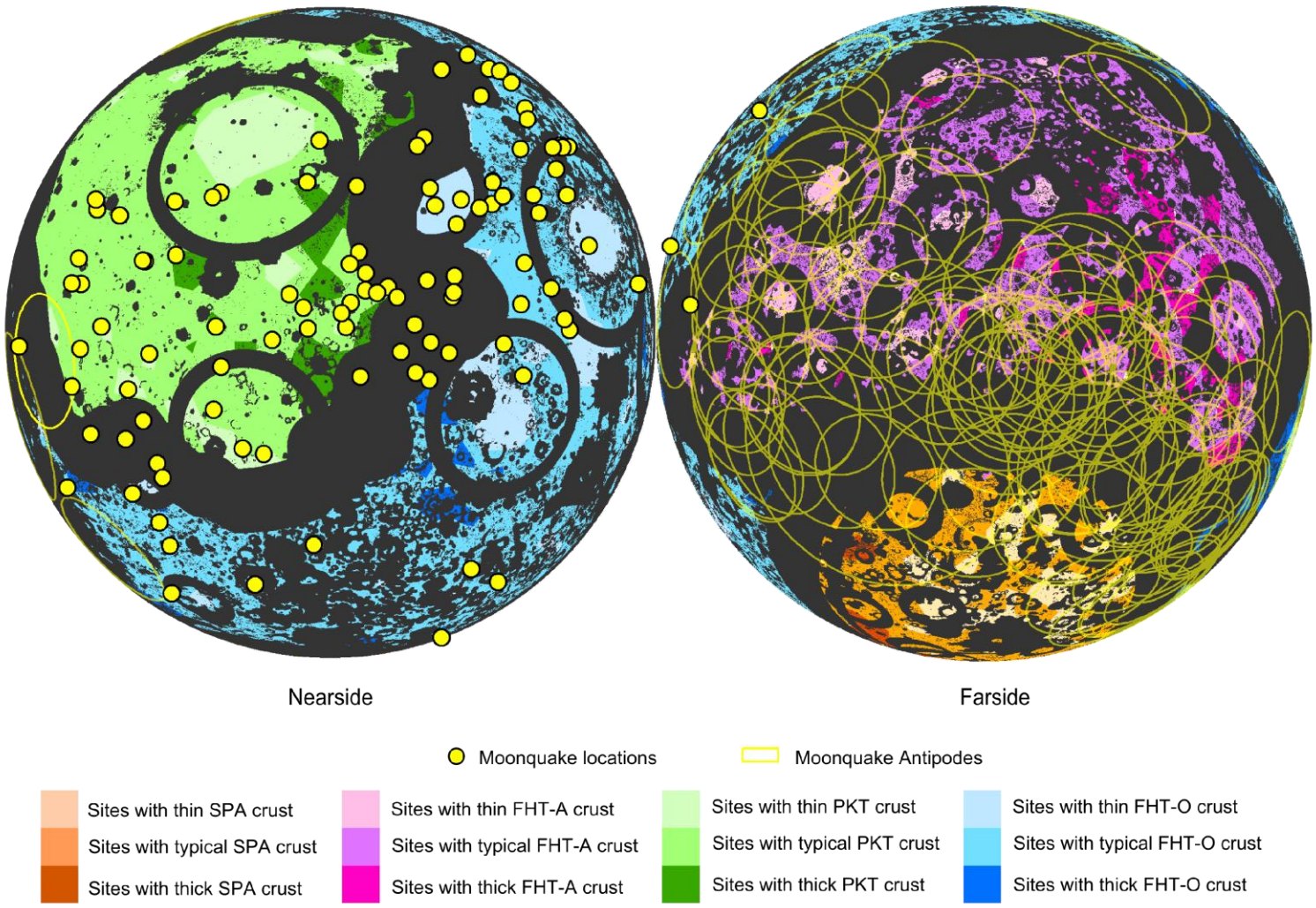

FIGURE 2.31 Map showing the same data as Fig. 2.30 applied to all known moonquake nests. This is to highlight that the A33 moonquake nest is not the only deep moonquake nest that could be used, but that it is one of the few known moonquakes that regularly occur on the farside.

SCIENCE GOAL 2D: CHARACTERIZE THE THERMAL STATE OF THE INTERIOR AND ELUCIDATE THE WORKINGS OF THE PLANETARY HEAT ENGINE

Introduction

Many geological and geochemical processes are driven by the removal of heat from the interior. Heat sources include energy accumulated during initial accretion and subsequent impacts, radioactive decay, tidal forcing, insolation, and bond energy release from chemical or phase changes. These energy sources either directly generate heat (*i.e.*, impact heating, latent heat, exothermic chemical processes, radioactivity) or produce material transport (*i.e.*, thermal/chemical convection, mechanical stirring from giant impacts, tidal deformation) that leads to viscous heat dissipation from internal friction or ohmic heat dissipation of currents generated during the dynamo process. A variety of factors such as energy budget, size and geometry of internal boundaries (*i.e.*, core mantle boundary (CMB) oblateness, crustal asymmetry), chemistry, composition, distribution of radiogenic elements, and orbital evolution can affect the thermal evolution of a planetary body.

The ways in which a planetary body removes heat dictate the physical and chemical evolution of its interior and its current state. Thus we need not only to study its present structure and composition, but also to understand the evolution of the planetary heat engine. The intimate link between thermodynamics and geology means that studies of thermal history require concurrent analyses of all aspects of lunar science affected by thermal processing.

Samples returned for Science Concept 1 will gauge the early impact flux of the Moon and provide insight into heat provided to the interior. Science Goal 2b, Science Concept 3 (Science Goals 3a and 3b), and Science Concept 5 (Science Goals 5a, 5b, and 5d) have proposed to sample various mare basalt flows within and outside the PKT. Data obtained from those samples will address the early cooling history of the Moon, in particular the evolution of basalt — and therefore upper mantle — chemistry and the distribution of KREEP through time. Thus, sample return for Science Concept 1, Science Goal 2b, Science Concept 3, and Science Concept 5 will also contribute to Science Goal 2d. In addition, geophysical data obtained for Science Goal 2a, 2b, and 2c will contribute greatly to our understanding of Science Goal 2d.

Background

It is hypothesized that the lunar magma ocean (LMO) occurred shortly after the giant impact that formed the Moon (Shearer *et al.*, 2006; *c.f.*, General Background). The depth of this LMO constrains the initial conditions of the lunar interior and its subsequent thermal evolution. This evolution is also affected by the primary anorthositic crust formed in the LMO, which acts as an insulating thermal boundary layer (Ziethe *et al.*, 2009). The core formation process advected heat out of the interior through material transport, likely producing an adiabatic temperature profile (Konrad and Spohn, 1997). The convection of a possible fluid metallic core early in lunar history and the generation of a core dynamo (Stevenson, 1983; Stegman *et al.*, 2003) put constraints on the rate at which heat was produced and removed from the core. Paleomagnetic data suggest a relatively strong dynamo had been active and peaked between 4.0–3.8 Ga (Fuller, 1974; Collinson *et al.*, 1977; Cisowski, 1983; Garrick-Bethell *et al.*, 2009; Shea *et al.*, 2012). The strength and persistence of the recorded magnetic field is difficult to explain with current thermal evolution models due to the lack of adequate energy during late accretion, although the energy budget of the core may have been expanded by later modification (LeBars *et al.*, 2011; Dwyer *et al.*, 2011). The subsequent magmatic evolution until 1.2 Ga (Hiesinger *et al.*, 2003) was characterized by the emergence of basaltic lava, which flooded large impact basins. Younger eruptions are difficult to explain with current models from an energy perspective because of the small size of the Moon and its inevitably rapid cooling; however, insulation by the crust and megaregolith combined with added heat energy could have curbed its secular cooling (Ziethe *et al.*, 2009). Factors such as meteorite impact flux, orbital evolution of tidal forcing, distribution of heat-producing elements, and crustal thickness variations affect this evolution to the current thermal state.

Present thermal state

Current global heat flux measurements are essential to assess the past and present thermal state of the Moon by providing both spatial and temporal boundary conditions for thermal models. Previous measurements of heat flow were taken during Apollo 15 and 17 (Langseth *et al.*, 1976) and yielded values of 21 and 14 mW/m^2, respectively. Unfortunately, both experiments suffered from a number of possible

interferences and were placed along terrane boundaries, making their representation of the lunar global heat flux questionable (*e.g.*, Conel and Morton, 1975; Warren and Rasmussen, 1987; Kiefer, 2012). The baseline measurement of any study of the planetary heat engine is an assessment of the current global heat flow. Thus, it is absolutely essential to obtain new heat flow measurements in each terrane and avoid locations where heat flow would be anomalous (*c.f.*, Requirements-Geophysical).

Once boundary conditions are obtained (*i.e.*, the heat flow distribution at the surface), the extension of the lunar thermal gradient requires knowledge of density and compositional stratification, since temperature, pressure, density and composition must be inverted for simultaneously (Dziewonski and Anderson, 1981). The thermal boundary layer (a layer in which the thermal state changes rapidly in order to match the boundary condition imposed by the surface) can be well approximated by a conductive temperature profile ($T_{cond}(z)$), and can be calculated by integrating the steady-state heat equation (Turcotte and Schubert, 2002, p. 250):

$$\frac{d^2T_{cond}}{dz^2} = -\frac{\rho H}{k} \qquad (2.16)$$

with outer boundary conditions (*i.e.* $\frac{dT}{dz}$ and T at z = 0) determined by the heat flow experiments. Values of thermal conductivity (k), density (ρ), and radiogenic heat production rate (H) vary with depth (z). These variables need to be determined using EM sounding, seismology and geochemical studies. The controlling factor for the geotherm at a particular location is H, since it can vary by many orders of magnitude depending on the quantity of various radioactive elements (Table 2.4) in the crust. Large lateral variations of H are expected due to a concentration of radioactive elements in the Procellarum KREEP Terrane (PKT) (Jolliff *et al.*, 2000). The depth extent of this conductive profile will also vary laterally because of variations in crustal thickness (Wieczorek *et al.*, 2006). Thus, conductive geotherms will vary globally and must be studied at multiple locations to determine the global thermal profile.

TABLE 2.4 Heat production rate and half-life ($\tau_{½}$) of various isotopes of elements relevant for the Moon. The actual radiogenic heat production rate in a volume will depend on the total concentration of each element (data from Turcotte and Schubert, 2002).

Isotope	H (W/kg)	$\tau_{1/2}$ (yr)
^{238}U	9.46×10^{-5}	4.47×10^{9}
^{235}U	5.69×10^{-4}	7.04×10^{8}
^{232}Th	2.64×10^{-5}	1.40×10^{10}
^{40}K	2.92×10^{-5}	1.25×10^{9}

Near the bottom of the thermal boundary layer (*i.e.*, the upper mantle), the temperature profile becomes approximately adiabatic (Konrad and Spohn, 1997). This adiabatic temperature profile ($T_{adia}(z)$) can be obtained through the joint integration of variables (*e.g.*, density and composition) using Equation 2.17 (Turcotte and Schubert, 2002, p. 340):

$$\frac{dT_{adia}}{dz} = \frac{T\alpha_V g}{C_p} \qquad (2.17)$$

C_p is the specific heat capacity at constant pressure and α_V is the volumetric thermal expansion coefficient of the material (both of which depend on the pressure, temperature and chemical composition) and g is the gravitational acceleration at that depth, which depends on the radial density profile. A global passive seismic network along with EM sounding can be employed (*c.f.*, Science Goal 2b) to determine the density and compositional stratification of the mantle and its lateral heterogeneity.

Any discontinuity in density or composition within the adiabatic profile can complicate thermal models by creating boundary layers that stall advective heat transport (Turcotte and Schubert, 2002). This can lead to major differences in geotherms by assuming that a conductive layer within the adiabatic region acts to insulate the interior (Fig. 2.32).

The size and state of the core controls the inner boundary conditions for the temperature profile (*i.e.*, heat flux and temperature at the CMB, its lateral variations, and the geometry of the CMB). The existence of an inner core along with solidus temperatures of probable lower mantle chemical compositions can also provide thermodynamic constraints. These constraints can elucidate the existence and thickness of an inner thermal boundary layer that also adopts a conductive profile. To probe these properties, a combination of seismology, LLR and EM sounding must be used (*c.f.*, Science Goal 2c).

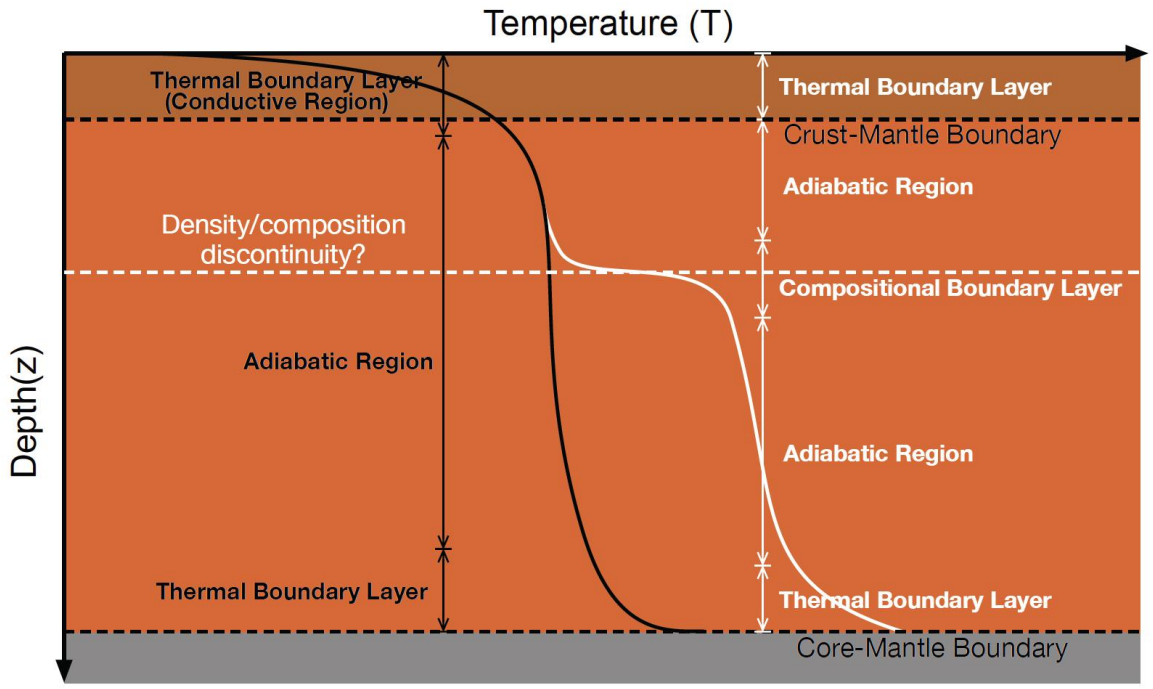

Figure 2.32 Possible one-dimensional temperature profiles for a planetary interior. Boundary conditions for T, dT/dz at the surface and CMB constrain the minimum and maximum temperature of the profile, and a compositional/density discontinuity changes the overall shape.

Thermal history

Three important heat sources are considered when modeling lunar thermal evolution: energy from accretion, energy from impacts, and long-lived radioactive isotopes (Wieczorek *et al.*, 2006). Energy from accretion affects the primary thermal state of the whole Moon during formation and governs how much initial melting occurs (Melosh, 1990). Energy from impacts has important consequences for the outer layers of the Moon and may have some influence on the location of volcanic provinces (Cintala and Grieve, 1998; Elkins-Tanton *et al.*, 2004). Long-lived radioactive isotopes affect the entire Moon and are a major driver for volcanism (Wieczorek and Phillips, 2000). A number of models have been created to address the early thermal state of the Moon, ranging from purely conductive to purely convective with some level of melting and/or melt migration (for more details regarding these models, the reader is directed to Tables 4.10 and 4.11 of Shearer *et al.* (2006)). However, a lack of new data on these issues has led to a stagnation in thermal model development.

Data from the Apollo missions had a profound impact on our understanding of the thermal evolution of the Moon. The favored hypothesis for lunar origin is through the accretion of material that was flung into Earth orbit from a giant impact (Canup, 2004b; *c.f.*, General Background). Some models suggest that accretion of this material was rapid, on the order of 100 years (Pritchard and Stevenson, 2000), leading to

an initially fully molten Moon. However, a lack of large-scale global contractional features have led others to postulate that the early Moon had a cold interior (*e.g.*, Solomon and Chaiken, 1976). The initial state of the interior is a topic of much debate and is fundamental to our understanding of thermal evolution.

Samples from the Apollo missions indicate that large scale melting did occur early in lunar history (*e.g.*, Taylor and Jakes, 1974; Warren, 1985) and is attributed to rapid accretion from an impact origin. The depth of this melting, known as the lunar magma ocean (LMO; *c.f.*, General Background), is largely unknown (ranging from 200–1000 km or more; Solomon and Chaiken, 1976; Nakamura, 1983) and debated but has significant ramifications for thermal evolution. For instance, if the LMO extended the entire radius of the Moon, it would have a much longer cooling history than an LMO that was only a few hundred kilometers deep.

The crystallization sequence of the LMO (Taylor and Jakes, 1974) and mantle mixing as suggested by mare and pyroclastic chemistries (Hughes *et al.*, 1988; Ryder, 1991) have led to the hypothesis of cumulate overturn. Dense, Fe- and Ti-rich mineral cumulates were formed in the latest stages of the LMO, leaving an inverse density sequence that would overturn due to gravitational instability (Ringwood and Kesson, 1976; Elkins-Tanton *et al.*, 2002; *c.f.*, General Background), releasing energy in the process. In addition, incompatible elements (particularly potassium, rare earth elements, and phosphorus (KREEP)) are the last to crystallize and the distribution of this layer, known as urKREEP, is particularly important for thermal evolution due its relatively high concentration of radioactive elements (Meyer *et al.*, 1971). At this point it is unknown if this layer was a global phenomenon, but surface observations suggest a high concentration on the nearside (Procellarum KREEP Terrane (PKT); Jolliff *et al.*, 2000). An asymmetric distribution of KREEP would lead to an asymmetric distribution of heat flux, further complicating thermal models. In addition, the asymmetric nature of crustal thickness (Ohtake *et* al, 2012; *c.f.*, Science Goal 2a) would act as a heterogeneous lid, affecting heat flux. It is believed that this KREEP concentration is one of the factors leading to the asymmetric distribution of mare volcanism (Wieczorek and Phillips, 2000).

The paucity of geophysical data regarding the interior has led scientists to unravel the thermal history through Apollo samples. Magmatic processes such as picritic glasses and mare volcanism provide clues to the thermal state of various depths in the Moon at various points in time. Picritic glasses have a large range of titanium concentrations and indicate source regions of 200 km or more (Wieczorek *et al.*, 2006; *c.f.*, Science Goal 2b and Science Concept 5). Mare basalts also have a wide range of compositions (BVSP, 1981; *c.f.*, Science Goal 2b and Science Concept 5), indicating a heterogeneous source region at depths of 100–500 km. Mare volcanism reached a peak at 3.6–3.9 Ga, with the majority of basalt erupting between 2.5–3.9 Ga (Head, 1976). However, there is evidence for recent (~1.1 Ga; Hiesinger *et al.*, 2011) and very old (cryptomare, >3.9 Ga; Antonenko, 1999) mare volcanism, although they are less prevalent (or obscured by regolith in the case of cryptomare). Thickness estimates for these magmatic episodes range from a few hundred meters (De Hon and Waskom, 1976) to 4.5 kilometers (Head and Wilson, 1992), with individual flows on the order of tens to hundreds of meters thick (Hiesinger *et al.*, 2002; Robinson *et al.*, 2012). However, much work remains to be done in characterizing flow unit thicknesses and basalt volumes globally, as this will provide important constraints on heat flux and secular cooling.

Volcanic processes record not only the thermal state of the magmatic source region, but also the magnetic field environment at the time of emplacement, revealing the energy state of a possible core dynamo. Thus, it is critical to conduct geologic and paleomagnetic studies of lithologies that could record the presence of an early dynamo.

Paleomagnetic studies

Rock samples are used to gauge the timing, intensity, and orientation of the purported dynamo. The Moon would have cooled faster than larger planetary bodies due to its small size (de Pater and Lissauer, 2010), thus making it more likely that a dynamo would have operated early in its history rather than later. Therefore, rocks containing magnetic minerals (*i.e.* iron oxides, iron-titanium oxides) that formed early in lunar history would have retained a signature of this dynamo. The lithologies that will be considered for sample return are mare basalt flows older than 3.0 Ga and impact melt sheets of basins that are Imbrian or older ($\geq$ 3.2 Ga), as previous studies suggests any lunar dynamo would have operated during this time.

Rocks that retain a magnetic signature are known to have natural remnant magnetization (Butler, 2004). This means that magnetic minerals (*i.e.* iron oxides) within the rock have cooled below their Curie

temperature (the temperature at which magnetic minerals hold a magnetization) in the presence of a magnetic field, even though there may not be one currently. Because ancient (≥ 3.2 Ga) lunar rocks have a natural remnant magnetization, albeit weak, it has been postulated that this magnetization was recorded in the presence of a lunar dynamo (*e.g.* Collinson *et al.*, 1977; Runcorn, 1994; Garrick-Bethell and Weiss, 2007a; Garrick-Bethell *et al.*, 2009). Seismic (Weber *et al.*, 2011) and LLR (Williams *et al.*, 2001; Khan *et al.*, 2004) detections of a small liquid outer core support the existence of a lunar dynamo early in lunar history.

Various lunar samples returned by the Apollo missions have been analyzed by paleomagnetic studies (*e.g.* Fuller, 1974; Collinson *et al.* 1977; Cisowski, 1983; Runcorn, 1994). However, a reanalysis of the data by Lawrence *et al.* (2008) showed the results obtained up to that point should not be considered scientifically robust due to uncertainties and problems with the method used. Since then, more reliable paleomagnetic measurements place dynamo activity at 4.2 Ga (Garrick-Bethell *et al.*, 2009; Shea *et al.*, 2012) and 3.6 Ga (Suavet *et al.*, 2012) (Fig. 2.33). Since there are no rock samples older than 4.2 Ga that can be used for paleomagnetic studies, it is unknown when the dynamo would have begun operating. Due to a lack of data and conflicting measurements from Tikoo *et al.* (2012a, 2012b) and Cournède *et al.* (2012), it is also unclear when this dynamo would have shut down.

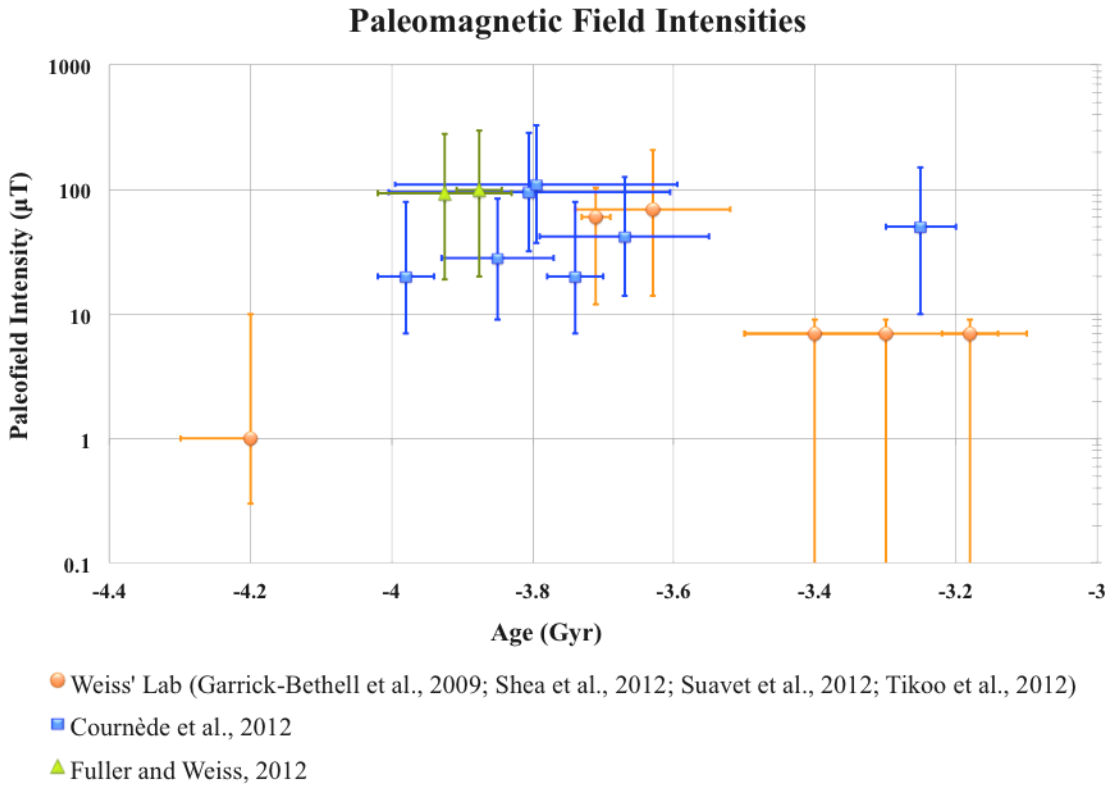

FIGURE 2.33 Paleomagnetic intensities of Apollo samples. Note that for many ages there is only one data point, which is suboptimal for paleomagnetic studies.

Central magnetic anomalies

Another way to constrain the strength and timing of the lunar core dynamo is through surface studies of central magnetic anomalies. The central magnetic anomalies are magnetic peaks or troughs near the center of large impact basins. They are proposed to be associated with thermal remanent magnetization of impact melt pools that had subsequently cooled below the Curie temperature and retained an ambient, steady state magnetic field (Halekas *et al.*, 2003; Hood and Halekas, 2010; Hood, 2011; Richmond and Hood, 2012). Since only a core dynamo can produce a magnetic field that lasts longer than the cooling timescale of the

melt rock, and basin age provides the timing of the magnetization, a surface study of these magnetic anomalies with a magnetometer traversal can provide the timing, orientation and energy state of the possible lunar dynamo (Halekas *et al.*, 2003). A survey of the basins that have these central magnetic anomalies compared to their relative ages paints a picture of the lunar dynamo that is in rough agreement with paleomagnetic studies (Fig. 2.34). A combination of surface magnetometer surveys and sample return studies at sites of interest is required to determine the exact state of the dynamo at particular times in lunar history.

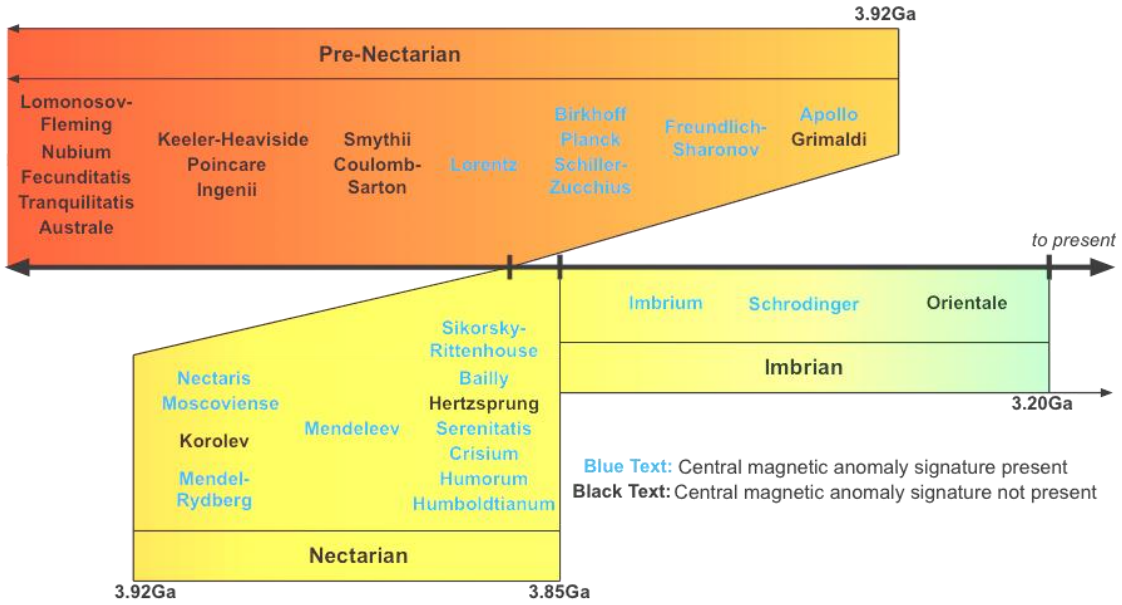

FIGURE 2.34 Basins, Pre-Nectarian to Imbrian in age, showing the temporal distribution of central magnetic anomaly signatures. Basins in the same column are in the same age class as defined by Wilhelms (1987). (Anomalies identified by Halekas *et al.*, 2003; Hood and Halekas, 2010; Hood, 2011; Richmond and Hood 2012).

Important Geologic Features for Sample Return

Sinuous rilles

Sinuous rilles are meandering channels common on the lunar surface (Schubert *et al.*, 1970). They are proposed to have formed either as collapsed lava tubes (*e.g.*, Greeley, 1971), lava channels with levees that formed in existing depressions (*e.g.*, Spudis *et al.*, 1988), or lava channels that cut into a pre-existing substrate due to thermal erosion (Hulme, 1973; 1982). A sinuous rille (Hadley) was visited by the Apollo 15 astronauts and was found to contain pristine, bedded mare in the upper walls of the rille (Figs. 2.35–2.37; NASA, 1972). Though the astronauts did not descend into the rille itself, descriptions of rille wall slope suggest an average of 25–30^{o} (NASA, 1972), and photographic analyses of rilles suggest there are numerous shallow entry points that sampling missions could exploit (Fig. 2.35).

Floor fractured craters

Floor-fractured craters have previously been catalogued by Science Concept 5 and are considered to represent pre-mare impact craters that were modified and uplifted during mare flooding (Schultz, 1976). While the fractures themselves may have been activated multiple times and may therefore expose mare flow units, they may also potentially have been exploited as magma conduits or dikes (Schultz, 1976). It is therefore unclear whether the appropriate samples for paleomagnetic studies (*i.e.*, multiple, pristine, exposed flow units) would be exposed at the surface. However, if they are indeed magma conduits or

dikes, it is likely that they would be magnetized in an active core dynamo, and thus are included as potential sampling sites.

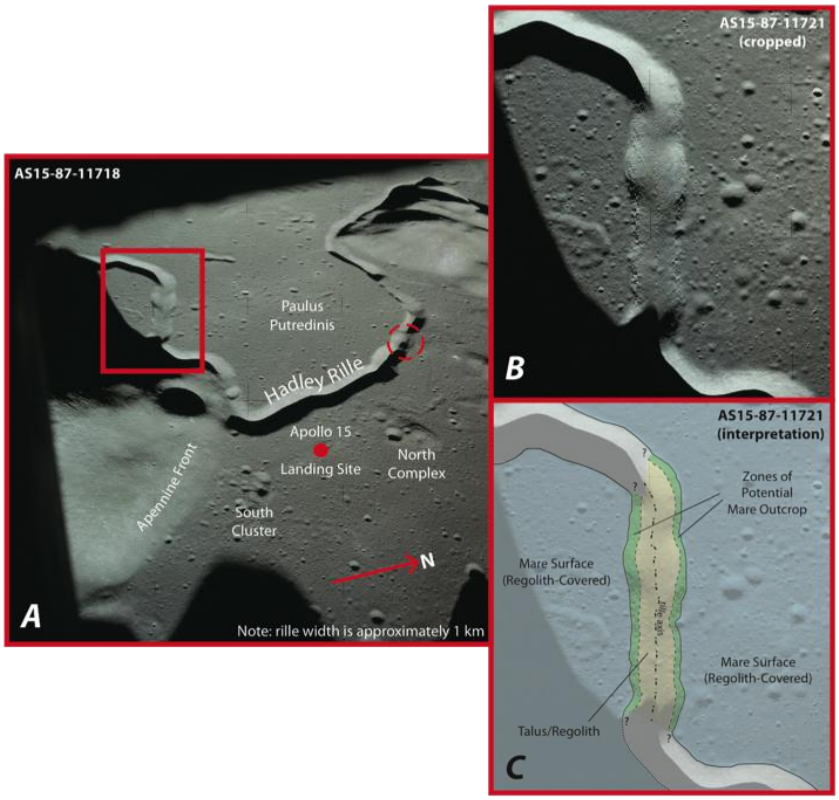

FIGURE 2.35 Apollo 15 Mission Photographs and Photogeologic Interpretation of Hadley Rille. (A) Regional view of the Apollo 15 landing site, taken from the Lunar Module (LM) as it descended to the surface. The dashed red circle outlines a potential shallow access point for the rille, and the red inset box indicates the area of detail in B and C. A scale bar is not shown, as it varies across the photograph, but the average rille width is ~1km. (B) Cropped photograph with elevated contrast and decreased brightness to show stratigraphic detail of Hadley Rille. (C) Photogeologic interpretation of B, with regolith-covered mare surface, zones of potential mare outcrops, and talus pile in rille center.

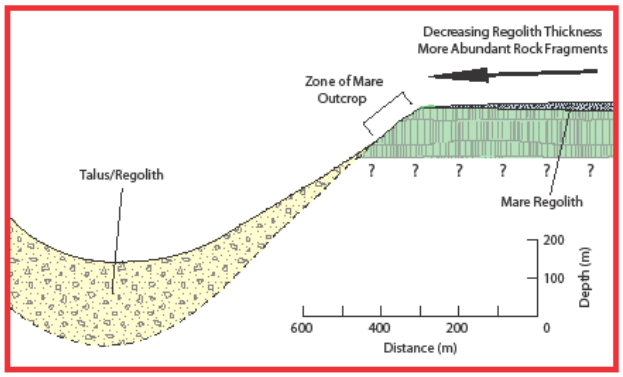

FIGURE 2.36 Cross-section of Hadley Rille area investigated by Apollo 15 astronauts (W to SW of landing site). The regolith thickness gradually decreases towards the edge of the rille; coherent bedrock is exposed for a number of meters below the rille edge but gives way to talus and regolith material with depth. Note

that the mare basalt itself is not thought to extend significantly below the edge of its exposure. Modified from the Apollo 15 Preliminary Science Report (NASA, 1972).

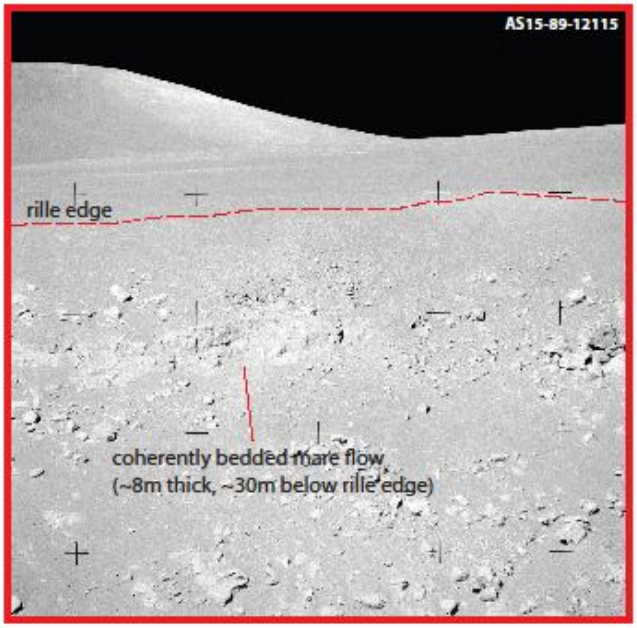

FIGURE 2.37 Mission photograph from Apollo 15 showing coherently bedded mare flow units in the western wall of Hadley Rille. This outcrop is ~30 m below the edge of the rille and ~8 m thick. Coherent flow units such as these are appropriate potential sampling sites for paleomagnetism studies.

Requirements

In situ Geophysics

The use of geophysical measurements will provide a complete density, conductivity, and thermal cross-section, thus helping to elucidate the thermal state of the interior and illuminate the workings of the planetary heat engine. Requirements for some geophysical techniques are detailed in previous sections (*c.f.*, Science Goals 2a, 2b, and 2c) and are not restated here, but it is recommended that the placement of geophysical instrumentation for Science Goal 2d be considered as a 'geophysical package' (see below).

Heat flow

The requirements for geophysical landing sites for Science Goal 2d are defined by the placement of four heat flow probes. While other geophysical instruments are necessary to fully address the Science Goal, a global set of stable and representative conductive heat flow measurements is required to determine the current thermal state of the Moon, and by extension, its thermal evolution since initial accretion and differentiation. Therefore, the satisfaction of the following requirements for heat flow probe placement should drive the geophysical landing site selection for this Science Goal:

(1) Probes must be placed at least 200 kilometers away from major crustal terrane boundaries (as defined by Jolliff *et al.*, 2000). Due to differences in crustal, megaregolith, and regolith thicknesses between terranes, major terrane boundaries are thought to experience potentially significant heat flow focusing effects, such that heat is deflected towards thinner crustal sites (Conel and Morton, 1975; Warren and Rasmussen, 1987; Cohen *et al.*, 2009).

(2) The edges of impact basins should be avoided for the same reason as terrane boundaries. The effects of heat flow focusing may be particularly pronounced at these sites due to abrupt crustal thickness changes (W. Kiefer, pers. comm.). Though no rigorously determined values

for the lateral extent of heat flow focusing is presently found in the lunar literature, we suggest a minimum buffer of 50 kilometers from these locations.

(3) Avoid significant topographic variations, craters (especially recent), boulders, and local, m- to km-scale heterogeneities (Langseth *et al.*, 1976; Kiefer, 2012). As these have the potential to create localized subsurface heat flow gradients, precise heat flow measurements require a flat, consistent, laterally uniform surface (Langseth *et al.*, 1976).

(4) Both active and passive measurements of thermal diffusivity (κ) should be obtained for measurement accuracy; whereas active measurements can be completed on the order of ~200 hours (*e.g.*, Grott *et al.*, 2010), passive assessment of diffusivity requires shallow (<3 meter) temperature profile measurements collected over a multi-year time span (Langseth *et al.*, 1976). Given that the passive measurements take advantage of the diurnal and annual lunar thermal wave to sample bulk material properties (Cohen *et al.*, 2009), heat flow probes should be placed out of permanent or temporary shadow to avoid thermal perturbations. This includes temporary thermal shadows from the deployment of other geophysical instruments (Kiefer, 2012).

(5) Probes should be placed in sites of minimal ejecta blanket thicknesses, especially from large basins that excavate KREEP-rich material (*e.g.*, Imbrium). This is to ensure that heat flow probes measure vertical conductive heat flow without contamination from surface radiogenic material (*e.g.*, Hagermann and Tanaka, 2006).

(6) Probes must penetrate to >3 meters depth to sample the thermal gradient at least a meter beneath material strongly affected by the lunar thermal wave (upper 1–1.5 meters) (Cohen *et al.*, 2009). Measurements must be made at regularly spaced increments (*e.g.*, every 10 centimeters). This is required to constrain the thermal gradient and will also account for depth variations in thermal conductivity (Langseth *et al.*, 1976). Combining this requirement with (4), above, the heat flow probes must penetrate below 3 meters but also measure temperature at intervals from the surface to the base of the probe.

(7) Landing sites must be located in areas of approximately "average" crustal thickness within each of the four lunar terranes of Jolliff *et al.* (2000). Considering the compositional and thickness differences between each terrane, and in conjunction with the data from other geophysical instruments, a single heat flow measurement from each terrane (four total) will establish a mean global heat flow estimate for the entire Moon.

Additional landing sites for heat flow measurements, while not explicitly required, would allow consideration of specific contributions to the vertical conductive heat flow of the Moon. For example, placement of an additional probe in a thin crustal site within the FHT-A terrane would provide constraints on the different mantle and crustal contributions to heat flow (Kiefer, 2012), which would help determine the distribution of radiogenic (*i.e.*, heat-producing) elements in the Moon. Similarly, placement of an additional heat flow station on a thick ejecta blanket will allow estimation of the thermal contributions from radioactive elements in ejecta. However, the principal purpose of a heat probe array for Science Goal 2d should be aimed at establishing a first-order estimate of global heat flow, and thus these anomalous sites should be considered secondary targets.

Seismology

A passive seismic network is required to evaluate lunar density structure, core size, and core state (*c.f.*, Science Goals 2a, 2b, and 2c). While the placement of an equilateral tetrahedron of four seismic sensors on the lunar surface would be ideal for obtaining deep interior structure (*c.f.*, Science Goal 2b), it is not as limiting as other landing site requirements for this Science Goal. The placement of a seismometer within each lunar terrane as defined by the heat flow requirements will allow enough resolution to address the density and thermal structure of the lunar interior, especially given the coincident locations of seismic and heat flow probes. However, the antipodes to known locations of DMQ should be incorporated as a rigorous requirement for at least one station, as seismic receivers placed at these sites are crucial to determining the size and state of the lunar core (*c.f.*, Science Goal 2c).

EM Sounding

EM sounding measurements are used to determine the conductivity structure of the lunar interior (*c.f.*, Science Goals 2b and 2c). Only a single measurement is required with no concern regarding location.

LLR

A minimum of one additional LLR retroreflector station, in conjunction with the current configuration, can constrain the elastic properties of the lunar mantle and a number of core parameters (*c.f.*, Science Goal 2c).

Magnetometer Traverse

Surface magnetometer measurements across the peak of a central magnetic anomaly can provide information on the state of the lunar dynamo at a particular time (*i.e.*, during basin formation). Only a small number of basins with central magnetic anomalies have been identified from orbital data (Halekas *et al.*, 2003; Hood and Halekas, 2010; Hood, 2011; Richmond and Hood, 2012).

Sample Return

A number of criteria must be met in order to obtain the samples necessary for accurate paleomagnetic studies:

1. Rocks of the age when it is likely that a dynamo could have existed, *i.e.*, 3.0–4.43 Ga (formation of the Moon)
2. Rocks that have retained their original cooling orientation or their original orientation can be inferred (*i.e.* by known strike/dip and uplift mechanism)
3. Rocks with the mineralogy necessary to record a magnetic field
4. Rocks that are minimally shocked (<5 GPa)

Additionally, there are a number of precautions that must be taken in order to obtain appropriate samples for paleomagnetic studies (Garrick-Bethell and Weiss, 2007b): (1) the original orientation and context of the rock must be documented for interpretation of paleofield geometry, (2) several rocks from a single outcrop must be sampled for measurement precision, and (3) rocks must be protected from all ambient magnetic fields during collection, transit, and storage. Considering these criteria, several issues arise in the use of Apollo samples for paleomagnetic data. Most of the collected samples were not from their original outcrop, so original orientations and contexts are unknown. There were also only a few samples with sufficient magnetization collected in a given area, resulting in only one data point for some ages (Fig. 2.33). In addition, all Apollo samples were exposed to some type of ambient magnetic field (space suit, spacecraft, or Earth) such that the magnetization of the rock has been modified from its original state. The precautions mentioned above must be considered for future paleomagnetic samples.

Methodology

In situ Geophysics

The selection of geophysical landing sites in this Science Goal is primarily made to fulfill the requirements of a global heat flow study. After mapping locations where heat flow probes can be placed, a subset of these locations where seismology, EM sounding, and LLR could also be implemented was mapped.

Heat Flow

Identification of sites suitable for heat flow measurements requires locating regions where the measurements cannot be taken:

1. A 200 km buffer zone was created around the terrane boundaries. Similarly, 50 km buffer zones around each of the basin rims (defined as ≥300 km diameter; Spudis, 1993) and 1 km buffers around mapped ejecta material (as used by Science Concept 5) were created to address measurement requirements.
2. A slope map was then produced from the LOLA 128 ppd DEM, and 20° or larger slopes were identified to avoid heat flow focusing effects.

3. Permanently shadowed regions over the lunar poles, from Mazarico *et al.* (2011), were mapped.

Seismology

For brevity, only the ideal configuration of an equilateral tetrahedron was considered. The placement of a single seismometer acts as a control point for the other vertices of the equilateral tetrahedron. Due to the flexible requirements regarding landing site locations, this configuration can be placed essentially anywhere on the Moon.

EM Sounding

As there are no requirements that must be satisfied for the location of an EM instrument, there are no methods to be outlined. Since the location requirements for EM sounding are trivial, we suggest the inclusion of an EM sounding instrument in a geophysical package (see below).

LLR

Methods regarding the placement of LLR stations are outlined in detail in Science Goal 2c.

Magnetometer Traverse

The locations of central magnetic anomalies are mapped as targets for magnetometer studies. Due to the nature of their formation, they occur at anomalously thin crustal sites and cannot be included along with any heat flow measurements.

Sample Return

To fulfill the requirements listed above, two target lithologies were considered: mare basalt flows and melt sheets of large impact basins. The necessary rock mineralogy to record a magnetic field was not used as a stringent requirement for landing site selection as it is assumed that basalts contain the necessary concentration of Fe, and impact melt sheets incorporate enough Fe during formation. Other Science Concepts have also proposed to sample mare basalts and impact melt sheets. However, samples for Science Goal 2d need to be from relatively unshocked outcrops where the original orientation of the rock is known or can be determined. Oriented samples are required to test if the observed surface magnetization is the result of a lunar dynamo (NRC, 2007). The methodologies regarding sample return for each of these are different and are described in more detail below.

Mare basalts:

(1) Mare basalt flows from ~3.0–4.0 Ga would have cooled in the presence of a lunar dynamo and therefore are appropriate for paleomagnetic analysis.

- Mare basalt flow ages are based on crater counting ages from Hiesinger *et al.* (2011) and Morota *et al.* (2011). Maps of mare units and their ages were digitized and a new shapefile of mare with model ages between 3.0 and 4.0 Ga was created.

(2) Sinuous rilles, craters within mare units, and floor-fractured craters can be used to sample oriented mare basalt flows.

- A recent dataset cataloguing global sinuous rille occurrence and distribution (Hurwitz *et al.*, submitted) was combined with the mare age distribution map in (1) to produce a map of all possible sinuous rille sampling locations.
- Exposed crater walls within mare units also allow for paleomagnetic sampling. However, in order to provide the appropriate samples, the crater size must not only be large enough to penetrate through the average 5-meter-thick mare regolith (Shkuratov and Bondarenko, 2001; Fa and Jin, 2010; Bart *et al.*, 2011; Fa and Wieczorek, 2012) to underlying bedrock, but also be large enough to preserve coherent, layered mare flows in its walls. This is expected to be the case for a minimum 0.5–1 kilometer crater diameter (V. Sharpton, pers. comm.).
    - The LPI crater database (Losiak *et al.*, 2009, revised by Ohman, 2011) was used as a starting point for possible landing sites; craters of the appropriate size that were emplaced within mare units of the appropriate age were identified in ArcMap. Only Copernican craters were considered to ensure the necessary bedrock exposure. However, essentially

any "young" crater greater than 0.5 kilometers in diameter could be considered a potential sampling location for paleomagnetism. Samples should be obtained from minimally-shocked or low-shock material.

- Compiled literature data on floor-fractured craters were obtained from Science Concept 5. Only those floor-fractured craters identified as "certain" were included in this analysis.
- Additional sampling sites for undisturbed mare may be available at linear rilles (Head and Wilson, 1993) or sublunarean voids or skylights (*e.g.*, Robinson *et al.*, 2012). However, their distribution is poorly characterized as of yet, and they have not been included in this analysis. Ongoing and future work to characterize their distribution should be considered prior to any sample return mission.

Impact melt sheets:

(1) Melt sheets of impact basins dating from the Imbrian and pre-Imbrian would have cooled in the presence of a lunar dynamo.

- Imbrian and older basins have been targeted, where only basins of ≥ 300km diameter (Wilhelms, 1987; Spudis, 1993) are considered.

(2) Craters of Copernican age (>800 Ma) within a basin transient cavity are used to sample oriented melt sheets.

- Since melt sheets of basins in (1) are old features, they have been covered by regolith and, in some locations, mare basalt. Craters are able to excavate beyond these upper layers and expose oriented melt sheets.
- Only Copernican craters are used due to their fresh morphology and their lack of regolith cover, providing the best exposures of melt sheets. Only Copernican craters from the LPI lunar impact crater database (Losiak *et al.*, 2009, revised by Ohman, 2011) were considered.
- There is greater confidence that the melt sheet is contained within the transient cavity as opposed to the final diameter of impact basins. In order to ensure melt sheet exposure, only Copernican craters within the transient cavity are considered.
    - The diameter of basin transient cavities was calculated using Equation 5 from Kring (1995):

$$R_C = 0.86 R_{TC}^{1.07} \quad (2.18)$$

where R_C is the complex crater radius and R_{TC} is the radius of the transient crater, all in meters. However, it is important to note that this relationship is for complex crater morphologies and is assumed to translate to basin scale impacts.

(3) Assess the regolith/megaregolith thickness that would cover the melt sheet for basins that satisfy (2).

- Ejecta from large impact basins has greatly contributed to regolith covering. Thickness of this regolith was calculated using the ejecta scaling law of McGetchin *et al.* (1973) and Kring (1995):

$$t = 0.14 R^{0.74} (r/R)^{-3.0 \pm 0.5} \quad (2.19)$$

where t is ejecta thickness, r is the range from the center of the crater, and R is the crater radius, all in meters. Only regolith generated from large impact basins was considered.

(4) Assess mare thickness that would cover the melt sheet.

- Mare thickness estimates from De Hon (1974), De Hon and Waskom (1976), Hörz (1978), De Hon (1979), Gillis (1998), Hiesinger *et al.* (2002), and Thomson *et al.* (2009) were used.

(5) Calculate the depth to the melt sheet using values from (3) and (4).

(6) Compare the depth of craters from (2) with thickness estimates from (5) and determine if the melt sheet is exposed in the upper crater walls.

- Only upper crater walls are considered due to the presence of breccia and slumped wall material that covers the crater interior (Fig. 2.11). The best outcrop exposures will also be present in the upper crater wall.

(7) Create a map where all craters satisfy (2) and (6).

Floor-fractured craters could also potentially sample oriented melt sheets of large impact basins, but the nature of fracture formation, sampling depth, and their ability to expose melt sheet below megaregolith is not well understood. If floor-fractured craters are indeed associated with mare volcanism, as suggested by Schultz (1976), it may be that impact melt sheets have been influenced by this volcanism, may not have an accurate paleomagnetic record, and/or may not be exposed in the fracture walls. Therefore, only fresh exposures at Copernican craters are considered for this study.

Suggested Landing Sites

In situ Geophysics

Heat Flow

All possible locations where a representative heat flow measurement can be taken are shown in Fig. 2.38. The 'thin', 'typical, and 'thick' terrane crustal thickness map from Fig. 2.14 has been used as a base map, as it would be preferable to take measurements in 'typical' crustal thickness locations from each terrane. In addition to the work carried out here, a comprehensive review of lunar surface incident radiation needs to be completed to locate regions at lower latitudes that may be permanently shadowed, and regions that may be partially shadowed throughout the lunar day.

Seismology

Locations of equilateral tetrahedron vertices are not shown here due to the shear number of possible station locations, but an example is shown in Fig. 2.23 (*c.f.*, Science Goal 2b). To calculate where the geophysics packages can be placed, whilst meeting the requirements for heat flow and seismology, a strict tetrahedron configuration was rotated at 1° intervals in the x, y, and z directions. If any of the tetrahedron apices were located within a region removed due to heat flow, then that configuration was discarded; there must also, there must be one station within each of the terranes. It is recognized that this only gives an indication of the available sites, and that more will be available when this study is carried out at finer resolution, using higher resolution (*e.g.* 100 m WAC LOLA DTM), and newer datasets (*e.g.* GRAIL). Optimized station locations to address the geophysical and sample return elements are shown in Fig. 2.44. The same rotation of a strict tetrahedral configuration is employed in the Final Map and A33 Case Study.

EM Sounding

A map of landing sites for EM sounding has not been created because a measurement can be taken anywhere on the surface.

LLR

Possible LLR stations that will increase the coverage of the current network are presented in Science Goal 2c (Fig. 2.30). These locations will be considered when discussing the deployment of a geophysical instrument package (see below).

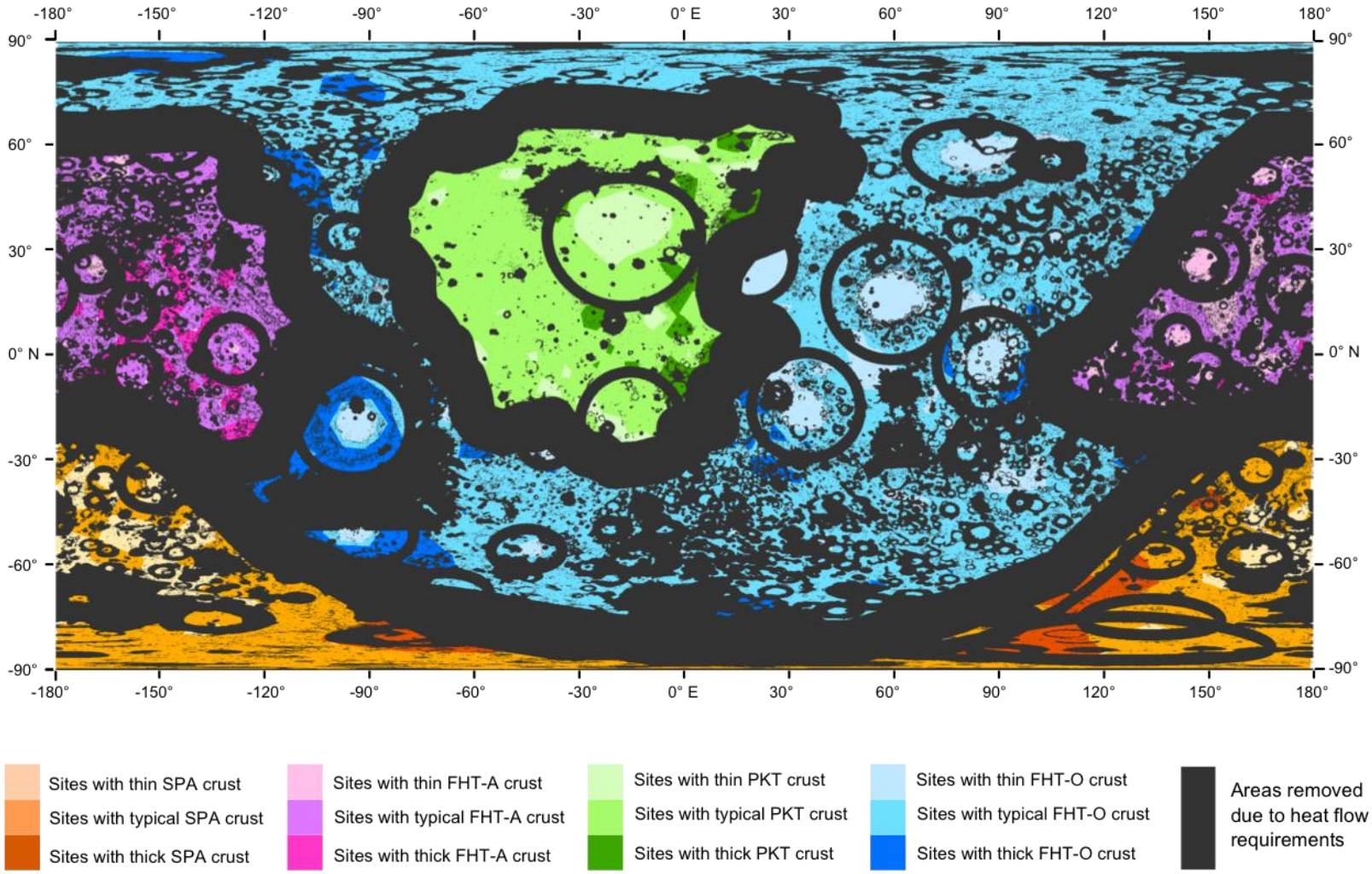

FIGURE 2.38 All locations where representative global heat flow can be measured. Thin, thick, and typical crustal thickness can be used to gauge the effects of crustal thickness on heat flow.

Magnetic Traverse

Locations for potential magnetic traverses are presented in Fig. 2.39. The locations of basins that contain central magnetic anomalies are shown along with the strength of each anomaly, as detected at 30–40 km altitude by Lunar Prospector.

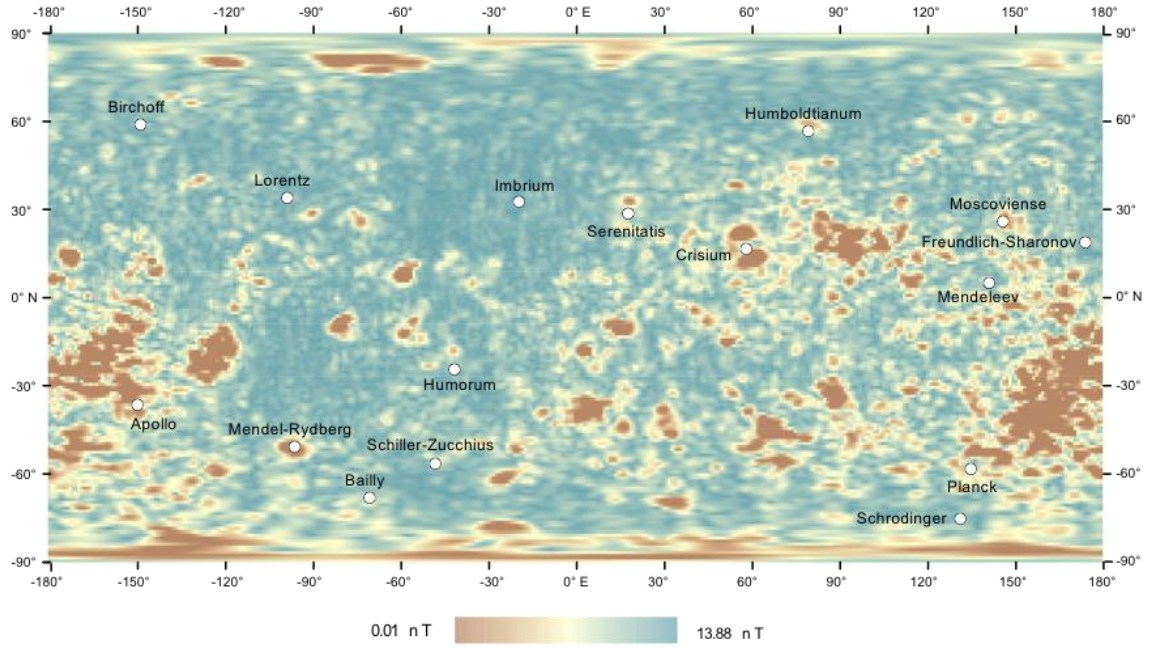

FIGURE 2.39 Locations of central magnetic anomalies within large impact basins. Lunar Prospector magnetometer data is underlain by a WAC Global Mosaic.

Geophysical Package

It is highly recommended that the geophysical instruments discussed above be grouped into a 'geophysical package'. This is important to reduce the number of required individual landers. However, since basin centers must be avoided for heat flow measurements due to their anomalously thin crust, surface magnetic traverses of central magnetic anomalies cannot be undertaken along with the proposed geophysical package.

Sample Return

Mare basalt

Mare bedrock exposures that satisfy the above requirements are shown in Fig. 2.40. The appreciable number of potential landing sites allows flexibility with other mission requirements or Science Goals. However, given the uncertainty of floor-fractured crater sampling, we suggest that mission planning be directed either at sinuous rilles or crater walls. Of these two, sinuous rilles are potentially the best sampling sites due to their unshocked nature and undisturbed orientation.

Additionally, the sampling of more than one mare bedrock site will greatly expand the potential scientific benefit. In addition to characterizing the core dynamo over a larger age range, it would allow investigation of mare flow thicknesses, chemistry, and thermal evolution of the Moon over time (and would therefore also be relevant for Science Goal 2b).

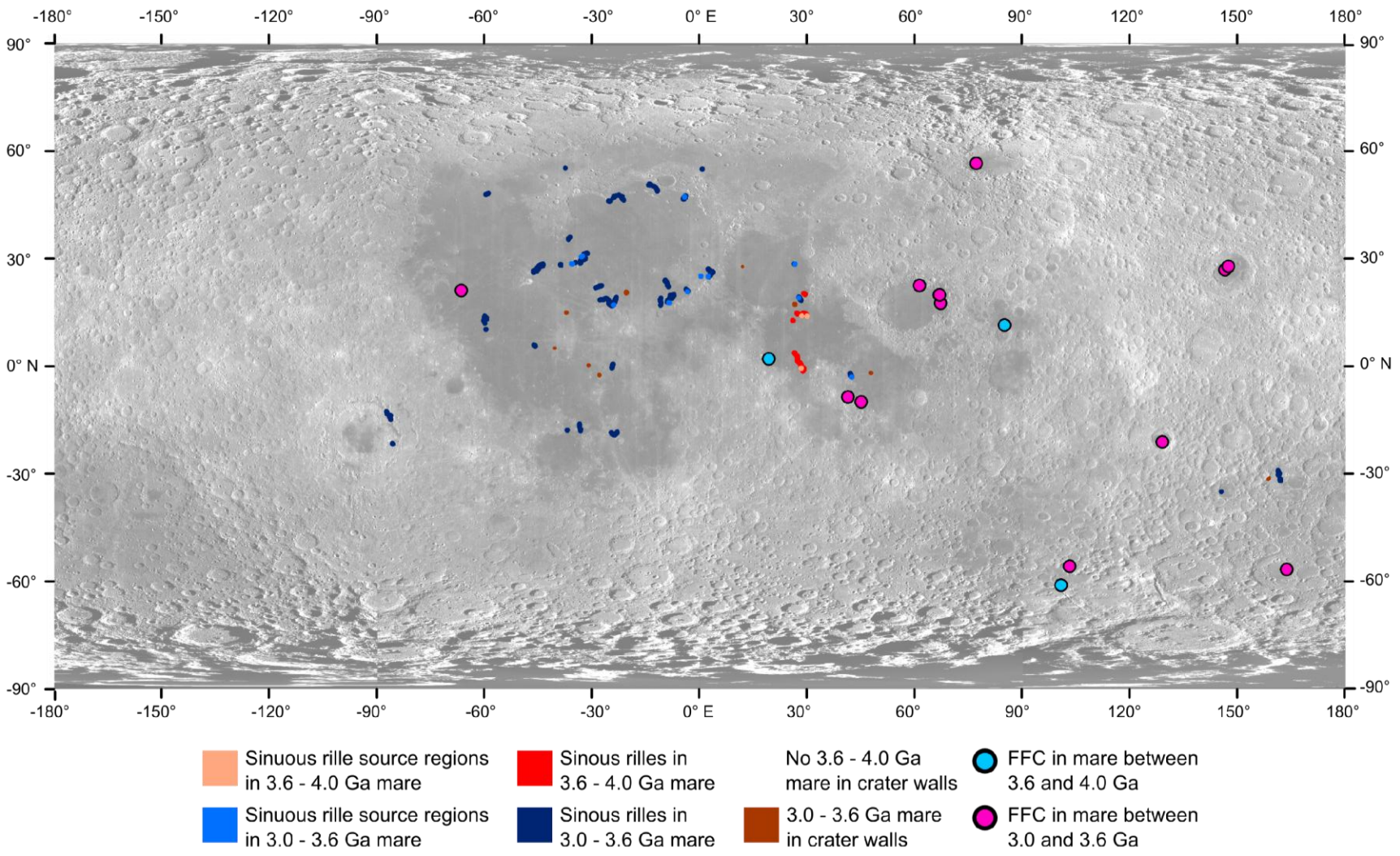

FIGURE 2.40 Locations where oriented mare basalt flows can be sampled.

Impact melt sheet

Using the LPI crater database (Losiak *et al.*, 2009, revised by Ohman, 2011), there are two craters that satisfy the requirements for sampling intact basin melt sheets: Birkhoff (Z) within the Birkhoff basin and Guthnick within the Mendel-Rydberg basin (Fig. 2.41).

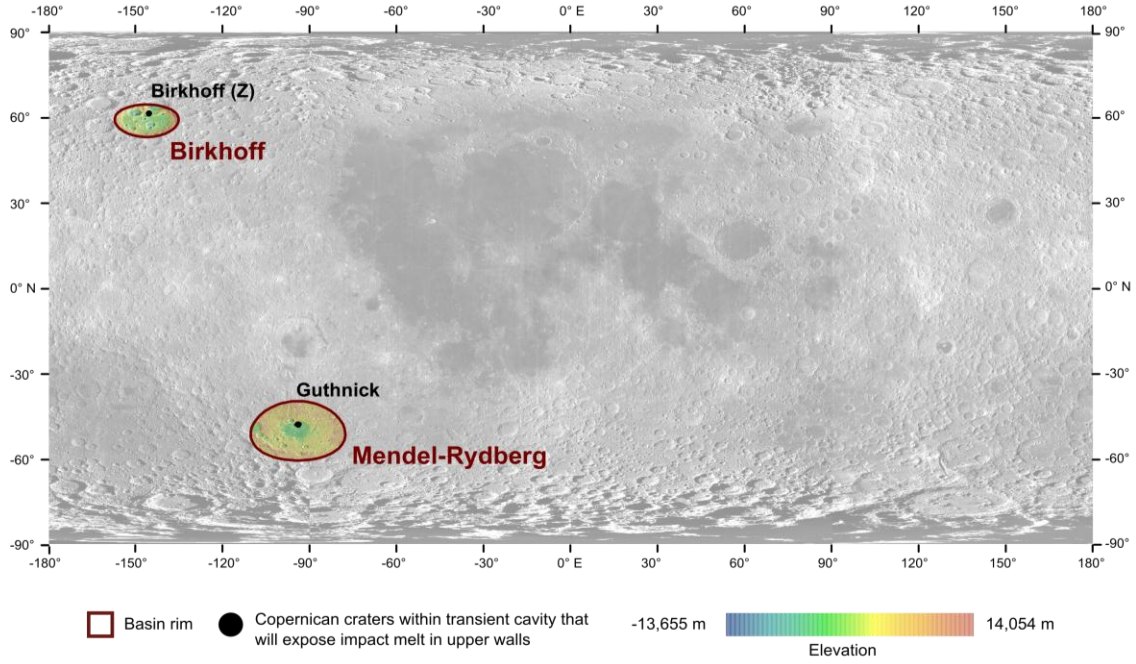

FIGURE 2.41 Locations that satisfy the requirements for oriented melt sheet sample return. Background is WAC Global Mosaic.

Upper walls of craters are characterized by their relatively steep slope and scarp-like morphology. This slope becomes more gradual as it nears the basin center due to slumping of material and late stage crater modification (Melosh, 1989). The first inflection point of this slope is the cutoff point of the upper crater wall and it is above this point that samples should be obtained (black arrows in Figs. 2.42 and 2.43).

However, it should be noted that melt sheet exposures are based on calculations and that detailed photogeologic mapping of Birkhoff (Z) and Guthnick should be done as part of the landing site reconnaissance. In addition, the LPI crater database is not a complete list of lunar craters and there could potentially be more craters that satisfy the requirements listed above. Any Copernican crater within the transient cavity of an Imbrian or older impact basin that exposes depths, within their upper wall, below the regolith thicknesses are viable landing site options (regolith thicknesses for Birkhoff and Mendel-Rydberg are shown in Table A2.7).

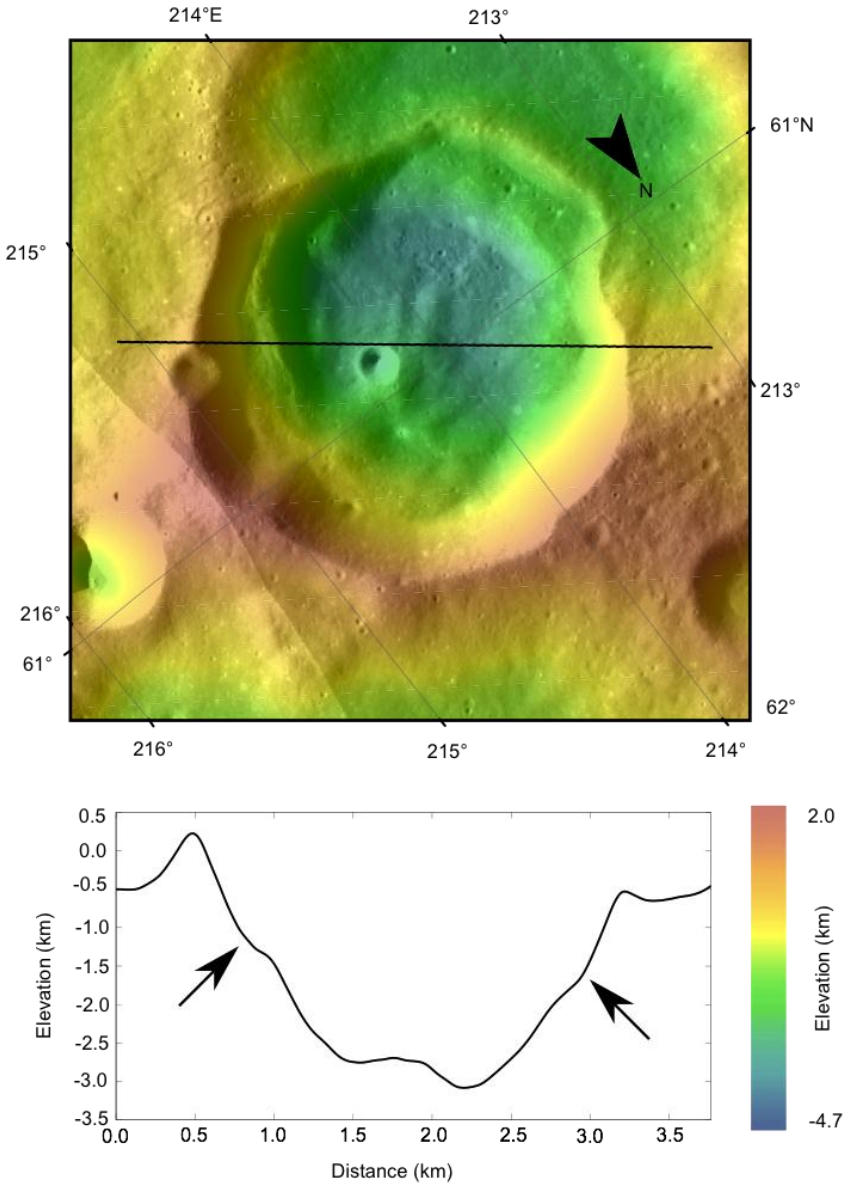

FIGURE 2.42 Topographic profile of Birkhoff (Z). Black arrows indicate the transition from upper crater wall to slumped material, as shown by an inflection in the slope. The vertical exaggeration of the elevation profile is ~1.5:1.

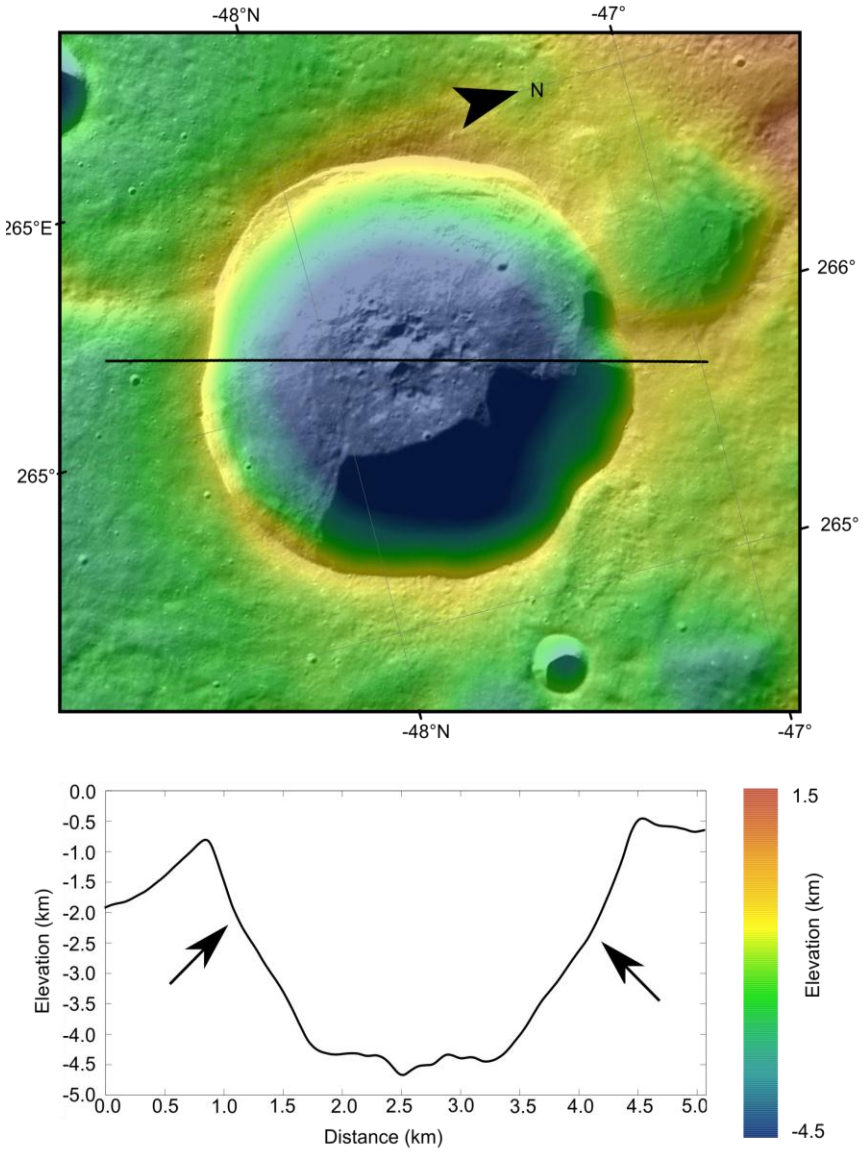

FIGURE 2.43 Topographic profile of Guthnick. Black arrows indicate the transition from upper crater wall to slumped material, as shown by an inflection in the slope. The map uses a polar projection centered on -48°N 266°E, and the vertical exaggeration of the elevation profile is ~2:1.

Conclusions

Figure 2.44 shows all locations, geophysical and sample return, where Science Goal 2d can be addressed. The colored dots show all the locations where sampling can be carried out at one or more of the four sites within that particular tetrahedral configuration. Solid orange denotes locations of tetrahedral vertices where the site in SPAT can also obtain a sample that will address this Science Goal; orange and black dots indicate vertices where samples can be obtained in SPAT and PKT. Blue shows tetrahedral locations where the location in FHT-O can also obtain a sample; blue and white dots can return samples in FHT-O and PKT. Green dots denote tetrahedral locations where the site in PKT will return a sample. Due to the nature of sample return for this Science Goal, no samples are needed from FHT-A.

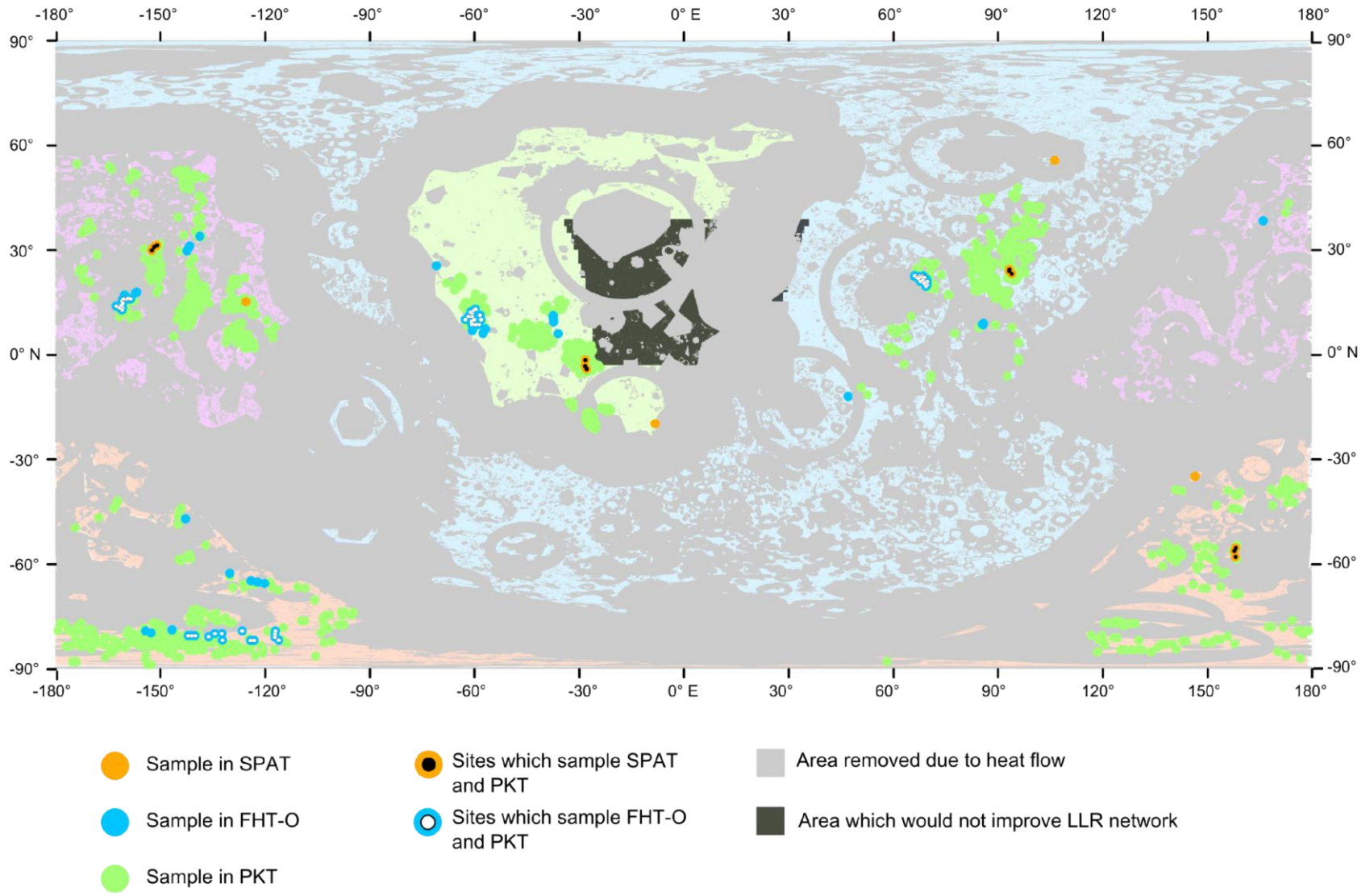

FIGURE 2.44 All locations that will address Science Goal 2d (see text for explanation).

FINAL LANDING SITES: GEOPHYSICAL METHODS

The final maps which include the geophysical packages for Science Concept 2 as a whole are shown in Fig. 2.45. This shows the locations where geophysical packages may be placed. Each geophysical package should include a seismometer, EM sounding instrument, and heat flow probes; any nearside package should also include an LLR retroreflector. It is worth noting that this is not an exhaustive list of geophysical requirements, but rather is the minimum required to address the geophysical aspects of Science Concept 2 as a whole.

We emphasize that four stations with instruments for *in situ* geophysical analyses are the minimum required to address all Science Goals contained in Science Concept 2, by constraining the present-day global configuration of the lunar interior (sample return is required to address past interior state and evolution to the present). However, even a single geophysical station with these instruments would still provide useful knowledge, and thus we emphasize that *any* further missions to the surface of the Moon should include such a geophysical package regardless of their location. For example, EM sounding has minimal location requirements, and a single EM measurement could provide a one-dimensional conductivity cross-section of the lunar interior. A single passive seismometer would allow consideration of crustal thickness in the vicinity of the landing site, as well as at locations where meteoroid impacts occur (if they can be observed from Earth or from orbit) (Chenet *et al.*, 2006). Even along terrane boundaries where heat flow measurements might be compromised by abrupt changes in crustal thickness, a general estimate of conductive heat flux would be useful and interferences could be perhaps be modeled and subtracted from the measurement. Finally, the placement of a single LLR retroreflector on the nearside, outside of the current network, will improve the accuracy and three-dimensionality of laser ranging experiments.

As in Science Goal 2d, the locations of the geophysics packages have been calculated for 1° rotations of a tetrahedral configuration, taking into account areas removed due to heat flow requirements, and extending the current LLR network. There are considerably more configurations available here, as requirement that at least one of the tetrahedron apices must overlap with a Science Goal 2d sample site has been removed. Also shown are the moonquake locations and antipodes, as discussed in the Science Goal 2c. A seismometer should be placed within a moonquake nest antipode and within 60° of the corresponding moonquake nest, as in the A33 moonquake nest case study. A relatively well-constrained moonquake nest should be chosen; it is not necessarily required to use only a farside moonquake nest as in the A33 Case Study, as this was chosen specifically to enable two LLR stations to be placed on the nearside. The potential landing sites in Fig. 2.45 do not greatly improve the southern extent of the current LLR network, particularly due to the tetrahedral configuration required as part of the geophysical package. It is therefore advised to add an additional geophysics package in the southern hemisphere, on the nearside, to increase the N-S extent of the current LLR network; this would improve the accuracy and precision of ephemeris and libration measurements.

In the ideal case, clusters of three seismometers in a triangular configuration should be placed at the corners of tetrahedron, as discussed in Science Goal 2b. This would help begin to address the nature of upper mantle structure and determine shallow moonquake distribution. However, we recognize that thirteen geophysical landers are unrealistic at the present time, and therefore the four-station configuration is our baseline proposal.

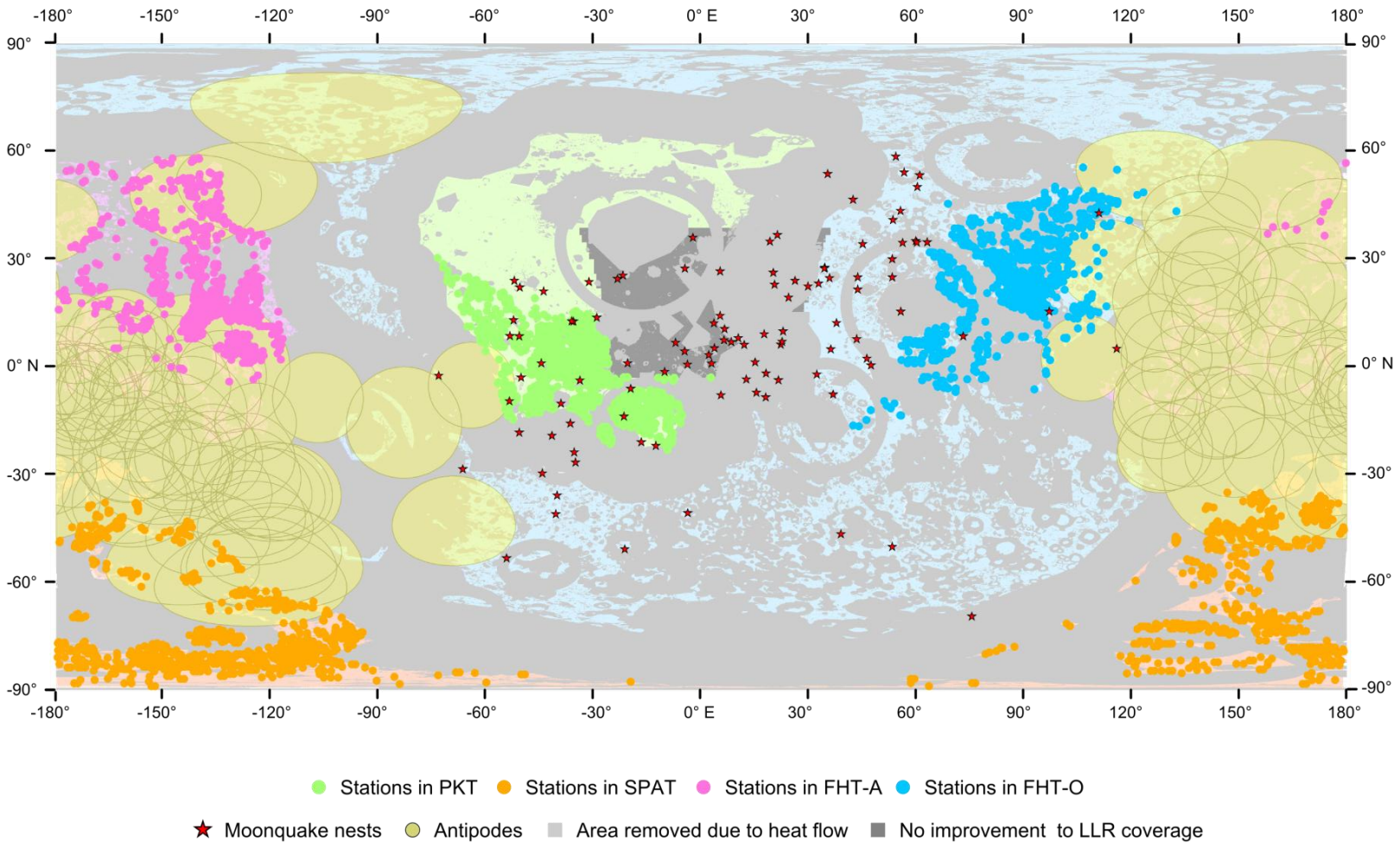

Figure 2.45 Final geophysical landing site map for Science Concept 2. The colored dots represent the apices to a tetrahedral geophysical configuration, where a lander at each apex would include a seismometer, EM sounding instrument, and heat flow probes. Any nearside station would also include an LLR retroreflector. Note that each colored dot represents the apex of a specific tetrahedron and correlates to three other specific dots (ensuring one station in each terrane).

FINAL LANDING SITES: SAMPLE RETURN METHODS

Sample return landing sites for Science Goals 2a, 2b, and 2d are combined and superimposed on a LOLA topography map mosaic (shown in Fig. 2.46). (Recall that sample return is not required to address the objectives of Science Goal 2c.) Some of the landing sites for 2a, 2b, and the mare basalt landing sites from 2d are within proximity to one another and thus could be sampled together during a single sample return mission. The exceptions are the landing sites for addressing the impact melt sheet requirements in Science Goal 2d, which are located far from any other suggested landing sites and thus would require a separate mission.

We note that a least one sample return mission is required to address each of the Science Goals (except 2c). *In situ* and orbital geophysical analyses can provide information on the current interior structure of the Moon, which is an important constraint for models of lunar evolution, but geochemical, geochronologic, and paleomagnetic analyses of additional samples are necessary to describe the changes in the structure and stratigraphy of the lunar interior with time.

Two example case studies for sample return were chosen, one on the farside (Moscoviense; Fig. 2.53) and one on the nearside (Nectaris; Fig. 2.54), which are discussed in detail below. These two case studies focus on areas where all or a subset of the three sample return Science Goals could be addressed by a single landing site.

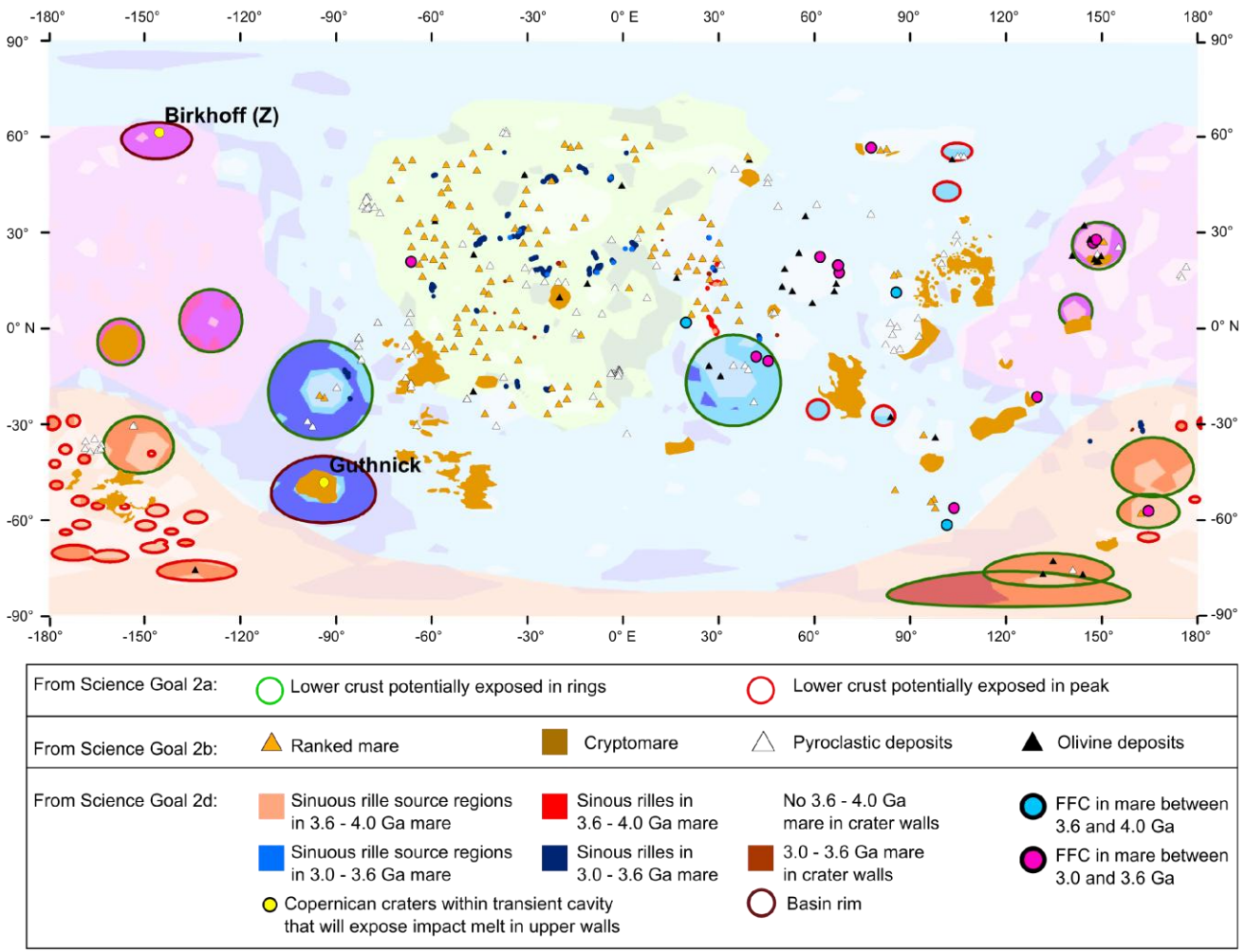

Figure 2.46 Map showing all the sampling locations for Science Concept 2. In order to fully address sample return for Science Goal 2a, samples need to be collected from each of the four terranes, whereas it is possible to address Science Goals 2b and 2d with a single landing site each.

SCIENCE CONCEPT 2 FINAL MAPS

The geophysical and sample return elements of Science Concept 2 are shown together in Fig. 2.47 and 2.48. Figure 2.47 shows all the possible tetrahedral configurations for the geophysical packages along with the sample return elements. This map shows that it is possible to sample for at least one of the Science Goals at one or two of the apices of the tetrahedral configuration, but it is not possible to complete all aspects of the sample return within this Science Concept using a tetrahedral configuration. It is therefore suggested that the sample return and geophysical elements of Science Concept 2 be kept separate, but that a geophysical package is included at all sampling sites. This will ensure that neither the geophysical nor the sample return elements of this Science Concept will be compromised. The addition of further geophysical packages at sampling sites can then be used to add complexity to the baseline understanding obtained using the geophysical configuration alone, by providing additional data at sites that have properties outside of what is thought to be typical for that terrane, such as anomalously thick or thin crust. These data can be used to provide better constraints on models of crustal thickness, the thermal state of the Moon, and mantle density and composition.

Figure 2.48 shows all the tetrahedral configurations that satisfy the entirety of Science Goal 2d, and the sample return elements of Science Goals 2a and 2b. This demonstrates that some of the configurations shown in Fig. 2.48 for Science Goal 2d overlap with sampling sites for Science Goal 2b and part of Science Goal 2a. Because there is not an 'ideal' configuration of four landers which enables all the geophysical and sampling elements of the whole Science Concept to be completed, additional landings are required to address Science Concept 2as a whole.

A maximum of eight landers is required to fully address the geophysical and sample return aspects of Science Concept 2. However there is likely to be overlap between at least one of the geophysical and sample return sites, such that seven landing sites may be sufficient to address this Science Concept. Assuming a geophysical package is added at each of the landing sites, a total of seven geophysical packages would be placed on the surface for this proposal. The nature of the sampling studies means that some of these sites are likely to be at locations of relatively thin crust, as many of the sampling sites are within basins or large complex craters, and thus will improve the models as discussed above.

Though a strict tetrahedral configuration of four landing sites has been used above, it may be possible to relax the tetrahedral configuration if more than four sites are chosen whilst maintaining global coverage of a passive seismic network. This may enable better sampling sites to be chosen and fewer total landing sites to be required; however, it would still not be possible to sample all lunar materials required to address this Science Concept.

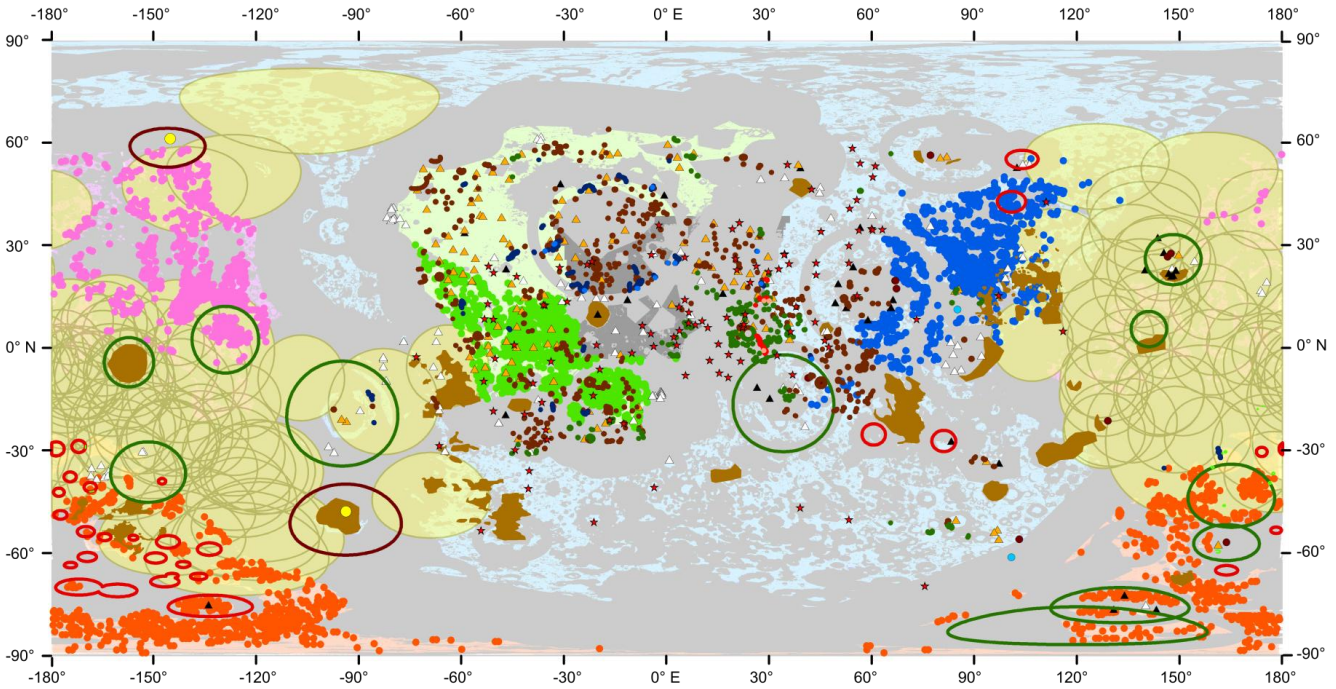

Figure 2.47 Final map displaying both geophysical and sample return aspects for all Science Goals in Science Concept 2, with the tetrahedral geophysical configurations satisfying *only* the geophysical requirements for the Science Concept.

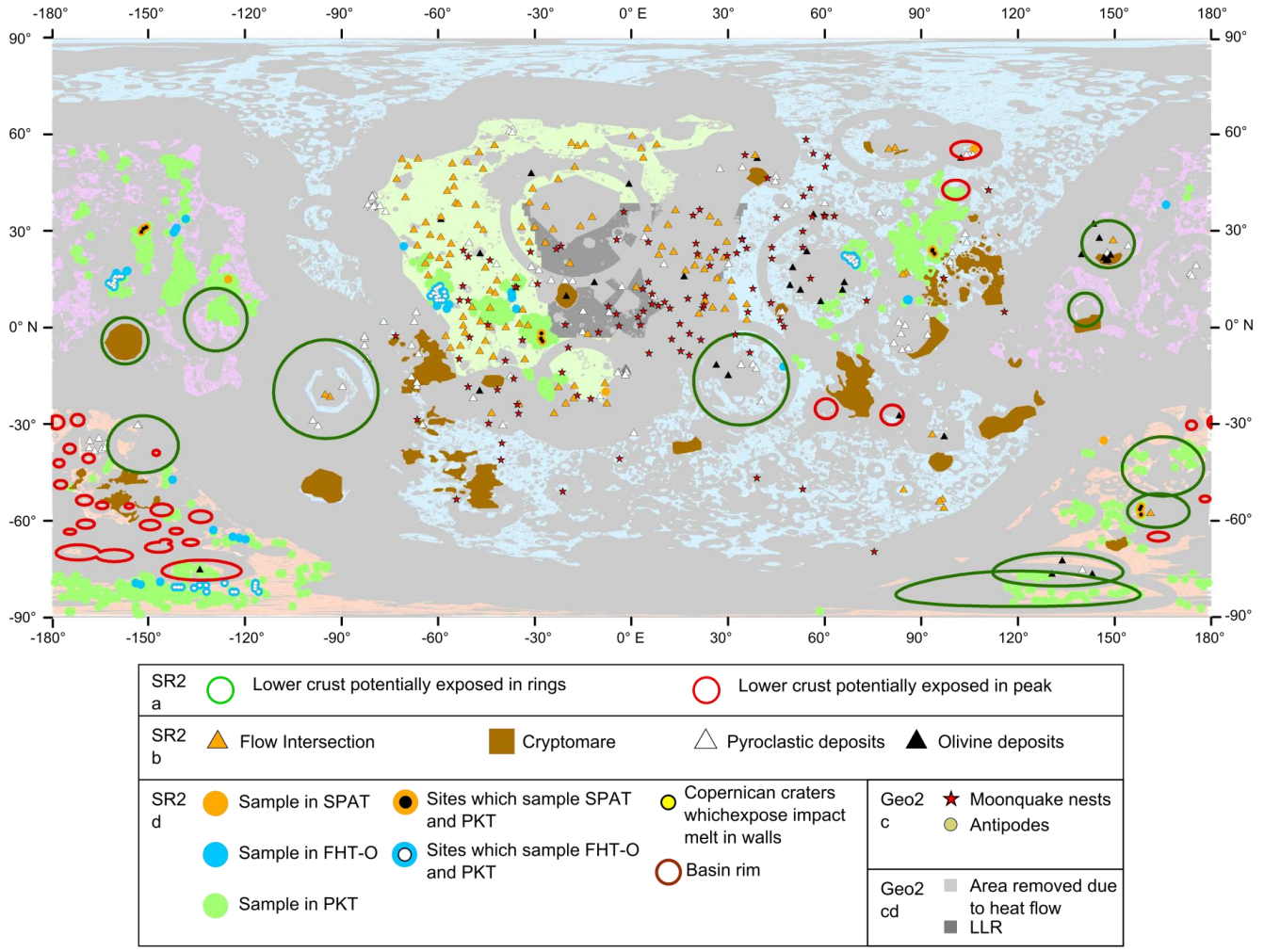

Figure 2.48 Final map displaying both geophysical and sample return aspects for all Science Goals in Science Concept 2. Here, the tetrahedral configurations satisfy Science Goal 2d only, showing that there are sites that partially overlap with Science Goals 2a and 2b.

GEOPHYSICAL CASE STUDY: A33 MOONQUAKE NEST

The A33 moonquake is used here as a case study example to address the geophysical aspects of Science Concept 2 (Fig. 2.49 to 2.52). This case study therefore uses the A33 moonquake nest to study the size and state of the core, as in Science Goal 2c, combined with a tetrahedral seismic configuration required for global mantle structure. One station needs to be placed within each of the areas within the white boundaries shown in Figs. 2.49 and 2.50, with the latter figure also excluding areas not appropriate for heat flow measurements. The configurations shown in Fig. 2.51 indicate the possible nearside locations of the geophysical package as part of a strict tetrahedral configuration, and Fig. 2.52 shows a global view of these locations (*i.e.*, including farside stations). This configuration allows for two LLR stations to be placed on the nearside, which will increase the extent of the current LLR network. As before, it would be preferable to place an additional geophysics lander with an LLR station in the southern hemisphere to improve the N-S extent of the current LLR network. It would also be ideal to place clusters of three geophysics packages at each apex of the tetrahedron configuration, to begin to address shallow moonquake distribution and upper mantle structure (but only within these clusters).

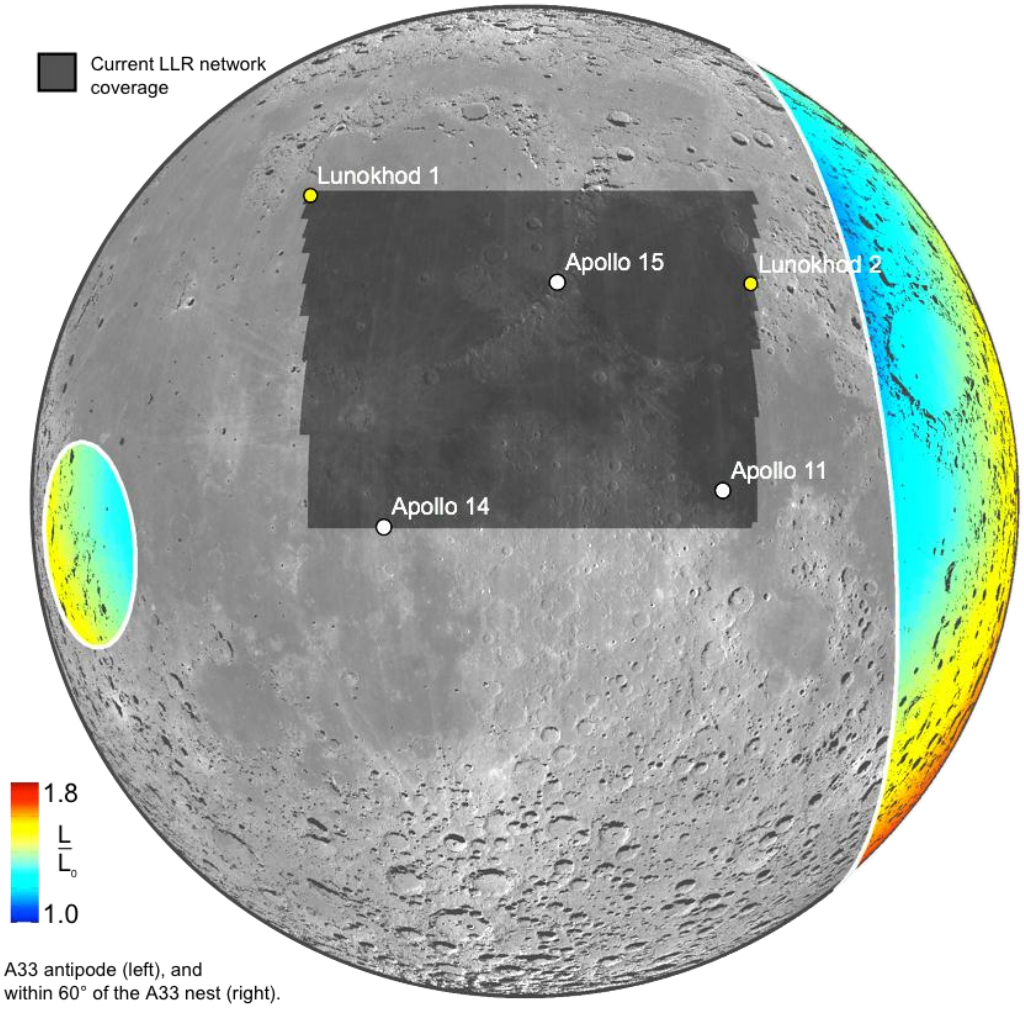

FIGURE 2.49 Map showing the same data as Fig. 2.30, but applied only to areas within S_1 of the A33 antipode (left), and within 60° of the A33 nest (right). This would be applicable if seismology and retroreflectors were to be combined in the same package and used A33 as the moonquake nest to study the lunar core.

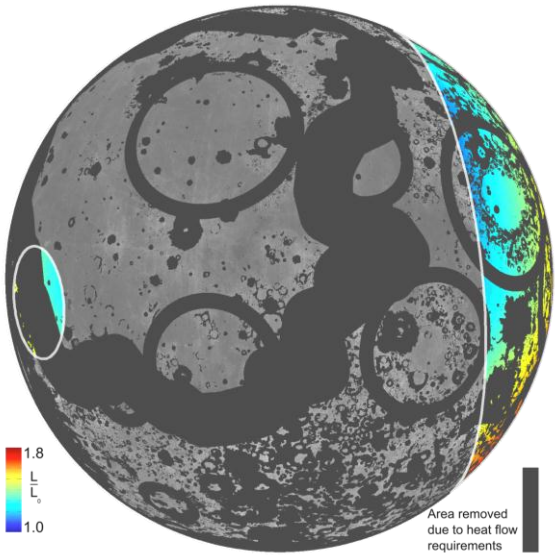

FIGURE 2.50 Map showing the same data as in Figure 2.49, with the subtraction of areas not suitable for heat flow experiments. This would be applicable if seismometers, retroflectors, and heat flow experiments were to be contained within one package and the A33 moonquake nest was to be used to study the lunar core.

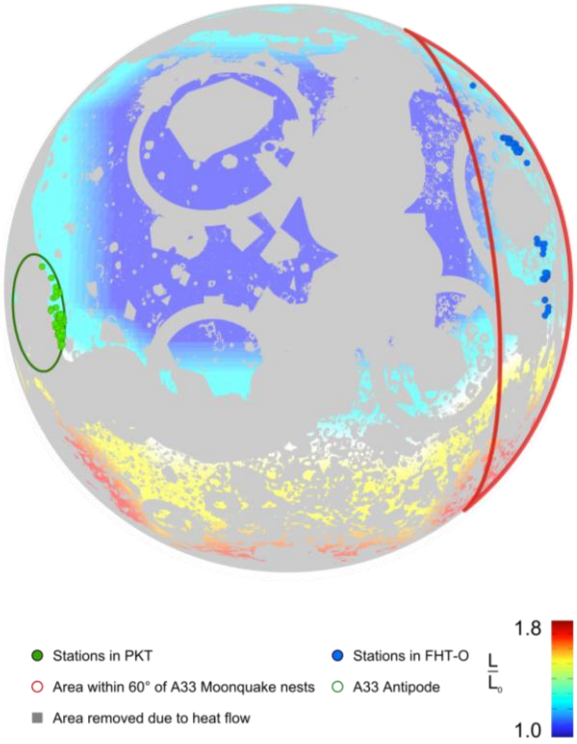

FIGURE 2.51 Map showing the same data as in Fig. 2.49, with the subtraction of areas of atypical crustal thickness. The background for this figure shows the results of the LLR optimization algorithm, discussed in Science Goal 2c.

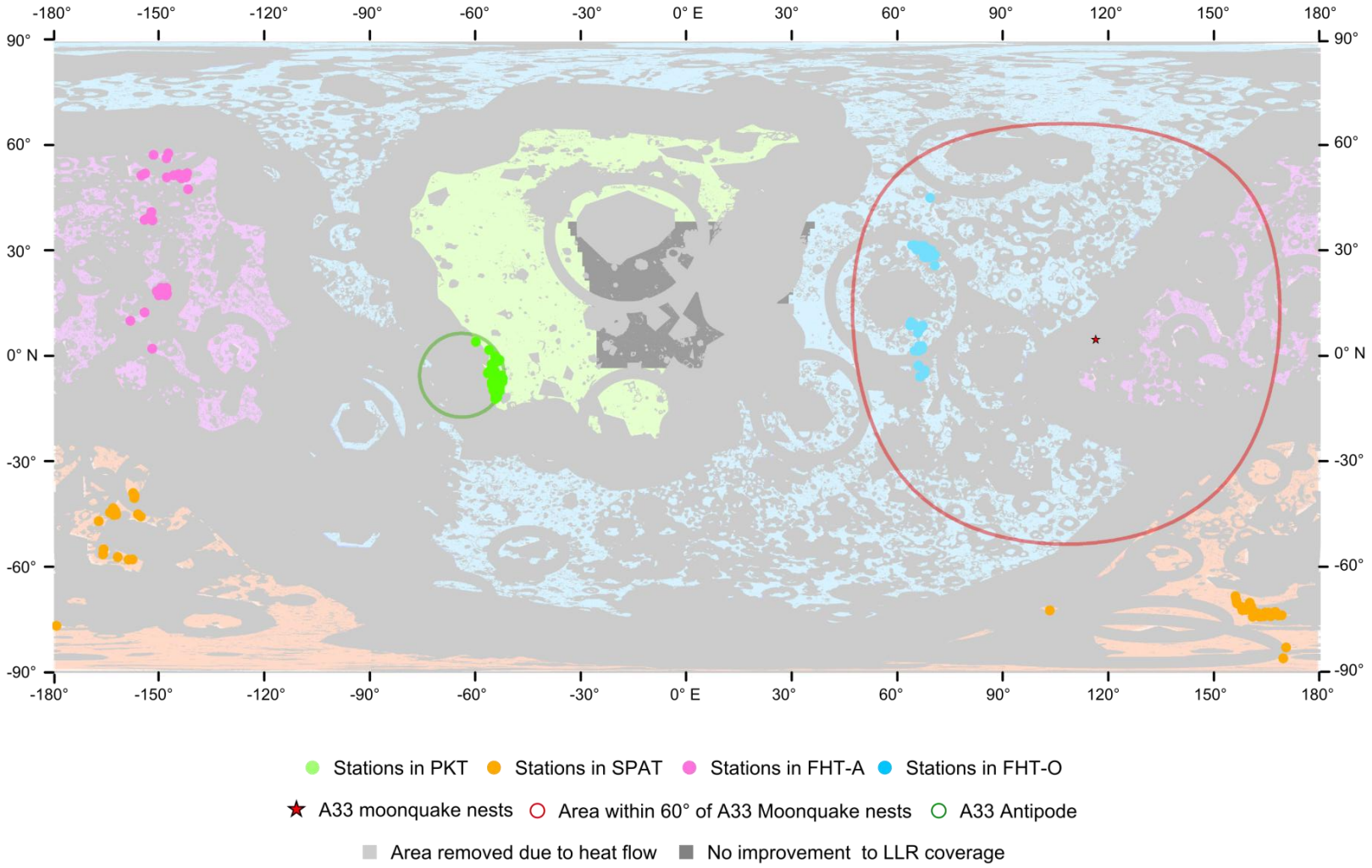

FIGURE 2.52 Map showing the potential global distribution of geophysical landers if the A33 deep moonquake nest is used as a seismic source to probe the Moon's core.

SAMPLE RETURN CASE STUDY 1: MOSCOVIENSE

Moscoviense is located on the lunar farside (FHT-A terrane) at ~26˚N, 148˚E and is Nectarian in age (Wilhelms *et al.*, 1987). This basin was chosen as a case study as it hosts a range of mantle derived materials (pyroclastic deposits, mare basalts, cryptomaria), and preserves a peak ring which may have originated from depths within the mantle and most probably samples both upper and lower crust.

Example landing sites have been selected within Moscoviense basin: from north to south, these are identified as sites 1, 2 and 3.

- *Site 1* is located in the topographic low of the basin, proximal to outcrops of the peak ring. Within the 10 km buffer, low-Ti basalt could be sampled, as well outcrop and rubble of the peak ring. From SELENE-SP detections the peak ring outcropping here may be of mantle material (Yamamoto *et al.*, 2010). At the 30 km buffer this site intersects olivine as detected by Pieters *et al.* (2011). The 20 and 30 km buffer also overlap with the unit Im (Kramer *et al.*, 2008) which may represent impact melt from basin formation (Thaisen *et al.*, 2011).

- *Site 2* is located on the basin floor at the junction between the southern pyroclastic deposit as mapped by Craddock *et al.* (1997) and the Im unit and the 10, 20 and 30 km buffer zones intersect with the unit Iltm (Kramer *et al.*, 2008). This site is proximal to the peak ring of the basin, and although not close to detections of olivine by Kayuga it is close to detections of low-Ca pyroxene and spinel (Pieters *et al.*, 2011).

- *Site 3* is located in a topographic low in the area between the peak ring and the inner ring (Figure 2.53). It is located within the cryptomare unit as identified by Hawke *et al.* (2005a), and is proximal to three detections of olivine (Yamamoto *et al.*, 2010). From this site it is expected that outcrop and rubble of both the peak ring and inner peak could be sampled.

SAMPLE RETURN CASE STUDY 2: NECTARIS

Nectaris is located on the lunar nearside, at the southeastern edge of the Procellarum KREEP Terrane (~16^{o}S, 35^{o}E) and is Nectarian in age. This basin contains at least two mare units, multiple pyroclastic deposits, two floor-fractured craters, and spectrally-detected olivine (Coombs *et al.*, 1990; Gaddis *et al.*, 2003; Hawke *et al.*, 1997; Kramer *et al.*, 2008; Schultz *et al.*, 1976; Yamamoto *et al.*, 2010), in addition to peak rings (Whitford-Stark, 1981) that may preserve uplifted mantle or lower-crustal material (this study).

Three potential landing sites within the Nectaris basin have been identified:

- *Site 1* is the westernmost potential landing site, just south of the innermost peak-ring. Samples of both a low-Ti mare basalt (Kramer *et al.*, 2008) and peak ring material (Whitford-Stark, 1981) could be sampled within the 10 km buffer. Pyroclastic glasses originating near the Daguerre crater (Coombs *et al.*, 1990; Hawke *et al.*, 1997) could potentially be sampled within this minimal buffer, but more likely within the 20 or 30 km buffers around the proposed landing site.

- *Site 2* is the easternmost potential landing site and is located in a geologically-similar area to Site 1. The same type of units could be sampled as in Site 1, though two different pyroclastic glass units (Gaudibert and Gaudibert B; Cooms *et al.*, 1990; Hawke *et al.*, 1997) may be encountered within the 30 km buffer as opposed to just one.

- *Site 3* is located nearer to the center of Nectaris basin and is the southernmost proposed landing site. Within a 10-km buffer, two mare units (one low-Ti and one intermediate-Ti), two pyroclastic units, and potentially two Copernican ejecta units can be sampled.

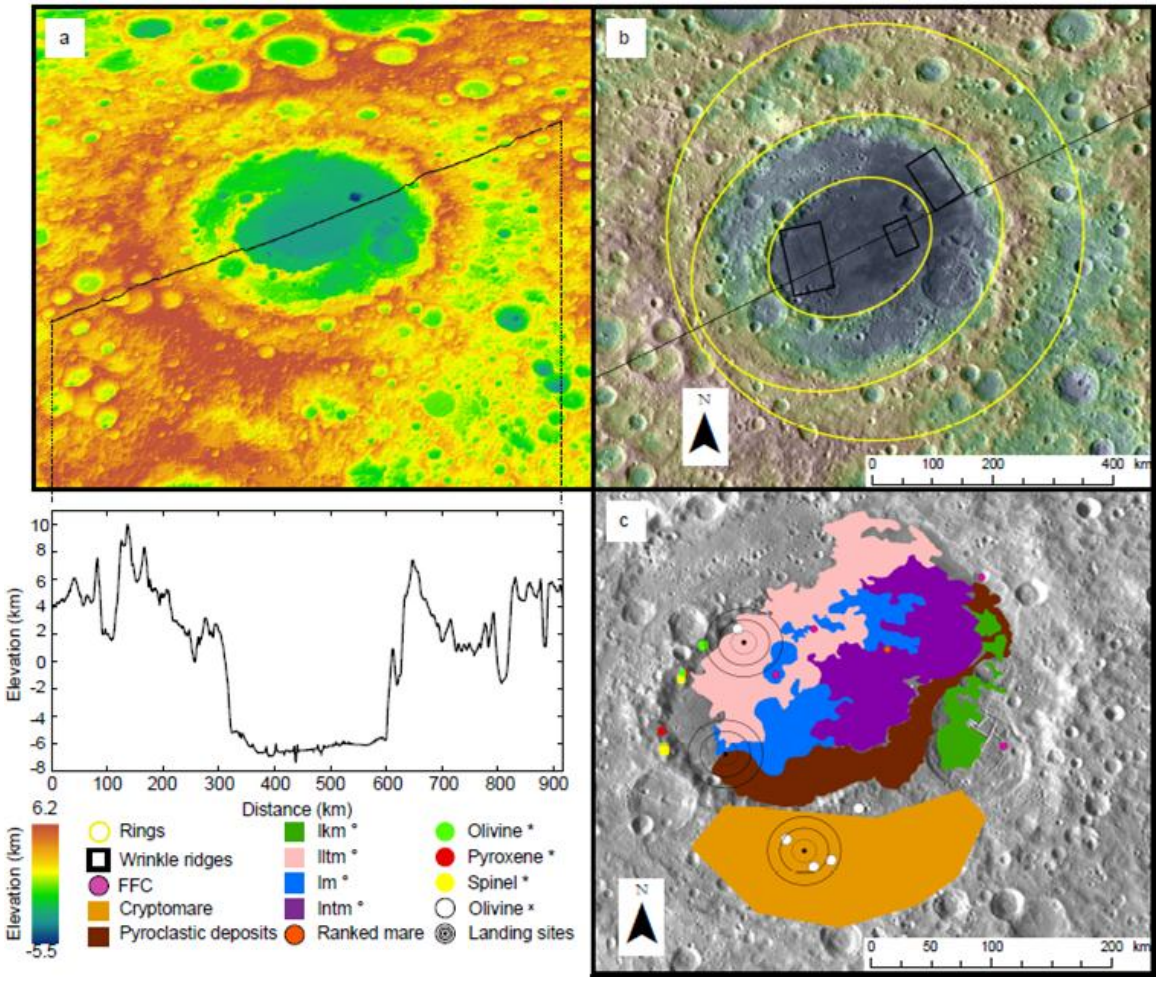

FIGURE 2.53 A) LOLA topographic DEM of Moscoviense and the corresponding topographic profile, highlighting the stark difference between the uplifted basin rings and topographic lows. B) Approximate location of the Moscoviense peak, inner and outer rings (as defined by Thaisen *et al.*, 2011). This image also identifies geomorphologic structures on the basin floor. C) Mapped geologic units within Moscoviense basin. The pyroclastic deposit was mapped by Craddock *et al.* (1997); the cryptomare by Hawke *et al.* (2005a). Spectrally determined mare units have been mapped by Kramer *et al.* (2008) (denoted ° in key) where **Ikm** is a low-Ti unit, **Iltm** is a low-Ti unit, **Im** is a very low-Ti unit, and **Intm** is a high-Ti unit. Spectral identifications have also been made by Pieters *et al.* (2011) (denoted * in the key) and Yamamoto *et al.* (2010) (denoted ^{x} in the key). Floor-fractured craters are taken from Concept 5. Three example landing sites are shown (1, 2, and 3 from N to S), with 10, 20 and 30 km buffer zones around each. Note that the ranked mare intersection is from this study (see Science Goal 2b) and that the point has a 30 km error associated with it.

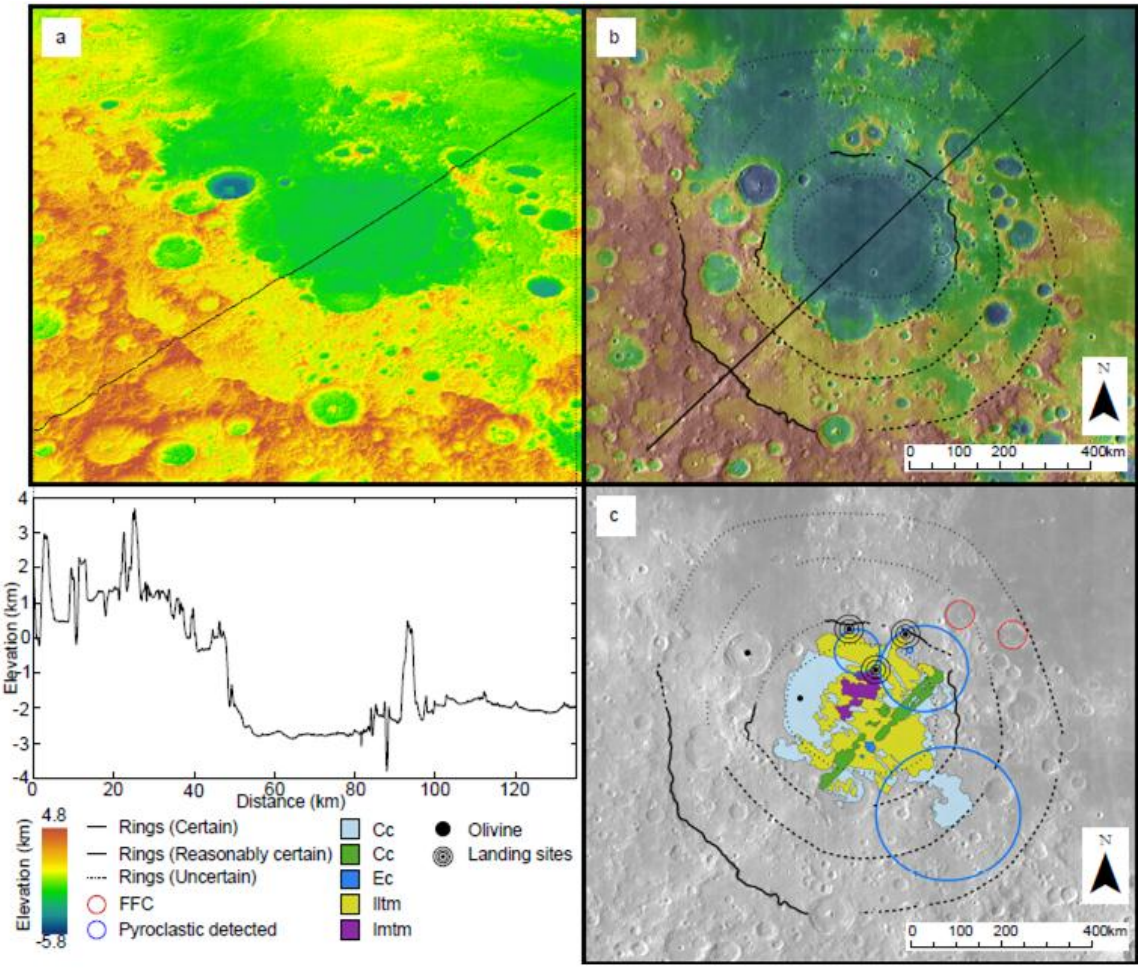

FIGURE 2.54 A) LOLA topographic DEM of Nectaris and the corresponding topographic profile, showing well-defined peak rings in the southwest compared to more muted topography in the northeast. B) Approximate location of the Nectaris basin rings showing locations where they are certain, reasonably-certain, and uncertain (Whitford-Stark, 1981). C) Mapped geologic units within Nectaris basin. The pyroclastic deposits were mapped by Coombs *et al.* (1990), Hawke *et al.* (1997), and Gaddis *et al.* (2003), and have been shown as blue circles correlating to their proposed areal extent (but note that this may not be their actual distribution). Spectrally-determined units have been mapped by Kramer *et al.* (2008) where **Imtm** is an Imbrian-aged, intermediate-Ti and Fe mare basalt, **Iltm** is an Imbrian-aged, low-Ti and low-Fe mare (possibly high-Al), and **Ec**, **Cc_1**, and **Cc_2** are Eratosthenian- and Copernican-aged crater ejecta, respectively. Spectral identifications of olivine have also been made by Yamamoto *et al.* (2010). Two floor-fractured craters (see Science Concept 5 and Schultz, 1976) are shown in the outer rings of Nectaris and are identified by red circles. Three example landing sites are shown with 10, 20, and 30 km buffer zones around each.